Pacific Northwest
NATIONAL LABORATORY

PNNL-35738

Evaluating Iodine Immobilization Technologies: Cermets, Polycermets, and Polyhalmets

April 2024

Brian J Riley
Nathan L Canfield
Saehwa Chong
Jared M Oshiro
Jaime L George
Carolyne A Burns
Jon L Helgeland

U.S. DEPARTMENT OF ENERGY

Prepared for the U.S. Department of Energy
under Contract DE-AC05-76RL01830

DISCLAIMER

PACIFIC NORTHWEST NATIONAL LABORATORY
operated by
BATTELLE
for the
UNITED STATES DEPARTMENT OF ENERGY
under Contract DE-AC05-76RL01830

Printed in the United States of America

Available to DOE and DOE contractors from
the Office of Scientific and Technical Information,
P.O. Box 62, Oak Ridge, TN 37831-0062
www.osti.gov
ph: (865) 576-8401
fox: (865) 576-5728
email: reports@osti.gov

Available to the public from the National Technical Information Service
5301 Shawnee Rd., Alexandria, VA 22312
ph: (800) 553-NTIS (6847)
or (703) 605-6000
email: info@ntis.gov
Online ordering: http://www.ntis.gov

PNNL-35738

Evaluating Iodine Immobilization Technologies: Cermets, Polycermets, and Polyhalmets

Radioiodine Management

April 2024

Brian J Riley
Nathan L Canfield
Saehwa Chong
Jared M Oshiro
Jaime L George
Carolyne A Burns
Jon L Helgeland

Prepared for
the U.S. Department of Energy
under Contract DE-AC05-76RL01830

Pacific Northwest National Laboratory
Richland, Washington 99354

Summary

The work in this report documents the efforts conducted to assess the feasibility of some of the ideas documented in Pacific Northwest National Laboratory invention disclosure reports (IDRs) including:

1) *Iodine capture in polyacrylonitrile (PAN)-containing composite sorbents* (**32451-E**). In this work, the composites evaluated included Ag^0, Bi^0, Cu^0, Bi_2S_3, and Cu_2S embedded in PAN.

2) *Metal iodide removal from these sorbents through dissolution in dimethyl sulfoxide (DMSO)* (**32729-E**). In this work, PAN dissolution was evaluated for multiple types of sorbents including Ag-Pan, Bi-PAN, Cu-PAN, Bi_2S_3-PAN, and Cu_2S-PAN.

3) *Using metal-sulfide sorbents for iodine capture* (**32647-E**). In this work, the composites evaluated under this IDR included Ag_2S, Bi_2S_3, and Cu_2S embedded in PAN.

4) *Using low-melting metals to immobilize (encapsulate) iodine-loaded and polymer-containing sorbents into polymer-ceramic-metal (called polycermet) or polymer-halide-metal (called polyhalmet) composite waste forms* (**32625-E**). In this work, the iodine-loaded PAN composites included AgI-PAN, BiI-PAN, and CuI-PAN.

5) *Ceramic-metal composite waste form synthesis of polymer-containing materials using low-melting metals like bismuth, tin, or bismuth-tin alloys* (**32537-E**). In this work, the metals evaluated included Bi, 58Bi-42Sn eutectic.

6) *Cermets for immobilizing commercial sorbents loaded with radioiodine* (**32806-E**). In this work, AgIX (iodine-loaded silver faujasite zeolite) was evaluated in cermet form.

All the ideas and work encompassed in this document cover methods for radioiodine capture and immobilization for environmental remediation from off-gas releases from nuclear processes. Details are provided for a variety of polymer-containing composite sorbent production processes, experiments conducted to better understand processing parameters of the polymer composite production process (e.g., viscosity of PAN dissolved in DMSO), methods used for producing polycermet/polyhalmet composite waste forms, and methods for removing the polymer phase from the iodine-loaded polymer-containing composite beads.

While the initial approach of using Al_2O_3 as a surrogate (i.e., pellets **2b** and **2c**) did not allow for pelletization of dense monoliths, this process worked well for pure metal iodides (MI_x) where low-porosity pellets were achieved using single-press pellets (i.e., pellets **3b**, **3c**, **4a**, **5a**, and **5b**). For pelletization of three-phase pellets containing a metal-iodide along with either a polymer phase (i.e., pellets **6b**, **6c**, and **7d**) or aluminosilicate (decomposed zeolite) phase (i.e., pellet **7e**). All other pellets produced (i.e., pellets **1**, **2a**, **3a**, **6a**, **7a**, **7b**, and **7c**) were made of pure metal at different thicknesses and run with the samples sort of as standards so that all samples were subject to the same conditions. For the Set-6 and Set-7 pellets multi-layer approach was used with different pressings prior to pellet removal from the die. The aim of this was to create barrier layers below and above the middle iodine-containing layer. Also, additional fill metal was added to the middle layer to fill in void spaces around the MI_x-containing phase in between the pure metal layers. A summary of these pellets is provided in Table S-1.

Table S-1. Summary of pellets produced within this project lifecycle including the sample set, the number of samples produced in each set (#), the metal encapsulant used, other phases present within the set of samples produced for that set, the target metal-iodide complex (MI_x), and the atmosphere used in the heat treatment process (atm).

Set	No. of Pellets	Metal	Other(s)	Target MI_x	Atm
1	1	Bi	–	–	Air
2	3	Bi	Al_2O_3	–	Air
3	3	Bi	AgI	AgI	Vac
4	1	Bi	CuI	CuI	Vac
5	2	Bi-Sn	AgI, CuI	AgI, CuI	Air
6	3	Bi	AgIPAN	AgI	Vac
7	5	Bi	CuIPAN, AgIX	AgI, CuI	Vac

Acknowledgments

Pacific Northwest National Laboratory (PNNL) is operated by Battelle Memorial Institute for the DOE under contract DE-AC05-76RL01830. Authors thank Cindy Powell, Alexander Kendall, Allan Tuan, Rachel Thompson (PNNL) for their internal support of this project as well as John Vienna, Mary Bliss, and Stuart Arm (PNNL) for their helpful reviews of the project proposal. Authors also thank Derek Dixon (PNNL) for his help setting up the Keyence optical microscope and Christian Herbert from Dralon for providing the samples of PAN fibers, Troy Garn from Idaho National Laboratory (INL) for helpful discussions regarding the PAN composite synthesis process, and Bill Del Cul (Department of Energy Office of Nuclear Energy, formerly of Oak Ridge National Laboratory) for helpful discussions about ceramic-metal composite synthesis processes.

Acronyms and Abbreviations

^{129}I	iodine-129
^{131}I	iodine-131
(a)	aqueous species
(g)	gaseous species
(ia)	neutral aqueous species
(s)	solid species
AgX	silver faujasite
AgIX	iodine-loaded AgX
atm	atmosphere used during pellet heat treatment
AVE	average
BSE	backscattered electron (detector)
BiS	Bi_2S_3
CE	conversion efficiency
cermet	ceramic-metal (composite)
CPS	cold-press-and-sinter
CUP	cold uniaxial pressing
CuS	Cu_2S
DIW	deionized water
DMSO	dimethyl sulfoxide [$(CH_3)_2SO$]
DSC	differential scanning calorimetry
EDS	energy dispersive X-ray spectroscopy
halmet	halide-metal (composite)
HIP	hot isostatic pressing
HKUST	Hong Kong University of Science and Technology
HUP	hot uniaxial pressing
ID	identification
IDR	invention disclosure report
mass%	mass percent
MOF	metal organic framework
MS_x	metal sulfide (compound)
OM	optical microscopy
PAN	polyacrylonitrile
PDF	powder [X-ray] diffraction file
PNNL	Pacific Northwest National Laboratory
polycermet	polymer-ceramic-metal (composite)
polyhalmet	polymer-halide-metal (composite)
polymet	polymer-metal (composite)

PSD	particle size distribution
PSI	pounds per square inch
RPM	revolutions per minute (mixing rate)
SD	standard deviation (± 1σ)
SEM	scanning electron microscopy
SEI	secondary electron (detector)
SG	[crystallographic] space group
SPS	spark plasma sintering
STA	simultaneous thermal analyzer
TGA	thermogravimetric analysis
(v)	atmosphere was vacuum (during pellet firing)
vol%	volume percent

Description of Symbols and Variables

A_d	area of die face (for making pellets)
alternative ID	includes the general composition (if easily written) for each pellet
atmosphere type	atmosphere used for sintering pellet(a)
C%m (MI_x, mass%)	conversion (mass%) of metal iodide (MI_x) in composite
date (mm/dd/yy)	date when sample heat treatment was initiated
F_A	force applied (during pellet pressing)
g	force of gravity (9.8 m/s^2)
h	height of pellet (i.e., thickness)
iodine loading	where data is provided for iodine loading of the base sorbent
K_{sp}	solubility product constant
Δm (mass%)	change in mass from before to after firing process
$m\%_{gL}$ (mass%)	mass% of getter loading in PAN composite beads
$m_{p\text{-}a}$ (g)	mass of phase “a” in pellet
$m_{p\text{-}b}$ (g)	mass of phase “b” in pellet
mf_I (mass fraction)	mass fraction of iodine in MI_x compound
mf_{ML} (mass fraction)	mass fraction of metal loading in composite
m_g (g)	mass of getter added to PAN-DMSO mixture during bead production
$m_{m,r}$ (g)	mass of residual (unreacted) getter after iodine loading
m_I (g)	mass of iodine loaded during iodine loading experiments
M_I (moles)	moles of iodine in the MI_x compound
$m_{m,e}$ (g)	mass of metal encapsulant
$m_{m,r}$ (g)	mass of residual (unreacted) metal after iodine loading
m_{MI_x} (g)	mass of MI_x in iodine-loaded composite
$m_{p,f}$ (g)	mass of fired pellet (after sintering)
$m_{p,g}$ (g)	mass of green (unfired) pellet measured before sintering)
m_{PAN} (g)	mass of PAN in composite synthesis batch
m_{recov} (g)	mass of recovered sample
m_s (g)	mass of sample
$m_{s,f}$ (g)	mass of final sample (after iodine loading experiments)
$m_{s,i}$ (g)	mass of initial sample (during iodine loading experiments)
n_D	index of refraction (at sodium D line at 589 nm)
P_A (MPa)	pressure applied (making pellets)
phase-a (comp.)	description of phase-a in the pellet
phase-b (comp.)	description of phase-b in the pellet
phase-c (comp.)	description of phase-c in the pellet
phase-d (comp.)	description of phase-d in the pellet
phase-a (g)	mass of phase-a weighed out for making the pellet

phase-b (g)	mass of phase-b weighed out for making the pellet
phase-c (g)	mass of phase-c weighed out for making the pellet
phase-d (g)	mass of phase-d weighed out for making the pellet
q_e (mg/g)	milligrams of iodine loaded per gram of sample
Q_e (g/g)	grams of iodine loaded per gram of sample
r (mm or cm)	radius (of pellet die)
R%	recovered mass%
ramp (°C/min)	ramp rate used for heat treatment (sintering)
ρ_b (g/cm^3)	bulk density
$\rho_{b,em}$ (g/cm^3)	bulk density of encapsulant matrix (e.g., metal enveloping phase)
$\rho_{b,MIx}$ (g/cm^3)	bulk density of the MI_x complex
$\rho_{p\text{-}a}$ (g/cm^3)	density of phase-a
$\rho_{p\text{-}b}$ (g/cm^3)	density of phase-b
ρ_{PAN} (g/cm^3)	density of PAN
sample Number	identification of the sample based on Set-# and letter identification
T_b (°C)	boiling temperature
T_d (°C)	decomposition temperature
T_g (°C)	glass transition temperature
t_{ht} (h)	heat treatment (sintering) time
T_{ht} (°C)	heat treatment (sintering) temperature
T_{Load} (°C)	temperature used during iodine loading of sorbents
T_m (°C)	melting temperature
$T_{m,m}$ (°C)	melting temperature for metal
T_{mix} (°C)	temperature of PAN mixture during composite bead production
$T_{o,c}$ (°C)	continuous operating temperature (polymers)
$T_{o,p}$ (°C)	peak operating temperature (polymers)
$t_{p,f}$ (mm)	thickness of fired pellet (after sintering)
$t_{p,g}$ (mm)	thickness of green pellet (before sintering)
$T_{s,L}$ (°C)	lower sintering temperature
$T_{s,U}$ (°C)	upper sintering temperature
T_V (°C)	viscosity temperatures
$V_{\%T}$ (vol%)	volume of final form based on predicted total volume
V_{DMSO} (mL)	volume of DMSO
$V_{m,e}$ (cm^3)	volume of encapsulant metal phase
V_{MIx}/m_{LS} (cm^3/g)	volume of MI_x complex per mass of iodine-loaded PAN composite
$V_{p,g}$ (cm^3)	volume of green (unfired) pellet
$V_{polymet+I}$ (cm^3)	volume of iodine-loaded PAN composite (polymet)
V_{tot}/m_{LS} (cm^3/g)	total volume iodine-loaded PAN composite per mass of loaded sorbent
$WL_{I,m}$ (mass%)	waste loading of iodine in final form in terms of mass%

$WL_{\mathrm{MI,v}}$ (vol%)	waste loading (vol%) based only on incorporation of MI_x complex
x_{i}	molecular weight of iodine
x_{m}	molecular weight of metal getter in compound
x_{MI_x}	molecular weight of MI_x compound

Contents

Figures

Tables

1.0 Introduction

Radioiodine can be released from nuclear processes such as used nuclear fuel reprocessing, salt-fueled molten salt reactor operations and waste treatment, as well as nuclear accidents. Depending on the age of the fuel and radioiodine isotopes, the isotopes present after these processes could be different but the primary radioiodine isotopes will likely be iodine-129 (^{129}I) and iodine-131 (^{131}I). The half-lives ($t_{1/2}$) of these iodine radioisotopes are drastically different with one being very short lived ($t_{1/2}$ for ^{131}I is 8.02 days) and one being very long-lived ($t_{1/2}$ for ^{129}I is 1.57×10^{7} years). The capture and effective storage of these iodine radioisotopes is important to prevent transport through the environment. The goal of this work was to evaluate the concept of using ceramic-metal (*cermet*) and polymer-ceramic-metal (*polycermet*) composites for the capture and storage processes of managing radioiodine from nuclear processes. Other terms for cermet and polycermets include halide-metal (*halmet*) and polymer-halide-metal (*polyhalmet*) composites, respectively, when the "cer" phase is a halide salt. The interplays of the different phases (polymer, metal, ceramic/halide) are shown in Figure 1-1.

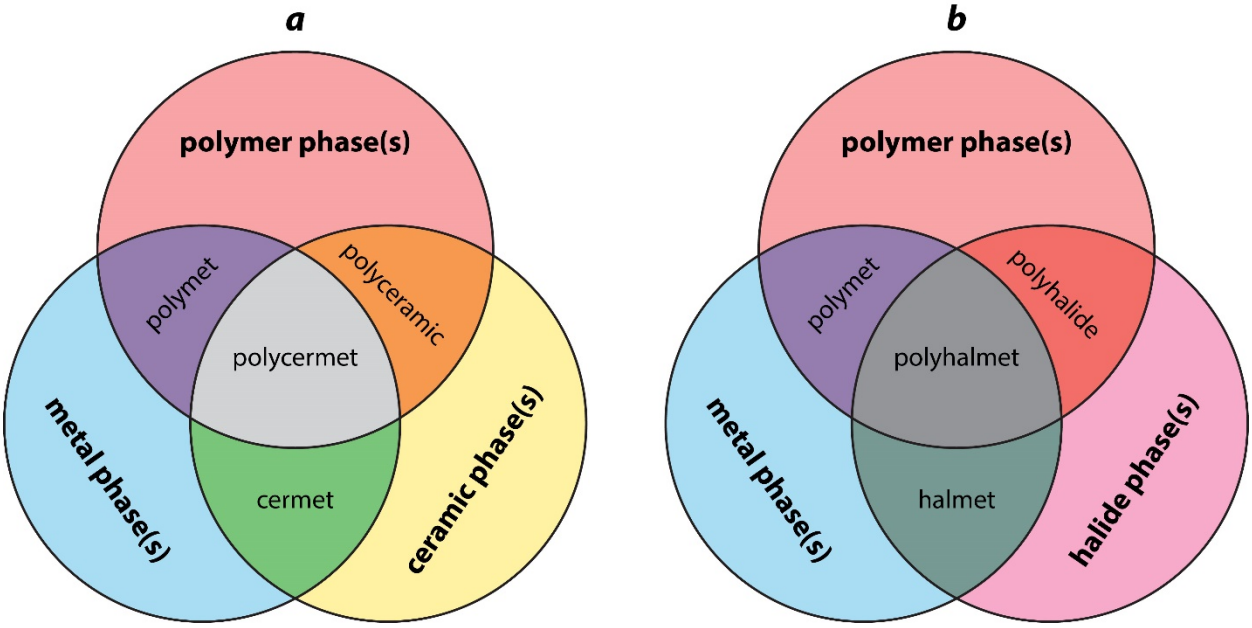

Figure 1-1. Venn diagrams showing phase relationships and composite names for (a) the polymer-metal-ceramic material system and (b) the polymer-metal-halide material system.

The project covered within this report is based off using demonstrated technologies for iodine capture that involve a polyacrylonitrile (PAN) phase as a scaffold to host materials that have demonstrated affinity for a target analyte (i.e., Ag^0, Bi^0, Cu^0, Sn^0, Ag_2S, Bi_2S_3, Cu_2S, Ag-loaded xerogels, and sulfide-based aerogels) during a gaseous loading process (Riley et al. 2014; Riley and Garn 2019; Cordova et al. 2020; Riley et al. 2020a; Yu et al. 2020; Riley et al. 2021a; Chong et al. 2022; Riley et al. 2024). The porous polymer matrix acts as a net (Figure 1-2a) that holds the target getter during the loading process, much like a fly is held within a spider web. Examples of some of the different PAN composite beads from these previous projects include metal-PAN (75 mass% metal in PAN) composites (Figure 1-2b) and composites of PAN with metal organic frameworks (MOFs) loaded at different mass ratios of 0 mass% MOF (pure PAN beads) to 90 mass% MOF (Figure 1-2c). The composite manufacturing process is very flexible and adaptable for new active materials to be loaded into PAN at different mass loadings.

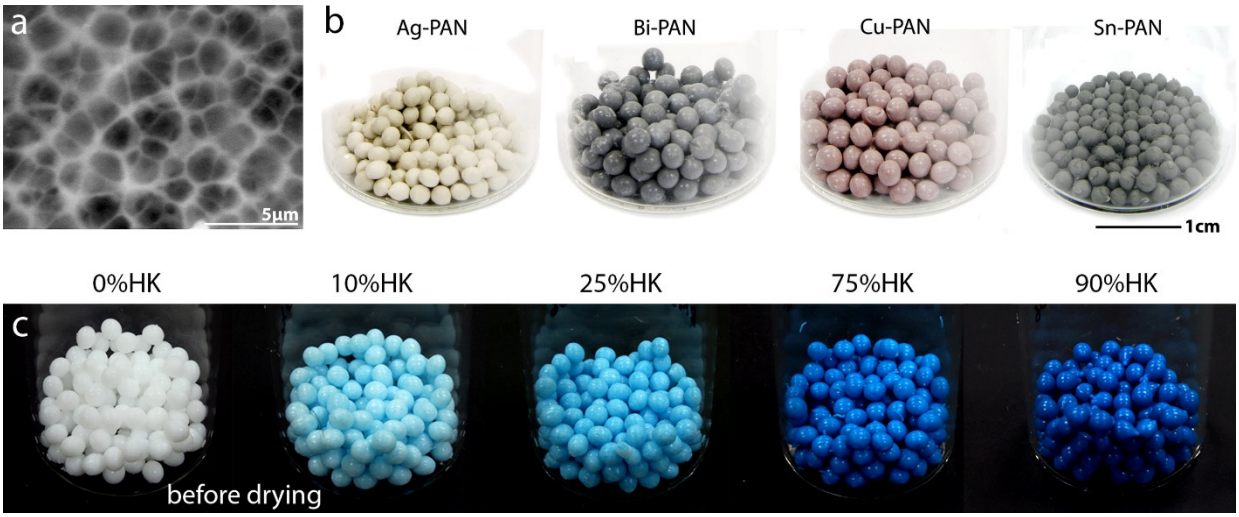

Figure 1-2. Optical collage showing a summary of the PAN composites including (a) a high-magnification scanning electron micrograph of the PAN matrix in a bead drawing attention to the webbed network, (b) images of metal-PAN composites (metal = Ag, Bi, Cu, and Sn, from left to right), and (c) images of pure PAN beads and MOF-PAN composites from 10 mass% (10%HK) to 90 mass% (90%HK) of the HKUST-1[1] MOF in PAN (from left to right) (Riley et al. 2020a; Chong et al. 2022).

A summary of the overall planned approach of the project documented in this report is provided in Figure 1-3. In this project, the general approach outlined in Figure 1-3a was to first determine the properties of the starting metal encapsulant materials including the melting temperatures of the metals ($T_{m,m}$) and the bulk densities (ρ_b). Then, simple cermets were made to evaluate the process of pressing a surrogate filler material in with the metal particles (*approach-1*) so that the heterogeneous pelletization process could be better understood prior to working with iodine-containing material as the filler. For *approach-2*, pure metal-iodides (i.e., AgI and CuI) were used as the filler material. For *approach-3*, the iodine-loaded polyhalide materials (iodine-loaded PAN composites) were used as the filler. Figure 1-3b describes some of the other tasks that were included in this project such as fundamental studies on the thermoviscosity of the PAN-DMSO mixture, analysis of the pipette-tip orifice diameters used during synthesis of PAN composites, and an outline of how to evaluate PAN removal from iodine-loaded PAN composites.

In this work, several different PAN composites were produced so that they could be loaded with iodine and the waste form production processes could be evaluated with different iodine-containing phases. The different iodine sorbents produced in this study included: 75Ag-PAN (75 mass% Ag^0), 75Cu-PAN (75 mass% Cu^0), 75Bi-PAN (75 mass% Bi^0), 80Cu-PAN (80 mass% Cu^0), 90Cu-PAN (90 mass% Cu^0), 80AgS-PAN (80 mass% Ag_2S), 90AgS-PAN (90 mass% Ag_2S), 80BiS-PAN (80 mass% Bi_2S_3), and 80CuS-PAN (80 mass% Cu_2S). Regarding the waste form fabrication process, Bi^0 and Bi-Sn eutectic were the primary materials evaluated as the encapsulant matrix.

The methodologies for selecting these particular materials is based off of success using these specific metals as effective active getters for iodine based on data in the literature as well as work done at Pacific Northwest National Laboratory (PNNL) on Ag (Riley et al. 2017; Riley et al. 2021b; Chong et al. 2022; Riley et al. 2022a; Riley et al. 2022b), Bi (Yu et al. 2020; Baskaran et al. 2022;

[1] HKUST denotes Hong Kong University of Science and Technology.

Baskaran et al. 2023), Cu (Riley et al. 2021b; Chong et al. 2022), Sn (Riley et al. 2013a; Riley et al. 2013b; Riley et al. 2014; Riley et al. 2021b; Chong et al. 2022), and sulfur-containing compounds (Riley et al. 2011; Riley et al. 2013a; Riley et al. 2013b; Riley et al. 2014; Subrahmanyam et al. 2015; Yu et al. 2020).

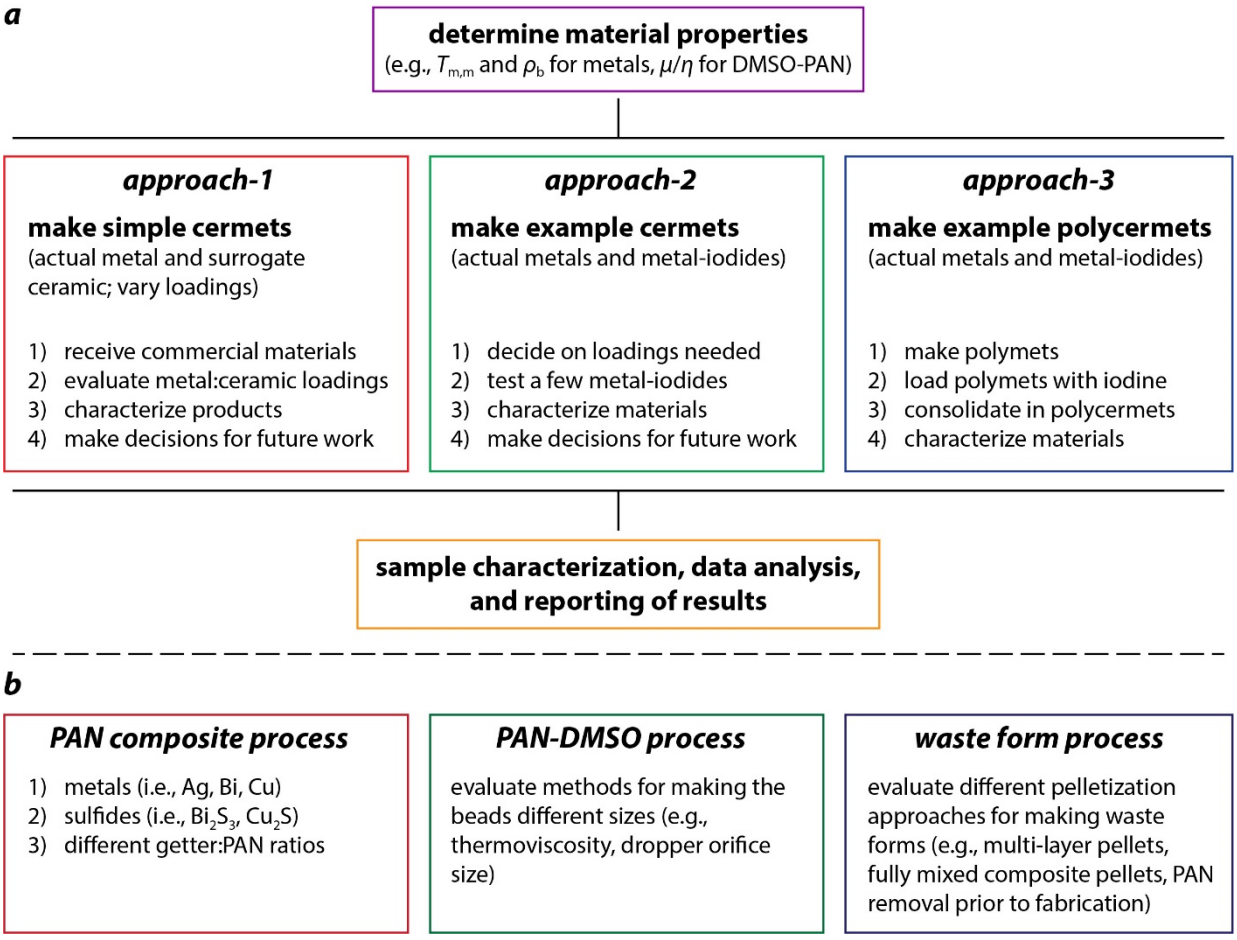

Figure 1-3. Summary graphic describing the high-level tasks encompassed in this project including (a) the general flow of the project in terms of phases and (b) some specific parts of the project including example materials, processes, and variables being evaluated. Variables and undefined terms are defined later in the report.

2.0 Project Background and Approach

2.1 Selection of Encapsulant Metals

The initial plan was to use 100Bi, 100Sn, 58Bi-42Sn (eutectic), and 55.5Bi-44.5Pb (eutectic) metals as the metallic (met) portion of the polycermet/polyhalmet composite waste form. the following metals for this project based on the low $T_{m,m}$ values for the metals (see Table 2-1), commercial availabilities, procurable sizes, malleabilities, and known formation of the targeted metal-iodide complexes (MI_x) for these metals in the event that iodine was released during the waste form production step where Bi forms BiI_3/BiOI, Sn forms SnI_4, and Pb forms PbI_2. In addition to the T_m values, Table 2-1 also shows the low sintering temperature ($T_{s,L}$) and high sintering temperatures ($T_{s,H}$) based on the recommendation found in the literature as the optimum being between 2/3*T_m and 3/4*T_m (in °C) (Liu and Chen 2014). The binary eutectic compounds of 55.5Bi-44.5Pb and 58Bi-42Sn are shown in the phase diagrams in Figure 2-1a and Figure 2-1b, respectively. Issues arose with the 55.5Bi-44.5Pb material procured for this work and thus it was removed from the study as a candidate encapsulant metal.

Table 2-1. Melting temperatures for the metals ($T_{m,m}$), boiling temperatures (T_b), lower sintering temperature ($T_{s,L}$ = 2/3*T_m in °C), upper sintering temperature ($T_{s,U}$ = 3/4*T_m in °C), and bulk density (ρ_b) for metals (Sobolev 2007; Lide 2008; Khairulin et al. 2010; Liu and Chen 2014).

Metal (mass%)	$T_{m,m}$ (°C)	T_b (°C)	$T_{s,L}$ (°C)	$T_{s,U}$ (°C)	ρ_b (g/cm^3)
100Bi	271	1564	180.7	203.3	9.7828
100Sn	231.93	2602	154.7	174.0	7.2900
58Bi-42Sn[(a)]	138	–	92.0	103.5	8.5588
55.5Bi-44.5Pb[(a)]	124	1670	82.7	93.0	10.73

[(a)]Eutectic compound

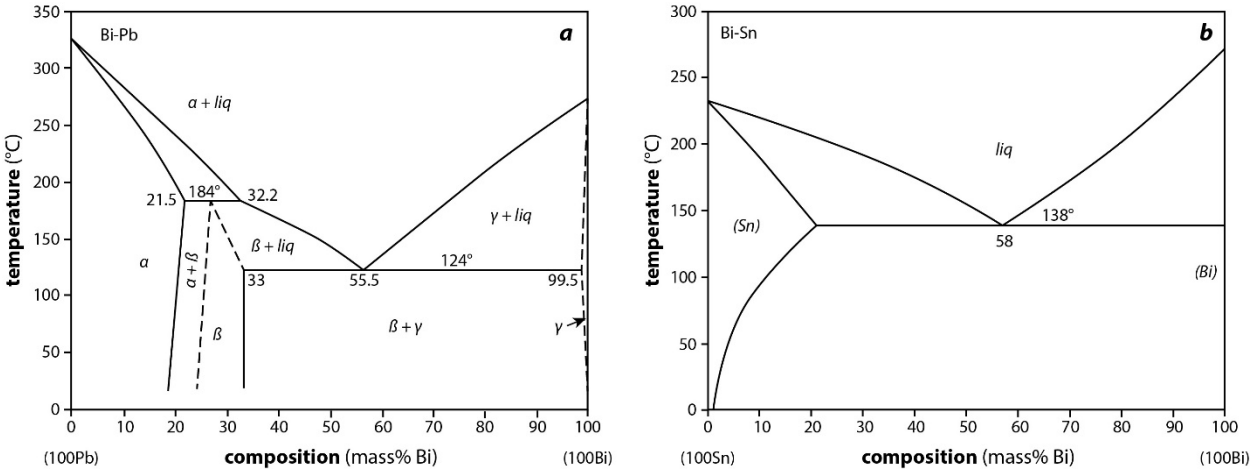

Figure 2-1. Phase diagrams from the literature of (a) the Bi-Pb binary (Sobolev and Gessi 2015) and (b) the Bi-Sn binary (NIST 2023). These figures were redrawn from the originals. The target eutectic compounds for this study are the 55.5Bi-44.5Pb (mass%) eutectic in (a) and the 58Bi-42Sn (mass%) eutectic in (b).

2.2 Target Metal Iodide Complexes (MI_x)

Regarding the final fate of radioiodine storage and immobilization, the following MI_x compounds were identified as candidates: AgI, BiI_3, BiOI, CuI, and PbI_2 (see Table 2-2). These range in

physical properties (i.e., T_m, T_b, ρ_b, K_{sp}) as well as the mass of iodine in the overall compound, defined here as the iodine waste loading (WL_I).

Table 2-2. Summary of metal-iodide compounds (MI_x) including the melting temperatures (T_m), boiling temperatures (T_b), bulk densities (ρ_b), solubility product constants (K_{sp}), and iodine waste loading (WL_I) for each where data were available (Lide 2008). A K_{sp} value for BiOI was not found in the literature at the time of completing this report.

MI_x	T_m (°C)	T_b (°C)	ρ_b (g/cm^3)	K_{sp}	WL_I (mass%)
AgI	558	1506	5.68	8.52×10^{-17}	54.1
BiI_3	408.6	542	5.778	7.71×10^{-19}	64.6
BiOI	308[(a)]	–	7.92	–	36.1
CuI	591	≈1290	5.67	1.27×10^{-12}	66.6
PbI_2	410	872[(a)]	6.16	9.5×10^{-9}	55.1

(a) decomposes

2.3 Target Polymer Matrix

The only polymer being used in the current study is PAN, which is used because of the ideal structural properties including open porosity, ease of composite bead formation, and demonstrated properties during iodine capture. Some literature data on the thermal properties of PAN are provided in Table 2-3 (Vatanpour et al. 2023). Also, it fairs well at high active sorbent loading. The mass loss curve based on thermogravimetric analysis (TGA) data was reported in the literature by Horrocks, Hall, and Zhang (Hall et al. 1994; Horrocks et al. 1994) and is shown Figure 2-2. This shows that the mass loss should not be an issue within the temperature regime used for this study where sintering temperatures are below 300°C.

Table 2-3. Relevant properties for polyacrylonitrile (PAN) from the literature including the glass transition temperature (T_g), T_m, decomposition temperature (T_d), continuous operation temperature ($T_{o,c}$), and peak operating temperature ($T_{o,p}$) (Vatanpour et al. 2023).

Property	Details
Amorphous density	1.184 g/cm^3
Tensile strength	24–65 cN/tex
T_g	100°C
T_m	317°C
T_d	175°C
$T_{o,c}$ (max)	130°C
$T_{o,p}$ (max)	135–145°C

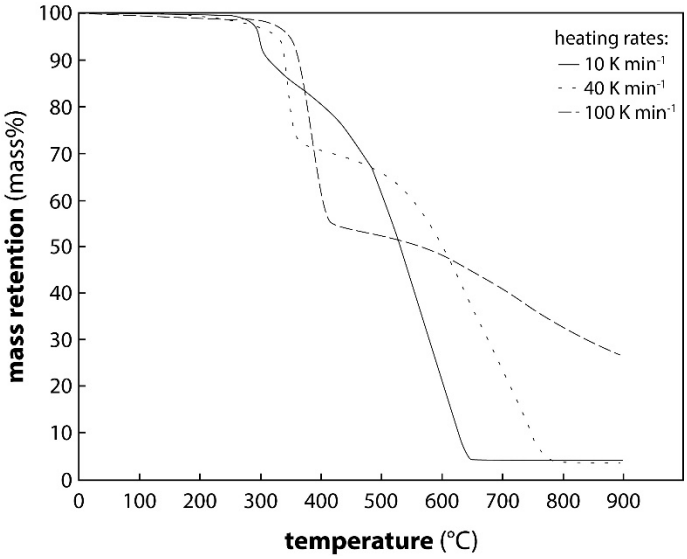

Figure 2-2. TGA data for PAN homopolymer at different heating rates in air (this figure was redrawn from the original) (Hall et al. 1994; Horrocks et al. 1994).

The thermal decomposition and flammability processes for acrylic fibers were documented (Hall et al. 1994; Horrocks et al. 1994) and shown in Figure 2-3. These types of data are often collected and available in the literature on the topic of preventing flammability of polymers. At high heating rates, the pathway to the right (i.e., $r_2 \rightarrow r_4 \rightarrow r_6$) dominates (i.e., cyclisation – dehydrogenation to dehydrogenation into a graphite-type structure, respectively). The pathway to the left (i.e., $r_1 \rightarrow r_3 \rightarrow r_5$) demonstrates "chain scission" (or polymer length shortening due to degradation) processes that can lead to the formation of flammable and volatile compounds.

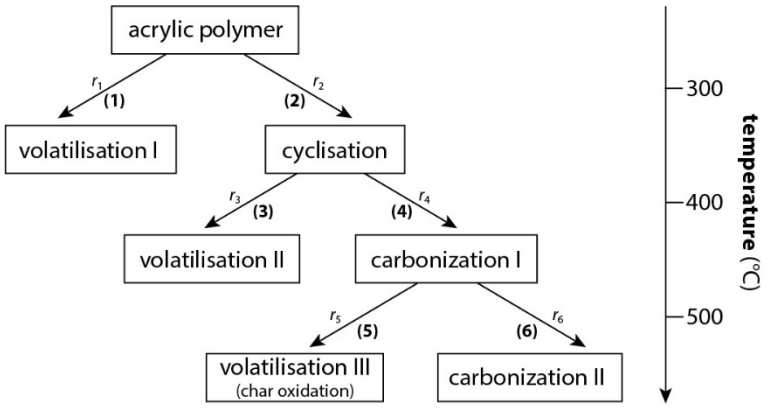

Figure 2-3. Model of polymer temperature-dependent conversion proposed for the acrylic polymer pyrolysis process (this figure was redrawn from the original) (Hall et al. 1994; Horrocks et al. 1994). In this figure, $r_{\#}$ denotes the route number.

In a previous study (Chong et al. 2022) with the Ag-PAN, Bi-PAN, Cu-PAN, and Sn-PAN composite beads, iodine loading was compared across the set of beads as well as iodine loading without the PAN (i.e., just the pure metal particles) where loading was conducted at 120°C ± 1°C for 48 h. The results provided in Table 2-4 show the iodine loading in terms of both grams of iodine (Q_e) and milligrams of iodine (q_e) per gram of initial sorbent. Also included is the conversion

percentage (*C*%m) based on mass change data alone. These data are also shown graphically in Figure 2-4 where the changes between the metal particles and the polymets are evident.

Table 2-4. Summary of iodine loading data for Ag, Bi, Cu, and Sn particles and metal-PAN (polymet) composites including Q_e, q_e, and *C*%m after 48 h at 120°C ± 1°C (Chong et al. 2022).

Metal	Metal Particles			Metal-PAN Composite		
	Q_e (g/g)	q_e (mg/g)	*C*%m (mass%)	Q_e (g/g)	q_e (mg/g)	*C*%m (mass%)
Ag	1.120	1120	95.2%	0.753	753	85.4%
Bi	0.773	773	42.4%	0.474	474	34.7%
Cu	1.033	1033	51.7%	1.457	1457	97.2%
Sn	3.000	3000	70.2%	1.669	1669	52.0%

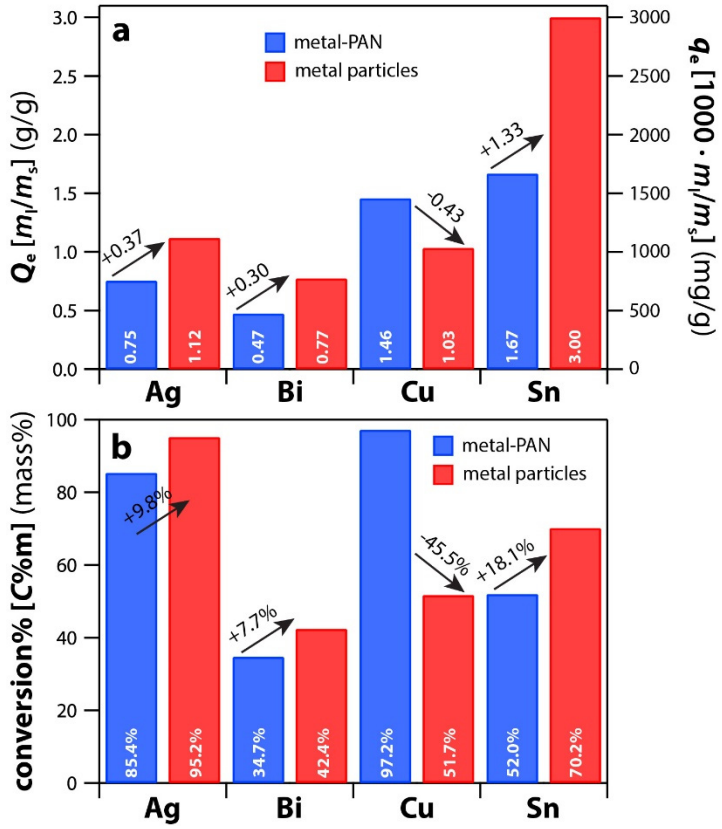

Figure 2-4. Iodine loading summary for Ag, Bi, Cu, and Sn metal particles and metal-PAN (polymet) composites including (a) the Q_e (g iodine per g of sorbent) as well as the q_e (mg iodine per g of sorbent) and (b) the conversion% (*C*%m) based on mass data alone (Chong et al. 2022).

2.4 Selection of Pelletization Process

In this project, a cold-press-and-sinter (CPS) process was utilized to make pellets. This process involves cold uniaxially pressing (CUP) the phases into a steel die and then firing the pellets. Other alternatives that would be better from multiple perspectives would be using a type of hot-pressing process. Examples of hot pressing include a hot uniaxial pressing (HUP) process such as heating the mold directly using heat tape or a heating blanket or by using a process like spark

plasma sintering (SPS) under an inert atmosphere or hot isostatic pressing (HIP). The main reason these were not used in the current work is that no HUP devices were available during the project lifecycle and PNNL does not have SPS or HIP apparatuses. It is possible to send samples out to colleagues or to industrial companies that do these types of things on pro-bono or contract bases but, for process of preserving intellectual property, these routes were not considered within the initial phase of the project.

2.5 Composite Phase Diagrams

Phase diagrams for the PAN composites (ternary diagram) discussed in this report as well as the metal-encapsulated, iodine-loaded PAN composites (quaternary diagram) are shown in Figure 2-5a and Figure 2-5b, respectively. These involve different phase proportions at different stages where, prior to iodine loading, the masses of metal in the metal-PAN composites in this study were high (≥75 mass%) with the mass balance being PAN. The iodine-loaded PAN composite can be thought of as a three-phase composite including the mass of the PAN matrix (m_{PAN}), the unreacted (residual) metal mass ($m_{m,r}$), and the mass of metal-iodide compound formed during iodine loading (m_{MI_x}). The waste form produced from this iodine-loaded includes another phase, which is the encapsulant metal phase mass ($m_{m,e}$). For the ternary in Figure 2-5a, the goal is to maximize the m_{MI_x} value while minimizing $m_{m,r}$ (meaning more metal was converted to metal-iodide) and m_{PAN}. For the quaternary shown in Figure 2-5b, the goal is to minimize the $m_{m,e}$ value (i.e., away from the top apex of the diagram) as this phase only dilutes the waste (MI_x) loading in the final form. However, a sufficient enough quantity is required to maintain good waste form integrity in order to prevent a percolation pathway through the entire waste form, i.e., creating a contiguous metal phase. Figure 2-6 covers the same information as Figure 2-5, but where the getter is not necessary a pure metal but something else (e.g., Bi_2S_3, Cu_2S) so the residual getter ($m_{g,r}$) replaces $m_{m,r}$. This is a more general way to consider these types of phase diagrams.

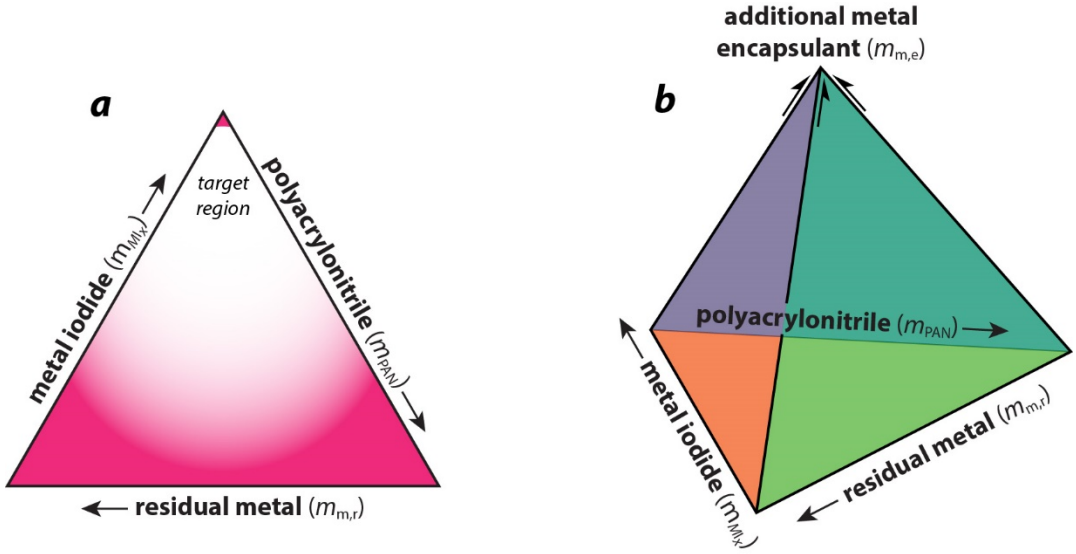

Figure 2-5. Summary of composite phase diagrams to consider when making multiphase pellets showing. (a) Ternary diagram of the PAN composite diagram representing the iodine-loaded material that has three phases including the polyacrylonitrile phase (m_{PAN}), the reacted metal iodide phase (m_{MI_x}), and the residual metal unreacted by iodine ($m_{m,r}$). (b) Quaternary diagram (triangular pyramid) providing the same diagram in (a) but with a fourth axis of the additional encapsulant metal mass ($m_{m,e}$).

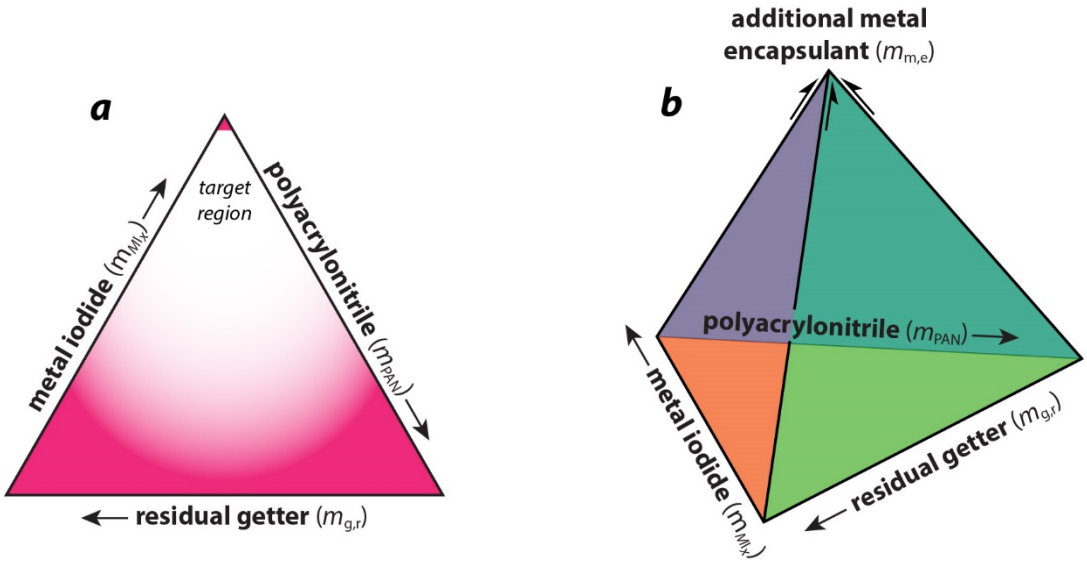

Figure 2-6. This is the same figure as Figure 2-5 but where the getter is not necessarily a pure metal phase, but it could be any chemisorbing getter compound (e.g., Bi_2S_3, Cu_2S). Summary of composite phase diagrams to consider when making multiphase pellets. (a) A ternary diagram of the PAN composite diagram representing the iodine-loaded material that has three phases including the polyacrylonitrile phase (m_{PAN}), the reacted metal iodide phase (m_{MI_x}), and the residual getter unreacted by iodine ($m_{g,r}$). (b) Quaternary diagram (triangular pyramid) providing the same diagram in (a) but with a fourth axis of the additional encapsulant metal mass ($m_{m,e}$).

2.6 Metal Iodide Decomposition and Conversion to Iodide (I^-)

It is possible to remove iodine from iodine-loaded metal getters through decomposition to iodide (I^-). If removed, the iodide could be transferred to different getter or converted to an ionic form for waste form production and ultimate iodine disposal. The side benefit to this process is that the base sorbent could potentially be recycled. Reasons why this type of iodine removal step would be attractive include:

- It could be used to recycle valuable, expensive, and limited resources (e.g., Ag) and move iodine to a long-term disposal waste form option that has higher iodine loading (e.g., PbI_2 instead of AgI) that is chemically durable but less expensive.
- Preventing the requirement of having to dispose of a waste form that contains elements regulated by the U.S. Environmental Protection Agency (EPA) under the Resource Conservation and Recovery Act (RCRA) (EPA 1980), which include Ag, As, Ba, Cd, Cr, Hg, Pb, and Se. Options for alternative non-RCRA metals to act as long-term repository options for iodine Cu (i.e., as CuI) and Bi (i.e., as BiI_3 or BiOI). This way, an effective iodine sorbent (e.g., Ag-containing zeolites) could be used to capture iodine and then it could be removed from the getter.
- Processes described herein would allow one to convert metal iodides to metal sulfides, which can also act as iodine getters (Yadav et al. 2023). Thus, the sorbent could be recycled.

Using a process described by Cao et al. (2017) [and later by Yadav et al. (2023)], AgI was decomposed in aqueous Na_2S solution where the Ag was converted to Ag_2S precipitates and the

iodine was converted to ionic iodide (I^-) in solution with Na^+; this is shown in Equation (2-1). In the study by Yadav et al. (2023), these experiments were conducted with iodine-loaded silver faujasite (i.e., AgX or IONEX Ag-400) particles and particles ground to a fine powder – see Figure 2-7. The final fate of the iodide present in solution is to immobilize it in a sodalite as NaI solution which was also demonstrated by Yadav et al. (2023) and others (Cao et al. 2017; Chong et al. 2017; Chong et al. 2018; Chong et al. 2020a) as shown in Equation (2-2).

$$2\ AgI_{(s)} + Na_2S_{(aq)} \rightarrow 2\ NaI_{(aq)} + Ag_2S_{(s)} \quad (2\text{-}1)$$

$$2\ NaI_{(s)} + 3\ Al_2Si_2O_{7(s)} + 6\ NaOH_{(s)} \rightarrow Na_8(AlSiO_4)_6I_{2(s)} + 3\ H_2O \quad (2\text{-}2)$$

Based on the work by Yadav et al. (2023), the iodine loading of AgX shows that no faujasite diffraction peaks remain after analysis with X-ray diffraction (XRD) (Figure 2-8a,b). The AgI in AgX is shown to partially convert to Ag_2S after soaking in the Na_2S solution, although AgI peaks still remain (Figure 2-8c). Also, grinding the pellets to a finer particle size provided a much higher $AgI \rightarrow Ag_2S$ conversion efficiency (CE) than leaving the Ag-400 AgX beads intact (not grinding them) as shown in Figure 2-9. As fine particles, the most effective conversion was realized with a 60°C soak temperature for 24 hours (Figure 2-9a).

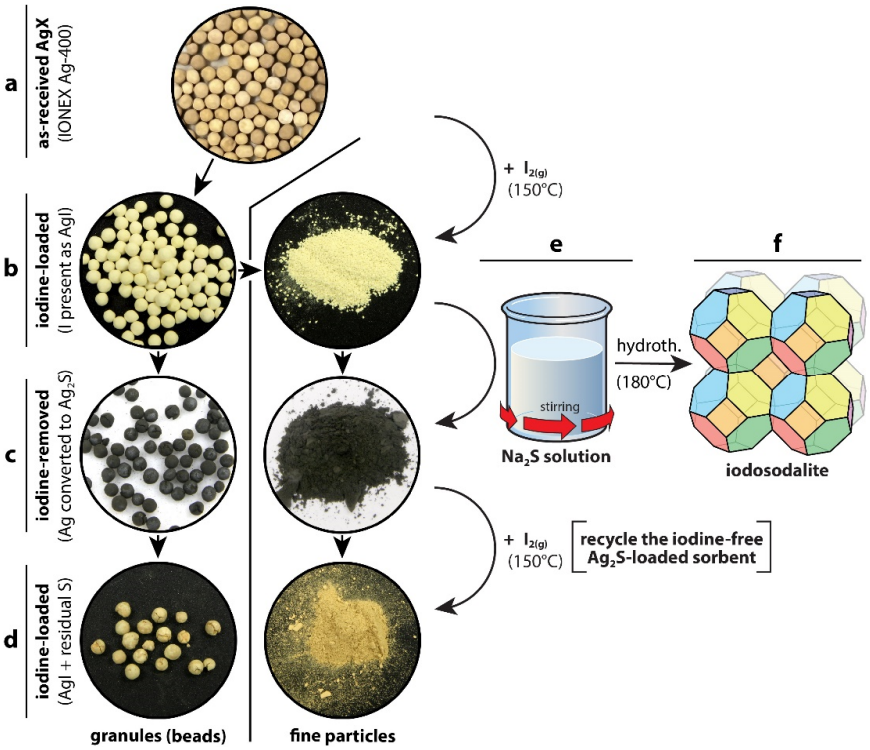

Figure 2-7. Conceptual design of metal-iodide conversion to metal-sulfide to recycle a metal-loaded sorbent from Yadav et al. (2023). Summary of experimental steps and photos of sorbents including (a) AgX sorbent, (b) AgI-containing sorbent after iodine-loading of AgX, (c) Ag_2S-containing sorbent after elution process, (d) AgI-containing sorbent after iodine-loading of Ag_2S-containing sorbent, (e, f) hydrothermal synthesis of iodosodalite. For scale, the initial size of AgX was ≈ 1.7 mm.

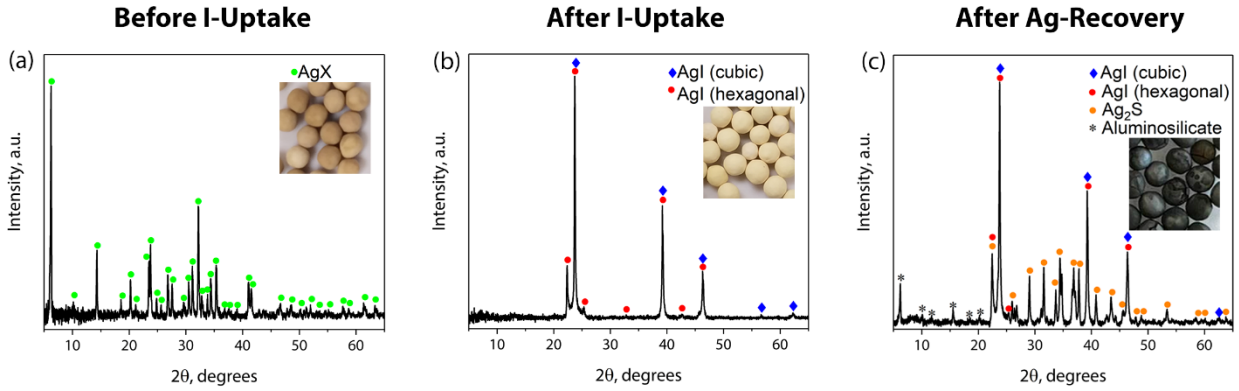

Figure 2-8. XRD patterns and optical images of (a) starting AgX sorbent, (b) AgX sorbent after iodine uptake, and (c) AgX sorbent after Ag-recovery from Yadav et al. (2023).

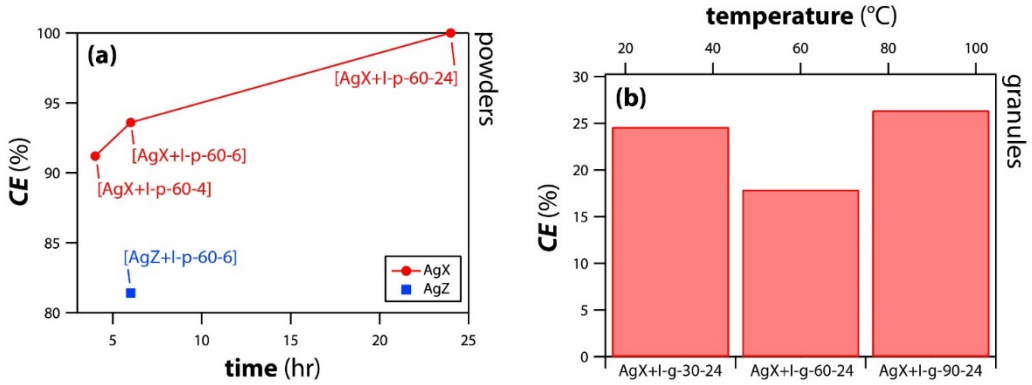

Figure 2-9 Conversion efficiency (*CE*) of AgI to Ag_2S relative to (a) time at 60°C for powders and (b) temperature for 24 hours for granules from Yadav et al. (2023). The CE value for Ag-mordenite (AgZ) (60°C for 6 hr) is shown in (a) for a comparison with the other data on AgX.

Conceptually, the same process described above for AgI reactions with Na_2S solutions could be applied to other MI_x compounds like CuI and BiI_3. Using HSC Chemistry (v9; Outotec, Finland) software, simulations were conducted to look at Gibbs free energies of formation (ΔG_f°) for the reactions[2] shown in Equation (2-3), Equation (2-4), and Equation (2-5). The reactions as a function of temperature are shown in Figure 2-10. While all of these reactions show up as spontaneous over the 0–90°C temperature regime, they all seem to be favored most towards 90°C.

$$2\ AgI_{(ia)} + Na_2S_{(ia)} \rightarrow 2\ NaI_{(a)} + Ag_2S_{(s)} \quad (2\text{-}3)$$

$$2\ BiI_{3(s)} + 3\ Na_2S_{(ia)} \rightarrow 6\ NaI_{(a)} + Bi_2S_3 \quad (2\text{-}4)$$

$$2\ CuI_{(a)} + Na_2S_{(ia)} \rightarrow 2\ NaI_{(a)} + Cu_2S_{(s)} \quad (2\text{-}5)$$

[2] Note that "a" denotes aqueous species and "ia" denotes neutral aqueous species. Not all species had data available in HSC Chemistry, so the closest options were selected for simulations. For example, no entries were available $BiI_{3(a)}$ or $BiI_{3(ia)}$ reactants, so $BiI_{3(s)}$ was used instead.

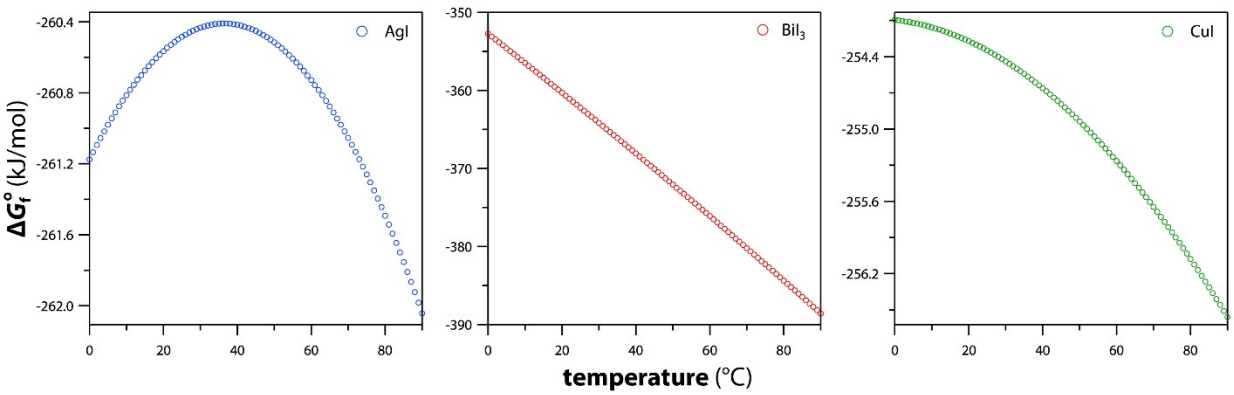

Figure 2-10. HSC Chemistry simulations for Gibbs free energies of formation (ΔG_f°) per mole (chemical potentials) for Na_2S reactions with (a) AgI, (b) BiI_3, and (c) CuI denoted in Equation (2-3), Equation (2-4), and Equation (2-5), respectively.

2.7 Metal Sulfide Reactions with Iodine Gas

Some calculations were performed using HSC Chemistry to assess thermodynamic stability of metal sulfides to react with $I_{2(g)}$ to form metal iodides. The general expected reactions for converting the MS_x compounds to MI_x compounds are provided in Equation (2-6) for Ag_2S, Equation (2-7) and Equation (2-8) for Bi_2S_3, and Equation (2-9) for Cu_2S. A graphic showing the ΔG_f° values for these compounds forming are provided in Figure 2-11 where the thermodynamic favorabilities are in the order of BiOI, BiI_3, AgI, and then CuI (i.e., BiOI is the most favored with the lowest ΔG_f° values over the temperature range of interest (0°C ≤ T ≤ 200°C). This work was documented in more detail by Riley et al. (2024).

$$Ag_2S_{(s)} + I_{2(g)} \rightarrow 2\ AgI_{(s)} + S_{(s)} \quad (2\text{-}6)$$

$$Bi_2S_{3(s)} + 3\ I_{2(g)} \rightarrow 2\ BiI_{3(s)} + 3\ S_{(s)} \quad (2\text{-}7)$$

$$Bi_2S_{3(s)} + 3\ I_{2(g)} + O_{2(g)} \rightarrow 2\ BiOI_{(s)} + 2\ I_{2(g)} + 3\ S_{(s)} \quad (2\text{-}8)$$

$$Cu_2S_{(s)} + I_{2(g)} \rightarrow 2\ CuI_{(s)} + S_{(s)} \quad (2\text{-}9)$$

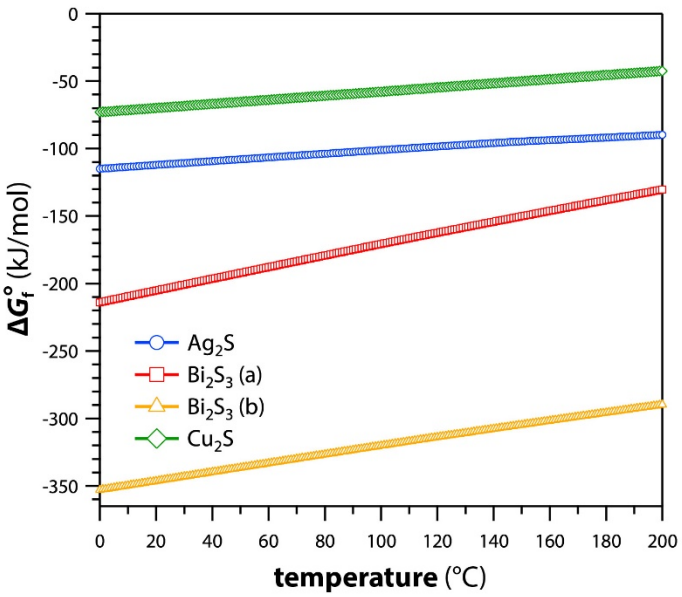

Figure 2-11. Gibbs free energies of formation (ΔG_f°) per mole (chemical potentials) for the reactions provided in Equation (2-6) [AgI formation], Equation (2-7) [i.e., BiI_3 formation], Equation (2-8) [BiOI formation], and Equation (2-9) [CuI formation], respectively.

3.0 Materials and Methods

3.1 Making PAN-Composite Beads

The polymet beads are produced through a multi-step process shown in Figure 3-1 below where the metal is Ag, Bu, Cu, or Sn but other non-metal getters can be added instead of metal. In **step-1** (Figure 3-1a), the PAN is dissolved in dimethyl sulfoxide (DMSO) in a ratio of 1 g PAN per 15 mL of DMSO using a magnetic stir bar on a stirring plate at ~500 revolutions per minute (RPM). Once dissolved, the active getter is then added in **step-2** (Figure 3-1b) and suspended within the mixture. In **step-3** (Figure 3-1c), the PAN-DMSO-metal mixture is kept suspended through vigorous mixing and it is withdrawn using a pipette and dropped into a stirring dish of chilled (T <10°C) deionized water (DIW) whereby the mixture is instantly frozen into a bead that is somewhat spherical in shape. In the final phase (**step-4**, Figure 3-1d), the beads are blotted dry with a paper towel and put into a vacuum desiccator to dry to constant mass over a few weeks. For example, a typical batch size involves 3 mL of DMSO, 0.2 g of PAN, and 0.6 g of active getter (75 mass% getter loading). All PAN material used in this study was from Dralon GmbH in the form of fibers (×100, 3.3 dtex, 60 mm; Dormagen, Germany). The DMSO was from Sigma Aldrich (≥99.9%, Sigma Aldrich).

Figure 3-1. Scheme showing how the metal-PAN composite (polymet) beads are produced (Chong et al. 2022).

The list of PAN composite beads produced during this project include the following: 75Ag-PAN, 75Bi-PAN, 75Cu-PAN, 80Cu-PAN, 90Cu-PAN, 80Cu_2S-PAN, 80Bi_2S_3-PAN, 80Ag_2S-PAN, and 90Ag_2S-PAN. These samples were made at different volume scales. The way the samples are labeled, the mass% of active getter is listed before the "-PAN" designation (where PAN makes up the remaining mass of the beads); also, the sample names are abbreviated (e.g., Ag_2S → AgS). Details for these composites are provided in Table 3-1. For making Ag-PAN, Bi-PAN, and Cu-PAN fine particles were used including -625 mesh Ag^0 (99.9%), -325 mesh Bi^0 (99.5%), and 10 µm Cu^0 (99.9%) all from Alfa Aesar. For the MS_x-PAN composites, the metal sulfides used were: Ag_2S (99.9%), Bi_2S_3 (99.9%), and Cu_2S (99.5%) from Themo Scientific. The Ag_2S particles were ground to a fine powder in a Diamonite™ mortar and pestle prior to making Ag_2S-PAN composites. For the experiments conducted herein, more details for the composites containing metal particles are provided by Chong et al. (2022). Additional details for MS_x-PAN composites are provided elsewhere (Riley et al. 2024).

Table 3-1. Summary of PAN composites produced on this project or some that were used in this study that were produced previously using a room-temperature casting temperature (T_{mix} ~ 22°C ± 1°C) including the sample identification (ID), PNNL source data from the laboratory record book, the getter mass in the batch (m_g), mass of PAN in the batch (m_{PAN}), volume of DMSO in the batch (V_{DMSO}), and the mass loading of the getter in the PAN composite ($m\%_{gL}$). For all samples, the ratio of V_{DMSO}:m_g was fixed at 15 mL:1 g, respectively. Samples 75Ag-PAN[(a)] and 75Cu-PAN are from a separate study with more details provided elsewhere (Chong et al. 2022).

Sample ID	Reference	Getter	m_g (g)	m_{PAN} (g)	V_{DMSO} (mL)	$m\%_{gL}$ (mass%)	Date
75Ag-PAN[(a)]	BNW62908-011	Ag^0	0.6015	0.2014	3.0	75%	1/27/2022
75Cu-PAN	BNW62908-011	Cu^0	0.6010	0.2002	3.0	75%	1/27/2022
75Ag-PAN[(b)]	BNW62908-050	Ag^0	0.5999	0.2006	3.0	75%	5/15/2023
75Bi-PAN	BNW62908-050	Bi^0	0.6000	0.1998	3.0	75%	5/15/2023
80Cu-PAN	BNW62908-054	Cu^0	4.0003	1.0000	15.0	80%	6/1/2023
90Cu-PAN	BNW62908-054	Cu^0	1.2000	0.1333	2.0	90%	6/1/2023
80BiS-PAN	BNW62908-054	Bi_2S_3	0.8004	0.2002	3.0	80%	6/8/2023
80CuS-PAN	BNW62908-054	Cu_2S	0.8009	0.2004	3.0	80%	6/8/2023
80AgS-PAN	BNW62908-063	Ag_2S	0.8003	0.2004	3.0	80%	8/12/2023
90AgS-PAN	BNW62908-063	Ag_2S	1.2004	0.1336	2.0	90%	8/12/2023

3.2 Evaluating Variables for PAN Composite Synthesis Process

3.2.1 Pipette Orifice Diameter Evaluation

In order to better understand the PAN composite process variables, some characterizations were done to understand the pipette tip orifice diameters and the rheological properties of the DMSO-PAN mixture. For the pipette tip orifice diameters, these were measured by cutting the tips ends off perpendicular to the central axes with a razor blade, mounting them vertically oriented on double-stick carbon tape on an aluminum disc, and images were captured with a JSM-7001F field emission gun scanning electron microscope (SEM; JSM-7001F field emission gun; JEOL USA, Inc.; Peabody, MA). Six tips were analyzed where three 1-mL and three 5-mL tips were included. For each tip, one image was collected using a long depth of field imaging mode in the JEOL software for the SEM and ≥ 11 measurements were made through the origins. Images of these tips showing the measurement process used are provided Figure 3-2.

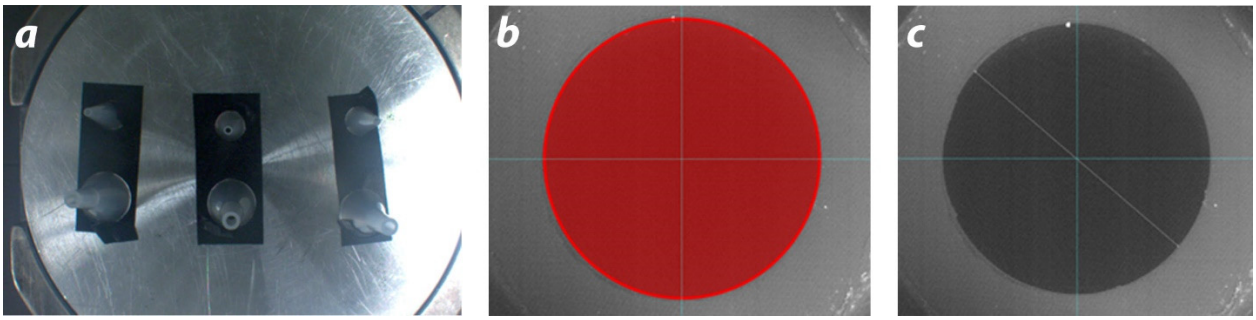

Figure 3-2. Process for measuring pipette tip orifice diameters including (a) a picture of the tips mounted for SEM analysis, (b) circle drawn to encompass the entire orifice, to find the center point, and the location of horizontal and vertical guides through the origin of the circle, and (c) an example diameter drawn through the origin to each side of the opening on that plane.

3.2.2 DMSO-PAN Solution Viscosity Evaluation

The DMSO-PAN mixture prepared for viscosity measurements was done in a 50 mL beaker including 2 g of PAN and 30 mL of DMSO. The PAN was dissolved into the DMSO through stirring with a Teflon-coated stir bar. This process took about 30 minutes before the PAN was fully dissolved within the DMSO. Once fully dissolved, the solution was transferred to a 60-mL Nalgene bottle and the bottle was capped with a lid. The viscosity measurements of this mixture were run in an RS600 (HAAKE RheoStress 600 Rheometer, Thermo Scientific) at 25°C, 40°C, 50°C, 60°C, and 70°C.

3.3 Evaluating Properties of Encapsulant Metals

The four encapsulant metals that were the focus of this study were Bi^0 (99.9%, -325 mesh), Sn^0 (99.9%, -325 mesh), $BiSn^0$ eutectic (99%, -300 mesh), and $BiPb^0$ eutectic (99.9%, -300 mesh), which were all received from American Elements. In order to determine the melting temperatures of the encapsulant metals, differential scanning calorimetry (DSC), helium pycnometry, and particle size distributions (PSDs) were measured for all materials. The purpose of the DSC runs, helium pycnometry runs, and PSD runs were to determine the $T_{m,m}$ values, bulk densities (ρ_b), and PSDs of the as-received metal particles. The DSC measurements were performed on a NETZSCH 449F1 Jupiter simultaneous thermal analyzer (STA) system. For each run, 15-20 mg of sample was placed in an alumina crucible and heated at 5 K min^{-1} to a temperature at least 50°C above the expected melting point of the metal ($T_{m,m}$). Argon was flowing at 40 mL min^{-1} over the course of the experiment. Melting points were determined by finding the onset of the endothermic melting peak. Helium pycnometry was run with an AccuPyc II 1340 (Micromeritics) whereby volume was measured ten times and the mass was measured for each sample on an analytical balance (± 0.1 mg). The PSDs were run on a Microtrac Sync unit. Particle bulk densities (ρ_b) were measured with a Micromeritics AccuPyc II 1340 helium pycnometer. Sample masses were weighed on an analytical balance to ± 0.1 mg and the instrument measured the sample volume 10× so that, with the mass value, the average ρ_b values and corresponding standard deviations (SD, i.e., ± 1σ) could be output.

3.4 Iodine Loading of Samples

Iodine loading of materials is a process by where samples are exposed to a saturated iodine atmosphere at elevated temperatures in a sealed chamber. In this study, a 1-L Savillex jar was used as the loading chamber where samples and iodine were loaded into separate glass containers. For each test, the empty glass vials were weighed with the vessel lids on (i.e., this is

the *tare mass*), samples were loaded into the vials, initial sample masses were measured, the samples were loaded into a glass dish and placed into the jar, and the lid was added to the jar. Then, the tests were initiated by placing the jar into an oven. Sometimes the vacuum oven (VO914A-1, Thermo Scientific, Lindberg Blue M) was used to run the test (with the vacuum off) so that a higher temperature precision could be obtained and other times a regular oven (3511FSQ, Isotemp, Thermo Scientific; Hampton, NH) was used. After the iodine loading duration, samples were samples were weighed after iodine loading. The temperature used for the loading was 150°C ± 5°C and the loading time was 24 h followed by 1 h of desorption at this temperature in the absence of iodine to remove any loosely bound (physisorbed) iodine. In all cases, the standard used is IONEX Ag-400 silver-exchanged faujasite zeolite. The procedures used here (e.g., temperature, time, desorption) and the Ag-400 standard used are based off of our previous work in this area (Riley et al. 2017; Chong et al. 2020b; Riley et al. 2020b; Chong et al. 2021; Riley et al. 2021a; Riley et al. 2021b; Chong et al. 2022; Riley et al. 2022a; Riley et al. 2022b; Yadav et al. 2023). The details for the samples loaded with iodine during this study are provided in Table 3-2.

Table 3-2. Description of samples for iodine loading process including the batch ID, sample description, initial sample mass ($m_{s,i}$; i.e., before iodine loading), final sample mass ($m_{s,f}$; i.e., after iodine loading), heat-treatment temperature (T_{ht}), and heat treatment time (t_{ht}) in days. Ag-400 is a commercial product (IONEX Ag-faujasite, or AgX).

Set#	ID	Description	Sample name	References	$m_{s,i}$ (g)	T_{ht} (°C)	t_{ht} (d)
1a	I-1a	75Ag-PAN	75Ag-PAN$^{(120)}$	BNW62908-11	0.0369	120	1.0
1b	I-1b	75Cu-PAN	75Cu-PAN$^{(120)}$	BNW62908-11	0.0276	120	1.0
2a	I-2a	Ag-400	Ag-400$^{(150)}$	BNW62908-53	0.2301	150	1.0
2b	I-2b	75Ag-PAN	75Ag-PAN$^{(150)}$	BNW62908-53	0.1388	150	1.0
2c	I-2c	75Cu-PAN	75Cu-PAN$^{(150)}$	BNW62908-53	0.1174	150	1.0
3a	I-3a	75Ag-PAN	75Ag-PAN$^{(130)}$	BNW62908-57	0.7213	130	4.90
3b	I-3b	75Bi-PAN	75Bi-PAN$^{(130)}$	BNW62908-57	0.7290	130	4.90
3c	I-3c	AC-6120	AC-6120$^{(130)}$	BNW62908-57	0.1001	130	4.90
3d	I-3d	Ag-400	Ag400$^{(130)a}$	BNW62908-57	0.0979	130	4.90
4a	I-4a	BiS-PAN	80BiS-PAN$^{(130)}$	BNW62908-62	0.1516	130	4.94
4b	I-4b	CuS-PAN	80CuS-PAN$^{(130)}$	BNW62908-62	0.1546	130	4.94
4c	I-4c	80Cu-PAN	80Cu-PAN$^{(130)}$	BNW62908-62	0.1530	130	4.94
4d	I-4d	90Cu-PAN	90Cu-PAN$^{(130)}$	BNW62908-62	0.1540	130	4.94
4e	I-4e	Ag-400	Ag400$^{(130)b}$	BNW62908-62	0.1256	130	4.94
5a	I-5a	80AgS-PAN	80AgS-PAN$^{(130)}$	BNW62908-66	0.1194	130	4.89
5b	I-5b	90AgS-PAN	90AgS-PAN$^{(130)}$	BNW62908-66	0.1585	130	4.89
5c	I-5c	Ag-400	Ag-400$^{(130)c}$	BNW62908-66	0.1305	130	4.89

After loading, several calculations were made that included the mass change, where all gained mass was assumed to be iodine (m_I), using Equation (3-1) through a difference between final sample mass ($m_{s,f}$) and initial sample mass ($m_{s,i}$). Once m_I is known, the iodine loading can be calculated using the Q_e term [Equation (3-2)] in grams of iodine per gram of starting sorbent or q_e [Equation (3-3)], which is the same but in milligrams of iodine instead of grams of iodine.

$$m_I = m_{s,f} - m_{s,i} \quad (3\text{-}1)$$

$$Q_e = {}^{m_I}/_{m_{s,i}} \text{ (in g/g)} \quad (3\text{-}2)$$

$$q_e = {}^{m_I}/_{m_{s,i}} \text{ (in mg/g)} \quad (3\text{-}3)$$

Assuming that all iodine is loaded directly onto the metal particles through chemisorption and results in the formation of a metal-iodide complex (MI_x), the maximum iodine mass possible ($m_{I,max}$) [Equation (3-4)], the mass of MI_x formed [m_{MI_x}; see Equation (3-5)], and the residual/unreacted metal mass [$m_{m,r}$; Equation (3-6)] can be calculated. For Equation (3-4), mf_{ML} is the mass fractional metal loading in the sorbent,[3] x_I is the molecular weight of iodine (i.e., 126.9045 g/mol), M_I is the moles of iodine in the MI_x compound (e.g., 1 for AgI, CuI, and BiOI and 3 for BiI_3), and x_m is the molecular weight of the metal getter in the sorbent. For Equation (3-5), x_{MI_x} is the molecular weight of the MI_x compound and the other variables were defined previously. The $m_{m,r}$ values are calculated with Equation (3-6) by difference of several other parameters previously calculated. Finally, the mass% conversion (*C%*m) of the metal can be calculated using Equation (3-7) (note that an assumption with this calculation is that all mass gained is iodine loading).[4]

$$m_{I,max} = {}^{(m_s \cdot mf_{ML} \cdot x_i \cdot M_I)}/_{x_m} \quad (3\text{-}4)$$

$$m_{MI_x} = {}^{(m_I \cdot x_{MI_x})}/_{(x_I \cdot M_I)} \quad (3\text{-}5)$$

$$m_{m,r} = m_{s,f} - m_{PAN} - m_{MI_x} \quad (3\text{-}6)$$

$$C\%m = {}^{m_I}/_{m_{I,max}} \cdot 100 \quad (3\text{-}7)$$

3.5 Making Pellets

The general layout of the pellet die (diameter = 10 mm, radius = 5 mm) being used in this work is shown in Figure 3-3. The pellet making process was varied with this work depending on several variables being explored where different numbers of layers were included in pellets. For multi-layer pellets, the anvil and previously pressed layers were left in the cylinder, but the ramrod was removed for each subsequent pelletization layer being pressed. Sometimes the pressures differed between the different layers in multi-layer pellets. This was done because it is nearly impossible to reinsert a pellet into the cylinder once it has been removed.

[3] As examples, mf_{ML} = 1 if the sorbent is a pure metal and mf_{ML} = 0.75 if the metal loading in a metal-PAN composite is 75 mass%.
[4] This calculation disregards the possibility that increased mass is attributed to water adsorption/absorption.

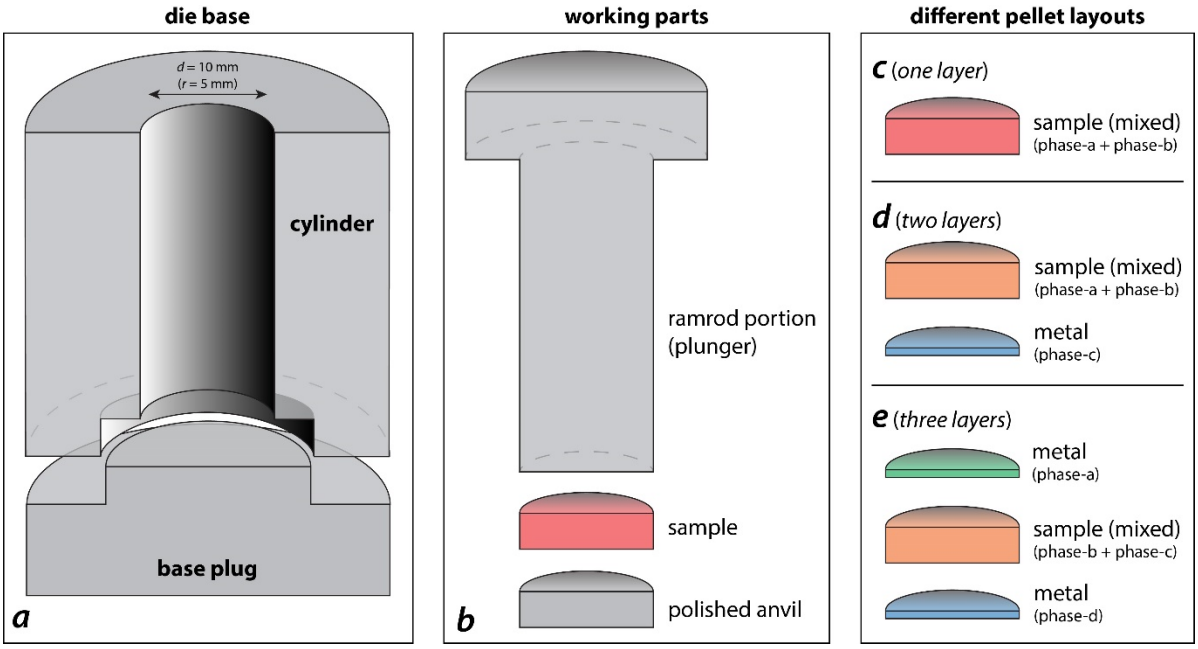

Figure 3-3. Schematic showing the (a) pellet die base (cylinder and base plug), (b) additional parts and where the sample fits (the ramrod, sample, and anvil), and (c–e) different pellet layouts with differing numbers of phases. An alternative approach is to use a polished anvil above and below the sample, not just below as shown in the diagram.

3.5.1 Making Two-Phase Pellets

To make pellets, several physical properties and parameters of each different phase were considered so that pellets of similar dimensions could be produced. Pellets were produced in similar sizes to start this process. The initial pellet sizes produced were ~2.5 mm in height (h) and 10 mm in diameter (radius, r, of 5 mm) with an approximate green pellet volume ($V_{p,g}$) of 196.35 mm^3 (0.19635 cm^3) calculated using Equation (3-8). The method for calculating the total mass of material needed to achieve this target pellet volume included formulation in Microsoft Excel based off Equation (3-9) using the *goal seek* function to determine target masses of phase-a ($m_{p\text{-}a}$; waste-containing material, i.e., ceramic or halide phase) and phase-b ($m_{p\text{-}b}$; encapsulant metal) to achieve a specific target waste loading in mass% ($WL_{m\%}$) utilizing the densities of each phase [Equation (3-10)], i.e., $\rho_{p\text{-}a}$ and $\rho_{p\text{-}b}$, respectively.

$$V_{p,g} = \pi r^2 h \tag{3-8}$$

$$V_{p,g} = {}^{m_{p-a}}/_{\rho_{p-a}} + {}^{m_{p-b}}/_{\rho_{p-b}} = 0.19635 \text{ cm}^3 \tag{3-9}$$

$${}^{m_{p-a}}\Big/_{(m_{p-a} + m_{p-a})} \cdot 100 = WL_{m\%} \tag{3-10}$$

Once the phase-a and phase-b masses were determined, these were weighed out on an analytical balance (ME204E; Mettler Toledo, Columbus, OH; ± 0.1 mg), mixed together on weight paper for 1 minute, and then loaded into the chamber of a 10-mm diameter steel die. The die was loaded into a uniaxial press (model 3393, Carver, Inc.), and a 1000 pounds per square inch (PSI) (3.1 metric tons) load was applied for 1 minute; for some pellets a 1500 PSI (5.0 metric tons) load was used on the gauge. After 1 minute of applied load, the load was released, and the pellet was

recovered from the die. Using Equation (3-11) modified (corrected) from the original (MTI 2023), the actual applied load pressure (P_A) during this process was calculated where T is the force applied (in metric tons) on the hydraulic cylinder, g is the acceleration due to gravity (9.8 m/s^2), and r is the radius of the die (in meters).[5] The other option is to divide the force applied (F_A) by the area of the die face (A_d) to get the applied pressure (P_A) as shown in Equation (3-12).

$$P_A = {(T \cdot g)}/{(\pi r^2)} \quad (3\text{-}11)$$

$$P_A = {F_A}/{A_d} \quad (3\text{-}12)$$

Once the pellets were removed from the die, the green pellet masses ($m_{p,g}$) were taken and the $V_{p,g}$ was calculated using calipers where a few different measurements were taken of the diameter and the thickness so that averages could be calculated. After pellets were prepared, they were heat treated for different temperatures, different times, and in different atmospheres and these details are provided in Table 3-3. The AgI used here was 99.999% (Alfa Aesar) and CuI was 99.998% (Thermo Scientific).

Table 3-3. Summary of processing details for two-phase pellets where phase-a is the material to be encapsulated and phase-b is the encapsulant phase (metal), h is the target pellet thickness (height, averaged), $m_{p,g}$ is the green pellet mass, Atm is the atmosphere (air or vacuum), T_{ht} is the heat treatment temperature, t_{ht} is the heat treatment time, Ramp is the ramp rate used for some of the pellets, $WL_{I,m}$ is the expected mass loading of iodine in the composite waste form, and $WL_{MI,v}$ is the expected volumetric loading of the MI_x compound in the final composite. [(t)]Denotes target (not measured) value.

ID	Phase-a	Phase-b	h (mm)	$m_{p,g}$ (g)	Atm	T_{ht} (°C)	t_{ht} (h)	Ramp (°C/min)	$WL_{I,m}$ (m%)	$WL_{MI,v}$ (vol%)
1a	–	100%Bi	1.55 ± 0.03	1.1419	Air	203	22	5	–	–
2a	–	100%Bi	2.5[(t)]	1.9239	Air	203	8	5	–	–
2b	10%Al_2O_3	90%Bi	2.5[(t)]	1.6712	Air	203	8	5	–	–
2c	15%Al_2O_3	85%Bi	2.5[(t)]	1.5697	Air	203	8	5	–	–
3a	–	100%Bi	2.59 ± 0.02	1.9108	Vac	203	22	–	–	–
3b	15%AgI	85%Bi	2.56 ± 0.01	1.7091	Vac	203	22	–	8.11	23.3
3c	30%AgI	70%Bi	2.58 ± 0.03	1.5628	Vac	203	22	–	16.22	42.5
4a	30%CuI	70%Bi	2.59 ± 0.02	1.5599	Vac	203	20	–	19.99	42.5
5a	30%CuI	70%BiSn	2.57 ± 0.01	1.4447	Air	104	8	5	19.99	39.3
5b	30%AgI	70%BiSn	2.61 ± 0.07	1.4484	Air	104	8	5	16.22	39.2

3.5.2 Making Three-Phase Pellets

The calculations for making three-phase pellets (i.e., metal, polymer, and ceramic/halide phases) that included the PAN phase were more complicated as they assume the following: (1) an even metal loading across all metal-PAN composites, (2) an even iodine loading across all metal-PAN composites, (3) that no mass changes occurred after iodine loading (due to water absorption from the air), and (4) that the PAN does not decompose during the iodine loading process. Thus, similar equations to those above were used here with a few adjustments described below in more detail.

[5] For a 1-cm diameter die (0.005-m radius) the P_A values for pellets pressed at 1000 PSI and 1500 PSI were calculated as 387 MPa and 624 MPa, respectively.

After loading the metal-PAN composites with iodine, not all of the metal reacts with iodine according to mass changes (before and after the iodine loading tests) alone. This means that some residual metal mass ($m_{\mathrm{m,r}}$) remains in the beads and this has to be accounted for when calculating the overall composite volume after iodine loading ($V_{\mathrm{polymet+I}}$), which is defined in Equation (3-13). The three components in this calculation include the PAN matrix (m_{PAN} and ρ_{PAN}), the metal-iodide (m_{MI_x} and ρ_{MI_x}), and the residual metal ($m_{\mathrm{m,r}}$ and $\rho_{\mathrm{m,r}}$) where the desired masses of all components were calculated using the same *goal seek* function in Excel as mentioned in Section 3.5.1. From these calculations, the mass of iodine waste loading ($WL_{\mathrm{I,m}}$) and volumetric waste loading of the MI_x complex ($WL_{\mathrm{MI,v}}$) can be calculated using Equation (3-14) and Equation (3-15), respectively, including the volume of the encapsulant metal phase ($V_{\mathrm{m,e}}$).

$$V_{\mathrm{polymet+I}} = {m_{\mathrm{PAN}}}/{\rho_{\mathrm{PAN}}} + {m_{MI_x}}/{\rho_{MI_x}} + {m_{\mathrm{m,r}}}/{\rho_{\mathrm{m,r}}} = 0.19635 \text{ cm}^3 \quad (3\text{-}13)$$

$$WL_{\mathrm{I,m}} = 100 \cdot {m_{\mathrm{I}}}/{\left(m_{\mathrm{PAN}} + m_{MI_x} + m_{\mathrm{m,r}}\right)} \quad (3\text{-}14)$$

$$WL_{\mathrm{MI,v}} = {V_{MI_x}}/{\left(V_{\mathrm{polymet+I}} + V_{\mathrm{m,e}}\right)} \quad (3\text{-}15)$$

For making the 3-phase pellets, a few different ideas were evaluated, and these are shown graphically in Figure 3-4. A summary these pellets produced is provided in Table 3-4.

1. ***Initial thin pellet layer***. Pressing the polymer-containing phase in between different pure metal layers. To evaluate this option, work was done to look at how difficult it would be to press pellets that were <1 mm with the target thickness of ~0.5 mm (500 µm). The pressing pressure for these thin discs was 1000 PSI (3.1 metric tons) on the Carver press gauge. This worked well so the next step was conducted. This is shown graphically in Figure 3-4a.

2. ***Adding polymer-containing layer with metal filler (2-layer)***. Adding the polymer-containing layer was done by loading the MI_x-PAN material on top of the thin bottom metal pellet, loading the metal powder in with the MI_x-PAN material, and pressing at higher pressures on the Carver press (1500 PSI or 5.0 metric tons) gauge. When doing this, it was clear that the portions of the MI_x-PAN remained uncovered by metal so it was decided that a top metal layer should be added in the subsequent 3rd layer approach. This is shown graphically in Figure 3-4b.

3. ***Adding a top metal layer to the 2-layer approach (3-layer)***. The 3-layer approach was done the same as the 2-layer approach, but after the 2-layer pellet was pressed, additional Bi^0 particles were added to the die, and the mixture was pressed at 1000 PSI (3.1 metric tons). This is shown graphically in Figure 3-4c.

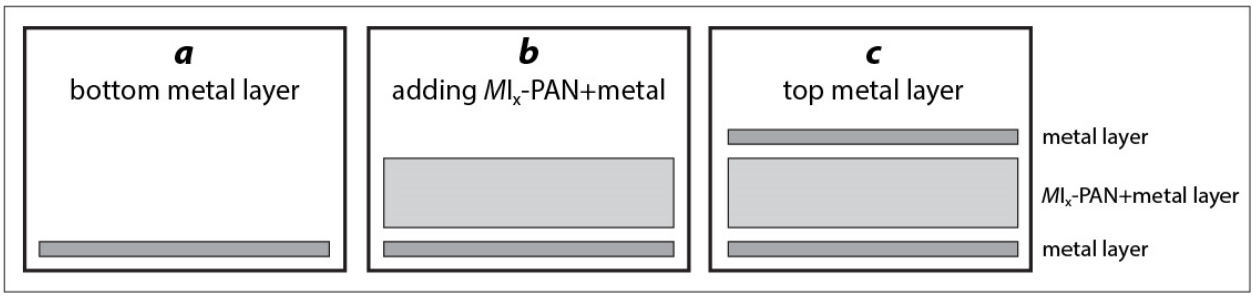

Figure 3-4. Schematic for how the 2-layer and 3-layer pellets were produced showing (a) the thin metal layer, (b) the middle layer containing the MI_x-PAN mixed with metal phase, and (c) the top metal layer.

No material grinding was performed when making the Set-6 pellets (Set-6b and Set-6c) whereas samples were ground to a finer particle size for Set-7 pellets (Set-7d and Set-7e). To do the grinding process, beads were placed between two weigh boats and crushed. This process prevents significant loss of material onto the surfaces of a mortar and pestle or due to samples jumping out of the container holding them during grinding. This method also allows for easy transfer of the crushed material afterwards since they are already in a weigh boat.

Table 3-4. Experimental details for 3-phase pellets where Phase-a, Phase-c, and Phase-d denote the encapsulant metal and Phase-b is the material to be encapsulated, h is the target pellet thickness (height, averaged), $m_{p,g}$ is the green pellet mass, t_{ht} is the heat treatment time, $WL_{I,m}$ is the expected mass loading of iodine in the composite waste form, and $WL_{MI,v}$ is the expected volumetric loading of the MI_x compound in the final composite. All pellets in this table were fired under vacuum (atm) at 203°C (T_{ht}). For more information on the Phase-b sources, see Table 3-2.

ID	Phase-a	Phase-b	Phase-c	Phase-d	Phase-a (mass, g)	Phase-b (mass, g)	Phase-c (mass, g)	*Phase-d (mass, g)*	*h* (mm)	$m_{p,g}$ (g)	t_{ht} (h)	$WL_{I,m}$ (m%)	$WL_{MI,v}$ (vol%)
6a	100Bi	–	–	–	0.3838	–	–	–	0.56	0.3753	22	–	–
6b	100Bi	75Ag-PAN$^{(150)}$	100Bi	–	0.3848	0.1112	0.6337	–	1.83	1.1170	22	4.47%	13.64%
6c	100Bi	75Ag-PAN$^{(150)}$	100Bi	100Bi	0.3835	0.1274	0.6288	0.3834	2.55 ± 0.13	1.5111	22	3.80%	11.67%
7a	100Bi	–	–	–	0.3842	–	–	–	0.54 ± 0.02	0.3370	20	–	–
7b	100Bi	–	–	–	0.3072	–	–	–	0.47 ± 0.02	0.3011	20	–	–
7c	100Bi	–	–	–	0.2308	–	–	–	0.36 ± 0.01	0.2257	20	–	–
7d	100Bi	75Cu-PAN$^{(150)}$	100Bi	100Bi	0.2310	0.1889	0.4125	0.2312	2.16 ± 0.02	1.0483	20	10.45%	23.81%
7e	100Bi	Ag-400$^{(150)}$	100Bi	100Bi	0.2303	0.2064	0.4154	0.2309	1.93 ± 0.04	1.0653	20	4.48%	25.41%

For each pellet, data was measured or calculated for each of the parameters (properties) described in Table 3-5.

Table 3-5. Summary of properties measured for pellets produced under this project.

Property/Information	Description
Sample Number	Identification of the sample based on Set-# and letter identification
Alternative ID	Includes the general composition (if easily written) for each pellet[(a)]
Date	The date when the sample was put into the oven or furnace for heat treatment
Iodine loading (source)	Location in report where data is provided for iodine loading of the base sorbent
Phase-a (composition)	Description of phase-a in the pellet
Phase-b (composition)	Description of phase-b in the pellet
Phase-c (composition)	Description of phase-c in the pellet
Phase-d (composition)	Description of phase-d in the pellet
Phase-a (mass, g)	Mass of phase-a weighed out for making the pellet
Phase-b (mass, g)	Mass of phase-b weighed out for making the pellet
Phase-c (mass, g)	Mass of phase-c weighed out for making the pellet
Phase-d (mass, g)	Mass of phase-d weighed out for making the pellet
C%m (MI_x, m%)	Conversion (mass%) of metal iodide (MI_x) based on starting metal in composite
mf_I (mass fraction)	Mass fraction of iodine in MI_x compound
$t_{p,g}$ (mm)	Thickness of green pellet (before sintering)
$m_{p,g}$ (g)	Mass of green pellet (before sintering)
Atmosphere type	Atmosphere used for sintering pellet[(a)]
T_{ht} (°C)	Heat treatment (sintering) temperature
t_{ht} (h)	Heat treatment (sintering) time
Ramp (°C/min)	Ramp rate used for heat treatment (sintering)
$t_{p,f}$ (mm)	Thickness of fired pellet (after sintering)
$m_{p,f}$ (g)	Mass of fired pellet (after sintering)
Δm (m%)	Change in mass from before to after firing process (sintering)
ρ_b (g/cm^3)	Bulk density
$\rho_{b,em}$ (g/cm^3)	Bulk density of encapsulant matrix (e.g., metal envelop phase)
$\rho_{b,MIx}$ (g/cm^3)	Bulk density of the MIx complex
$WL_{I,m}$ (m%)	Waste loading of iodine in final form in terms of mass%
V_{MIx}/m_{LS} (cm^3/g)	Volume of MI_x complex per mass of iodine-loaded PAN composite
V_{tot}/m_{LS} (cm^3/g)	Total volume of iodine-loaded PAN composite per mass of loaded sorbent
$WL_{MI,v}$ (vol%)	Waste loading (vol%) based only on incorporation of MI_x complex
$V_{\%T}$ (vol%)	Volume of final form based on predicted total volume

[(a)]note that (v) denotes vacuum was used as the atmosphere.

3.5.3 Making Pellets with Greater Than Three Phases (Conceptual Idea)

Some additional pellet concepts were considered where, instead of using metals as the getters inside a PAN matrix, metal-sulfides (MS_x; i.e., Ag_2S, Bi_2S_3, Cu_2S) were used where reacting the sulfides with iodine results in residual S. Thus, MS_x-PAN composites loaded with iodine contain four distinctly separate phases of PAN, MI_x, S, and residual MS_x where adding an encapsulant metal phase will lead to a five-phase composite material. The general expected reactions for converting the MS_x compounds are provided in Equation (3-16) for Ag_2S, Equation (3-17) and Equation (3-18) for Bi_2S_3, and Equation (3-19) for Cu_2S (note that these equations are reiterations of details provided in Section 2.7). A graphic representation of how these phases are distributed is presented in Figure 3-5.

$$Ag_2S_{(s)} + I_{2(g)} \rightarrow 2\ AgI_{(s)} + S_{(s)} \quad (3\text{-}16)$$

$$Bi_2S_{3(s)} + 3\ I_{2(g)} \rightarrow 2\ BiI_{3(s)} + 3\ S_{(s)} \quad (3\text{-}17)$$

$$Bi_2S_{3(s)} + 3\ I_{2(g)} + O_{2(g)} \rightarrow 2\ BiOI_{(s)} + 2\ I_{2(g)} + 3\ S_{(s)} \quad (3\text{-}18)$$

$$Cu_2S_{(s)} + I_{2(g)} \rightarrow 2\ CuI_{(s)} + S_{(s)} \quad (3\text{-}19)$$

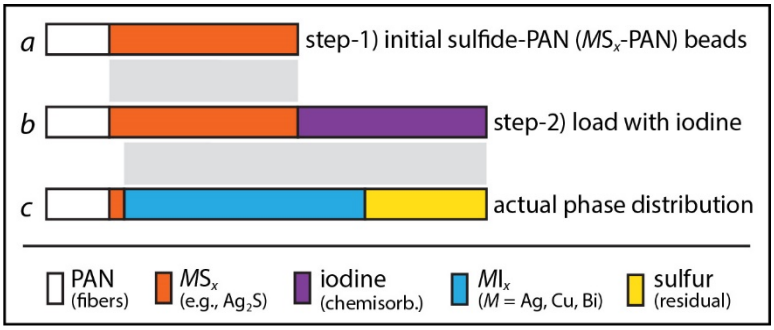

Figure 3-5. Graphic representation of multi-phase sorbent after iodine reaction showing (a) the initial MS_x-PAN composite, (b) the MS_x-PAN composite after iodine loading, and (c) the phase distribution of (b); note that these values are arbitrarily shown as an example.

Considering sorbents containing metal-sulfides (MS_x), assuming the iodine-loading process fully reacts the metal from the MS_x compound into MI_x, the resulting sorbent will contain elemental sulfur [see Equation (2-6), Equation (2-7), Equation (2-8), and Equation (2-9)], which is defined here as $m_{Sulf,L}$ in Equation (3-20). This value of $m_{Sulf,L}$ is defined as the difference of the total loaded sorbent mass ($m_{s,f}$), the mass of MIx present in the loaded sorbent ($m_{MIx,L}$) and the PAN mass (for PAN composites; $m_{PAN,L}$). While this work was not completed within the scope of this project, a paper was published summarizing the development of MS_x-PAN composites for iodine capture (Riley et al. 2024).

$$m_{\mathrm{Sulf,L}} = m_{\mathrm{s,f}} - m_{\mathrm{MIx,L}} - m_{\mathrm{PAN,L}} \quad (3\text{-}20)$$

3.6 Evaluating PAN Removal After Iodine Loading

During the course of this work, a process was proposed for removing the PAN matrix phase after iodine loading of PAN composite sorbents as is shown schematically in Figure 3-6. Since having PAN present in the sample leads to thermal limits for the consolidation process due to the low PAN decomposition temperature of 175°C (see T_d in Table 2-3), removing the PAN phase prior to decomposition would make the consolidation process more flexible. It also removes the concerns of unwanted reactions between the polymer phase and the other phases as well as the unknown degradation properties of the polymer phase over long time periods. Overall, removing the PAN phase is a benefit for several reasons, but the added drawback is that it adds more steps in the process and produces another waste stream containing DMSO. Another point of concern here is that the MI_x complexes could dissolve in the DMSO, and it is possible that some iodine is encapsulated directly in the PAN matrix (Riley et al. 2021a) that could also become mobile upon PAN dissolution with DMSO.

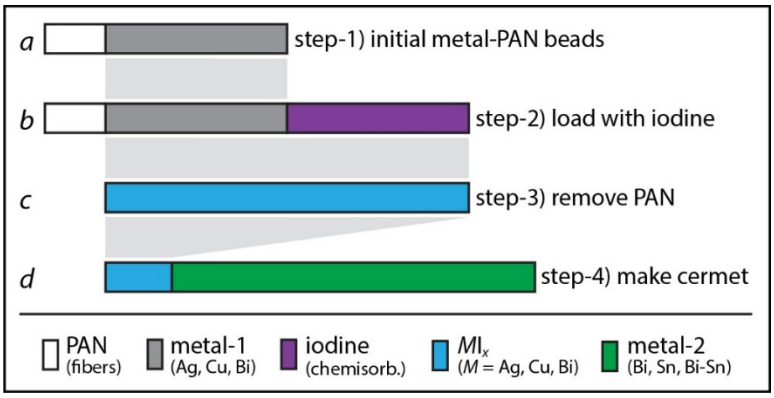

Figure 3-6. Schematic of the proposed method for removing PAN from iodine-loaded PAN composites followed by cermet/halmet synthesis. Note that a large volume of metal-2 is used to encapsulate the MI_x complex.

For this set of experiments, different batches of beads were fabricated including 75Ag-PAN[(b)] and 75Bi-PAN (see Table 3-1). A key difference in this experiment from prior PAN composite fabrication processes was that all of the residual material was captured from the process including material often discarded as waste. This "waste" material includes the material left in the glass beaker (i.e., "vessel-1" container in Figure 3-1b,c), material left in the pipette used to drop beads into the stirring DIW (i.e., see pipette in Figure 3-1c), and all of the debris in the DIW dish resulting from bead creation (i.e., "vessel-2" container in Figure 3-1c). After bead fabrication using the process described previously (see Section 3.1; specifically Figure 3-1), the beads were loaded into a plastic weigh boat, gently dried with paper towels and then all of the materials from each batch were placed into separate tared 20-mL scintillation vials. The vials were capped but the lids were not screwed on tight and then each vial was placed into a glass vacuum desiccator to dry over the course of several weeks.

After drying the batches of 75Ag-PAN[(b)] and 75Bi-PAN, the entire batches were loaded with iodine in a single run within the 1 L Savillex jar at 130°C for 4.9 days – these samples were 75Ag-PAN[(130)] (I-3b) and 75Bi-PAN[(130)] (I-3c) in Table 3-2. An additional sample evaluated in these experiments was the CuI-PAN[(150)] (I-2c) in Table 3-2. To run DMSO-PAN dissolution tests, it was unclear how the PAN phase would behave. For these tests, pellets were added to 20-mL glass scintillation vials with small magnetic stir bars. For AgI-PAN[(130)] and BiI-PAN[(130)], the beads were crushed before they were loaded into the containers while the CuI-PAN[(150)] beads were not crushed beforehand. DMSO was added to the containers during stirring (i.e., 500-580 RPM) and images were taken of the samples at different time intervals. Experimental details are provided in Table 3-6.

Table 3-6. Summary of experiments performed for PAN removal using DMSO after iodine loading of PAN composites. The ID# denotes the details for the starting sorbent from Table 3-2, $m_{s,d}$ is the sample mass for dissolution tests, and V_{DMSO} is the volume of DMSO added to each vial.

ID#	Getter	Sample ID	Reference	Morphology	$m_{s,d}$ (g)	V_{DMSO} (mL)
I-2c	Cu^0	CuI-PAN(150)	BNW62908-59	Intact	0.0670	3.0
I-3a	Ag^0	AgI-PAN(130)	BNW62908-61	Crushed	0.0317	3.0
I-3b	Bi^0	BiI-PAN(130)	BNW62908-61	Crushed	0.0288	3.0
I-4a	Bi_2S_3	80BiS-PAN(130)	BNW62908-64	Crushed	0.0474	2.0
I-4b	Cu_2S	80CuS-PAN(130)	BNW62908-64	Crushed	0.0516	2.0
I-4c	Cu^0	80Cu-PAN(130)	BNW62908-64	Crushed	0.0611	2.0
I-4d	Cu^0	90Cu-PAN(130)	BNW62908-64	Crushed	0.1146	2.0

After dissolution in PAN, two samples [i.e., AgI-PAN(130) and BiI-PAN(130)] were processed further based on the most promising initial results. The contents of each sample vial (i.e., DMSO mixed with samples, including both soluble and insoluble materials) were transferred to a 50-mL conical centrifuge tube and allowed to settle for 7 days. After this, the DMSO was removed from the vial and saved in case it was needed later. Then, 4 mL of DIW was added to each vial and mixed with a small magnetic stir bar (from the original glass scintillation vial). The DIW was allowed to sit for 7 days in the container. After this 7-day period, the tubes were loaded into a centrifuge (Sorval Legend Mach 1.6, Thermo Fisher Scientific) and run for 5 minutes at 2500 RPMs. The liquid was pipetted off the pelletized solids at the bottom, fresh 4 mL DIW was added, and stirred again with the stir bar. The centrifugation step was repeated as before, the stir bar was removed, the DIW was discarded, and the centrifuge tubes containing the residual solids were placed inside a glass vacuum desiccator at room temperature to dry. Additional studies were performed with the I-4 set of samples including 80BiS-PAN(130), 80CuS-PAN(130), 80Cu-PAN(130), and 90Cu-PAN(130) (see Table 3-2 and Table 3-6). These samples were processed the same way as the others discussed above but were left to stir for 11 days at room temperature. All of the Cu-containing materials appeared very dark and seemed to dissolve the sample. Thus, they were not further processed.

3.7 Pellet Characterization

3.7.1 Images and Optical Microscopy

Images of pellets were taken with a digital camera or an iPhone. Optical microscopy (OM) was performed on all samples after pellets were mounted in epoxy and cross-sectionally polishing. The OM was done on a VHX-7000 (Keyence Corporation of America, Itasca, IL) using a 20-200× objective and coaxial lighting.

3.7.2 Scanning Electron Microscopy and Energy Dispersive X-Ray Spectroscopy

All SEM was performed on a JSM-7001F field emission gun SEM using probe current 13-15, 15 kV acceleration voltage, and imaging was done with backscattered electron (BSE) and secondary electron (SEI) detectors. Energy dispersive X-ray spectroscopy (EDS) was performed using dual Bruker xFlash 6|60 (Bruker AXS Inc., Madison, WI) mounted at different angles off the X-ray collection cone.

3.7.3 Bulk Density Measurements (Helium Pycnometry)

Bulk densities (ρ_b) of materials were measured using an AccuPyc II 1340 helium pycnometer (Micromeritics instrument Corporation, Norcross, GA). To run these experiments, samples were weighed on an analytical balance through difference in mass by taring the sample cup mass before adding sample and then 10 volumetric measurements were measured with the instrument. Using the volumetric data coupled to the mass entry, the instrument software output an average density value with associated SD values.

3.8 General Material Characterizations

Characterizations were performed on different raw materials and produced composites at different phases within the project. XRD analyses were performed on raw materials (i.e., Bi^0, Sn^0, $BiSn^0$), the unloaded PAN composites, and iodine-loaded PAN composites. XRD analysis was performed using a Bruker® D8 Advance (Bruker AXS Inc., Madison, WI) XRD with Cu Kα emission. The detector used was a LynxEye™ position-sensitive detector with a collection window of 3° 2θ. Scan parameters were generally within the 10–70° 2θ scan range with a step of 0.02° 2θ and a 1-s dwell at each step. Scanning electron microscopy was performed using a JSM-7001F field-emission gun microscope (JEOL USA, Inc.; Peabody, MA). EDS was performed using a Bruker xFlash 6|60 (Bruker AXS Inc., Madison, WI) detector.

4.0 Results and Discussion

4.1 Evaluating Variables for PAN Composite Synthesis Process

4.1.1 Pipette Orifice Diameter Evaluation

The SEM micrographs of the 1-mL and 5-mL pipette tips are shown in Figure 4-1 and the tabulated results are provided in Table 4-1. The average values for the 1-mL and 5-mL diameters were 732.1 (8.4) and 1379.3 (14.5) µm, respectively. Looking at the micrographs in Figure 4-1, it is also clear that the 5-mL tips (Figure 4-1b) were far more regular in shape with less debris on the tips than the 1-mL tips (Figure 4-1a).

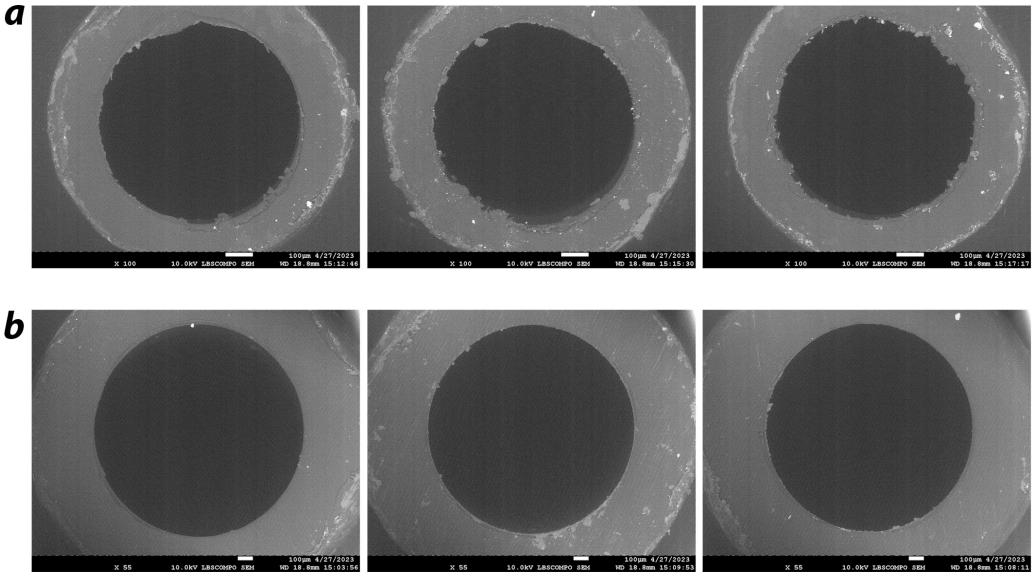

Figure 4-1. SEM micrographs of (a) 1-mL pipette tips and (b) 5-mL pipette tips.

Table 4-1. Summary of 1-mL and 5-mL pipette orifice sizes (µm) including average (AVE) and standard deviation (SD, in parenthesis) values for each tip and each set of tips from each set.

Pipette tip size: 1 mL (µm)			Pipette tip size: 5 mL (µm)		
Tip-1	**Tip-2**	**Tip-3**	**Tip-**	**Tip-21**	**Tip-3**
737.2	730.8	727.1	1383.1	1362.7	1364.4
732.5	730.1	719.7	1381.2	1361.0	1362.4
705.2	733.5	722.7	1377.0	1361.2	1366.3
738.3	734.3	725.8	1379.8	1360.0	1371.2
716.0	722.6	727.5	1386.5	1364.3	1364.6
726.5	733.8	741.9	1390.4	1365.8	1371.3
733.3	739.5	745.0	1393.8	1373.2	1369.6
735.3	740.7	745.4	1397.1	1378.6	1380.3
733.3	740.1	734.5	1399.6	1380.6	1375.2
730.8	738.7	739.5	1406.0	1383.1	1380.3
731.8	735.5	736.4	1405.8	1383.5	1378.0
725.5	–	–	1408.7	–	–
–	–	–	1408.5	–	–
728.8 (± 9.6)	734.5 (± 5.4)	733.2 (± 9.1)	1393.7 (± 11.5)	1370.4 (± 9.5)	1371.2 (± 6.5)
732.1 (± 8.4) µm			1379.3 (± 14.5) µm		

4.1.2 DMSO-PAN Solution Viscosity Evaluation

The viscosity versus temperature data for the DMSO-PAN solution is provided in Table 4-2. A common method for plotting these values is an Arrhenius function of the form shown in Equation (4-1) where *A* and *B* are fitted coefficients, viscosity (η or μ) is in the form of mPa·s, and temperature is in Kelvin (Hrma and Kruger 2016). The raw and fitted data are provided in Figure 4-2. These data show a nice viscosity-temperature relationship with a high correlation coefficient where *A* = -2.429 and *B* = 2256.

$$\ln(\eta,\mu) = A + B/T \quad (4\text{-}1)$$

Table 4-2. Summary of viscosity measurements (*n*) on DMSO-PAN solution at different measurement temperatures (T_V). For all samples, the Newtonian fit range was 0-1000 s^{-1} (up/down).

T_V (°C)	μ (mPa·s)
25	170.9
40	118.2
50	94.48
60	76.74
70	63.44

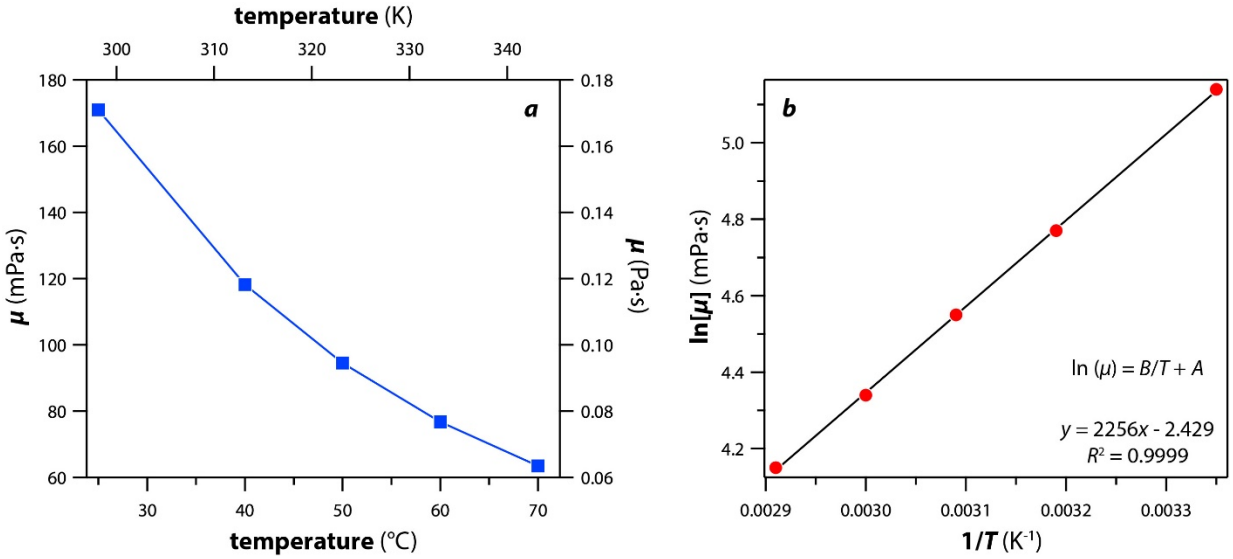

Figure 4-2. Summary of (a) DMSO-PAN viscosity as a function of temperature and (b) the Arrhenius plot of ln(μ) as a function of inverse temperature (K^{-1}).

4.2 Making PAN Composites

Pictures of the as-made PAN composites from Table 3-1 are provided below in Figure 4-3. The appearances of the composite beads were as follows: of 75Ag-PAN(b) was whitish gray, 75Bi-PAN was a bluish gray, 80BiS-PAN 80Cu-PAN were dark gray, 80Cu-PAN was purplish brown (like blueberries), and 90Cu-PAN was reddish brown. Bead sizes varied somewhat as well based solely on visual appearances.

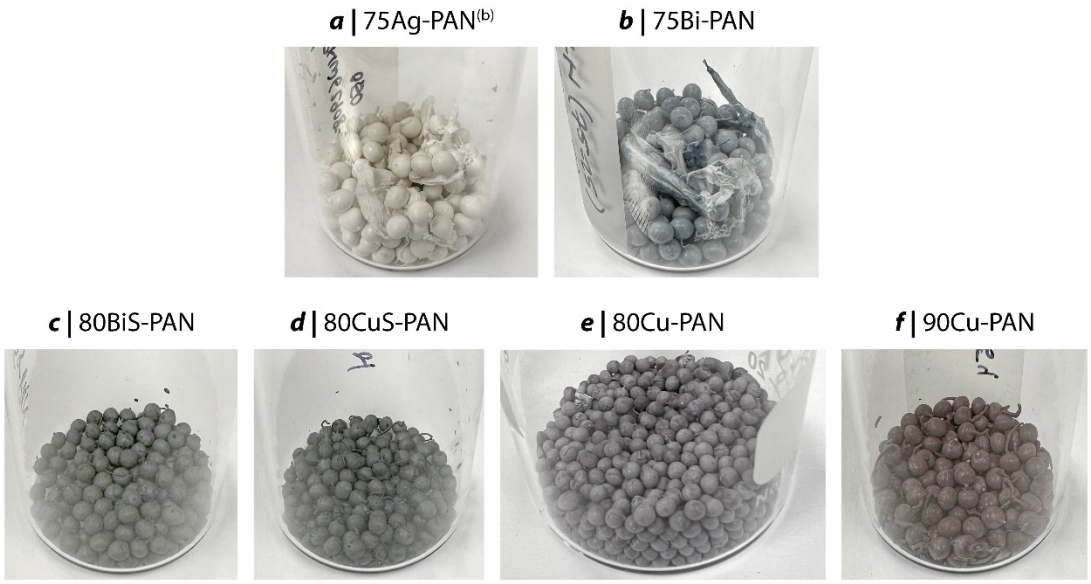

Figure 4-3. Pictures of PAN composite beads including (a) 75Ag-PAN(b), (b) 75Bi-PAN, (c) 80BiS-PAN, (d) 80CuS-PAN, (e) 80Cu-PAN, and (f) 90Cu-PAN after drying. All samples are in 20-mL scintillation vials except for (e), which is in a 100 mL beaker (48 mm diameter) due to the larger sample volume produced for this sample.

The process of making PAN composites results in bead-like shapes but the beads often have tails that are likely the last portion of the drop to enter the water bath, which creates a splash back up towards the pipette dropping the solution mixture, but the tail solidifies instantly and thus remains attached to the bead. These tails can be observed in Figure 4-4 for 80Cu-PAN and 90Cu-PAN. During the DIW rinsing process, the DMSO can be observed emanating from the beads as a layer just above the beads that appears wavey, but still transparent. This layer remains just above the beads due to the density of DMSO (ρ_{DMSO} = 1.1010 g/cm^3, 25°C) being higher than that of water (ρ_{H2O} = 0.99705 g/cm^3, 25°C) (Lide 2008). This is likely due to the difference in the refractive index of DMSO at room temperature (n_D = 1.4793, 20°C) compared to that of water (n_D = 1.33336, 20°C) (Lide 2008).[a] Thus, the extent of DMSO removal from the beads can be monitored during DIW rinsings by monitoring the visual appearance of the solutions after each iteration of replacement (with fresh DIW) and over time. The tails on the beads can be removed from the body of the beads by rolling the beads in a paper towel following drying or while they are freshly made and damp from the DIW rinsing solution.

[a] Refractive index (n_D) values are based off the sodium D line at 589 nm.

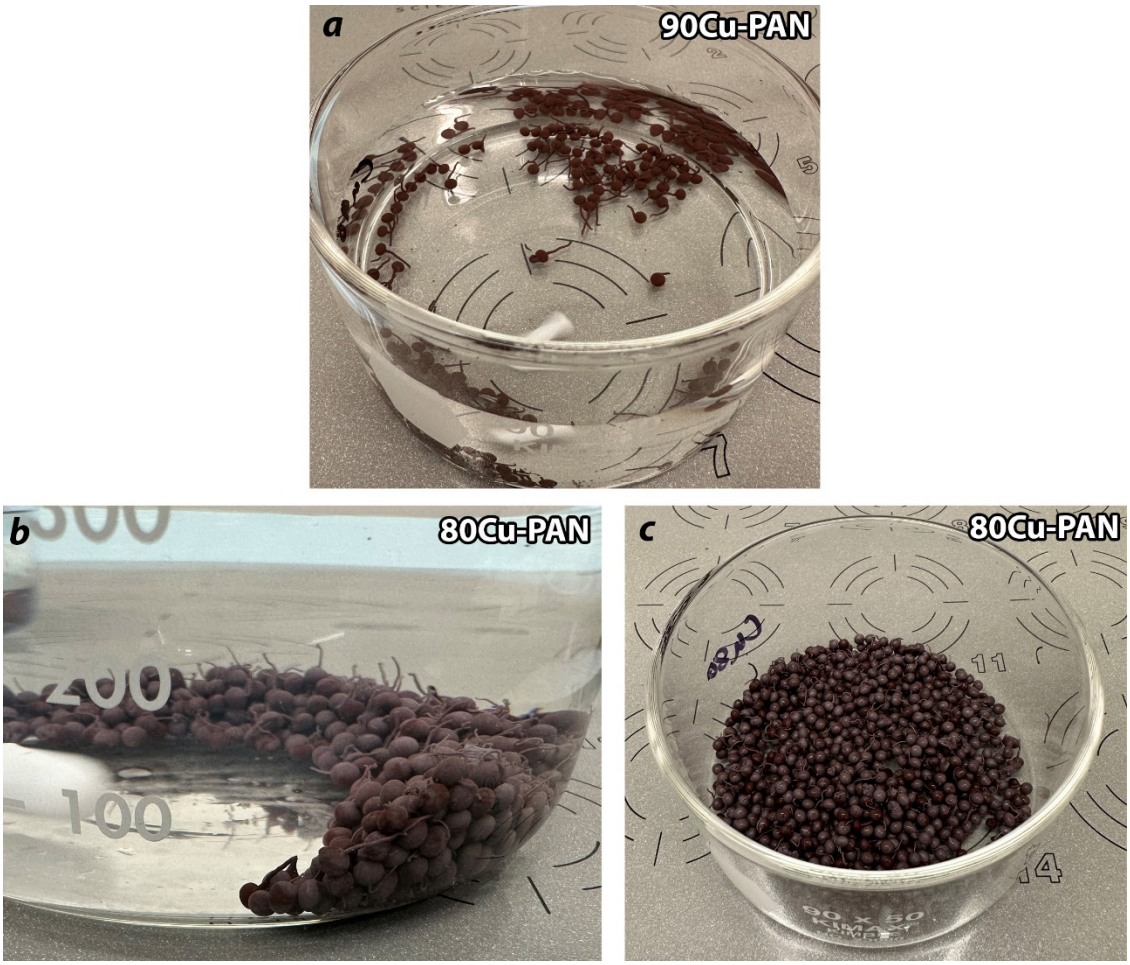

Figure 4-4. Pictures of (a) 90Cu-PAN and (b,c) 80Cu-PAN (b) during the DIW washing process and (c) after the last DIW water rinse was decanted and a picture was taken just before the beads were loaded into a Nalgene bottle. The stir bars were moving when images (a) and (b) were taken so they appear blurry in each. The light blue cloudiness in (b) shows the appearance of DMSO-rich DMSO/DIW solutions.

Pictures of the 80AgS-PAN, 90Ag_2S-PAN, 80Bi_2S_3-PAN, and 80Cu_2S-PAN are presented in Figure 4-5. These pictures emphasize the similar morphologies between the beads but drastic differences in color.

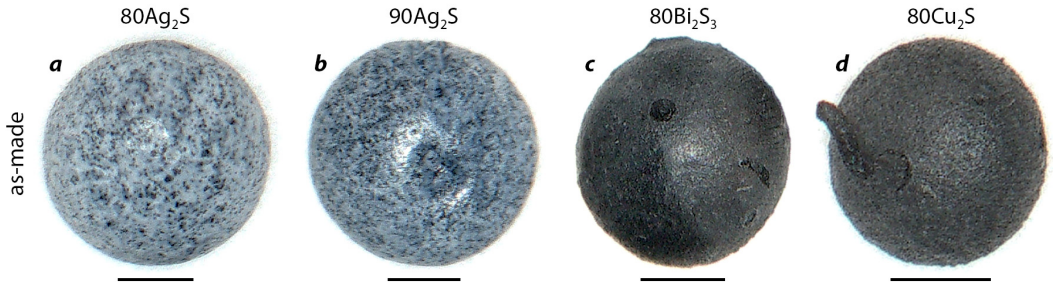

Figure 4-5. Pictures of four as-made MS_x-PAN composites including (a) 80AgS-PAN, (b) 90AgS-PAN, (c) 80BiS-PAN, and (d) 80CuS-PAN. The lines below each image are 1 mm. This figure was modified from the original by Riley et al. (2024).

A potential improvement to the DMSO removal process could be implemented where a basket could be inserted into the dish to catch the beads within the dish. Two examples are shown in Figure 4-6 where the beads are elevated over the bottom of the dish. A few key points of note in the design would be adequate room above the bottom of the dish so a stir bar could spin without hitting the support, a mesh size of small enough opening sizes to make sure that the beads do not fall though the support, and walls on the mesh support to prevent beads spillage over the ledge of the support. An additional feature that it could include would be a handle to allow for each removal of the basket from the dish so it could be placed directly (and quickly) into a new dish with fresh DIW. Finally, if the basket had a feedthrough port near the edge, a pipette could be inserted through the basket plane and used to draw DMSO-rich solution out of the container to further facilitate DMSO removal from the vicinity of the pellets and expedite the solution rinsing process to dilute DMSO within the pellet interior surfaces and replace it with fresh DIW.

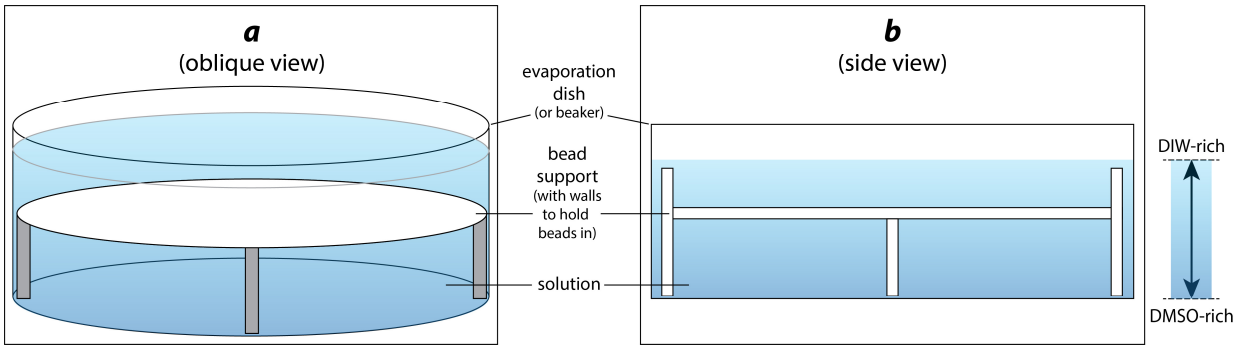

Figure 4-6. (a) Oblique-view and (b) side-view drawing of how the PAN composite bead formation process could be improved by allowing for a gap under a support holding the beads that can be stirred without disturbing the beads where the DMSO-rich solution could be removed from below the beads. In both designs, the basket would be a mesh likely made of stainless steel.

4.3 Iodine Loading of Samples

The details of the iodine loading of each sample loaded under this project or from previous projects are provided in Table 4-3. Iodine loading runs were performed with different sets of samples, experiments were run at different temperatures, and details were summarized accordingly so that the original samples used could be tracked both before and after iodine loading processes. Sample naming designations were given based the source material and the loading temperature but also with secondary labels (i.e., “ID” in Table 4-3) to make sure that samples were not mixed up at any time during the project. Pictures of several PAN composite beads (and other samples) are shown in Figure 4-7, Figure 4-8, and Figure 4-9. In all cases, the color of the beads changed after iodine loading.

Table 4-3. Description of samples for iodine loading process including the batch ID, sample description, iodine loading temperature used (T_{Load}), initial sorbent mass ($m_{s,i}$), final sorbent mass after iodine ($m_{s,f}$), mass of iodine loaded on each sample (m_I), iodine loading in g iodine per gram of sorbent (Q_e), the mass of PAN in the loaded sorbent ($m_{PAN,L}$), the mass of residual metal in the loaded sorbent ($m_{m,L}$), the mass of metal-iodide (MI_x) in the loaded sorbent ($m_{MIx,L}$) [the mass of total iodine in the loaded sorbent ($m_{I,L}$) is equal to m_I], the mass of residual sulfur ($m_{sulf,L}$) in the loaded sorbent, the volume of MI_x per mass of loaded PAN composite (V_{MIx}/m_{LS}), and the total volume of iodine-loaded PAN composite per mass (V_{tot}/m_{LS}). For the sample name, the superscripted value is the temperature at which iodine was loaded. Ag-400 is from IONEX. For more details, see Table 3-2.

ID	Description (base sorbent)	Sample Name (after iodine)	T_{Load} (°C)	$m_{s,i}$ (g)	$m_{s,f}$ (g)	m_I (g)	Q_e (g/g)	$m_{PAN,L}$ (g)	$m_{m,L}$ (g)	$m_{MIx,L}$ (g)	$m_{Sulf,L}$ (g)	V_{MIx}/m_{LS} (cm^3/g)	V_{tot}/m_{LS} (cm^3/g)
I-1a	75Ag-PAN	75Ag-PAN$^{(120)}$	120	0.0369	0.0647	0.0278	0.7534	0.0092	0.0040	0.0514	–	0.1399	0.2663
I-1b	75Cu-PAN	75Cu-PAN$^{(120)}$	120	0.0276	0.0678	0.0402	1.4565	0.0069	0.0006	0.0603	–	0.1569	0.2438
I-2a	Ag-400	Ag400$^{(150)}$	150	0.2301	0.3008	0.0707	0.3073	–	–	–	–	–	–
I-2b	75Ag-PAN	75Ag-PAN$^{(150)}$	150	0.1388	0.2543	0.1155	0.8321	0.0347	0.0059	0.2137	–	0.1479	0.2654
I-2c	75Cu-PAN	75Cu-PAN$^{(150)}$	150	0.1174	0.2852	0.1678	1.4293	0.0294	0.0040	0.2518	–	0.1557	0.2393
I-3a	75Ag-PAN	75Ag-PAN$^{(130)}$	130	0.7213	1.3320	0.6149	0.8525	0.1803	0.0183	1.1376	–	0.1504	0.2660
I-3b	75Bi-PAN	75Bi-PAN$^{(130)}$	130	0.7290	1.2952	0.5704	0.7824	(a)	(a)	(a)	–	(a)	(a)
I-3c	AC-6120	AC6120$^{(130)}$	130	0.1001	0.1079	0.0120	0.1199	–	–	–	–	–	–
I-3d	Ag-400	Ag400$^{(130)a}$	130	0.0979	0.1327	0.0390	0.3984	–	–	–	–	–	–
I-4a	80BiS-PAN	BiS-PAN$^{(130)}$	130	0.1516	0.2894	0.1378	0.9090	(a)	(a)	(a)	(a)	(a)	(a)
I-4b	80CuS-PAN	CuS-PAN$^{(130)}$	130	0.1546	0.3239	0.1693	1.0951	0.0309	0.0140	0.2541	0.0249	0.1383	0.2610
I-4c	80Cu-PAN	80Cu-PAN$^{(130)}$	130	0.1530	0.3816	0.2286	1.4941	0.0306	0.0079	0.3431	–	0.1586	0.2286
I-4d	90Cu-PAN	90Cu-PAN$^{(130)}$	130	0.1540	0.4210	0.2670	1.7338	0.0154	0.0049	0.4007	–	0.1679	0.2001
I-4e	Ag-400	Ag400$^{(130)b}$	130	0.1256	0.1823	0.0567	0.4514	–	–	–	–	–	–
I-5a	80AgS-PAN	80AgS-PAN$^{(130)}$	130	0.1194	0.2057	0.0863	0.7228	0.0239	0.0098	0.1597	0.0124	0.1366	0.2683
I-5b	90AgS-PAN	90AgS-PAN$^{(130)}$	130	0.1585	0.2895	0.1310	0.8265	0.0159	0.0128	0.2423	0.0185	0.1474	0.2287
I-5c	Ag-400	Ag-400$^{(130)c}$	130	0.1305	0.1933	0.0628	0.4812	–	–	–	–	–	–

(a)Values could not be determined based on the incongruent formation of MI_x (i.e., BiI_3 and BiOI) in the iodine-loaded samples because (1) the entire sample would have to be analyzed with XRD and mass changes are complicated by the formation of BiOI, which introduces oxygen and adding mass.

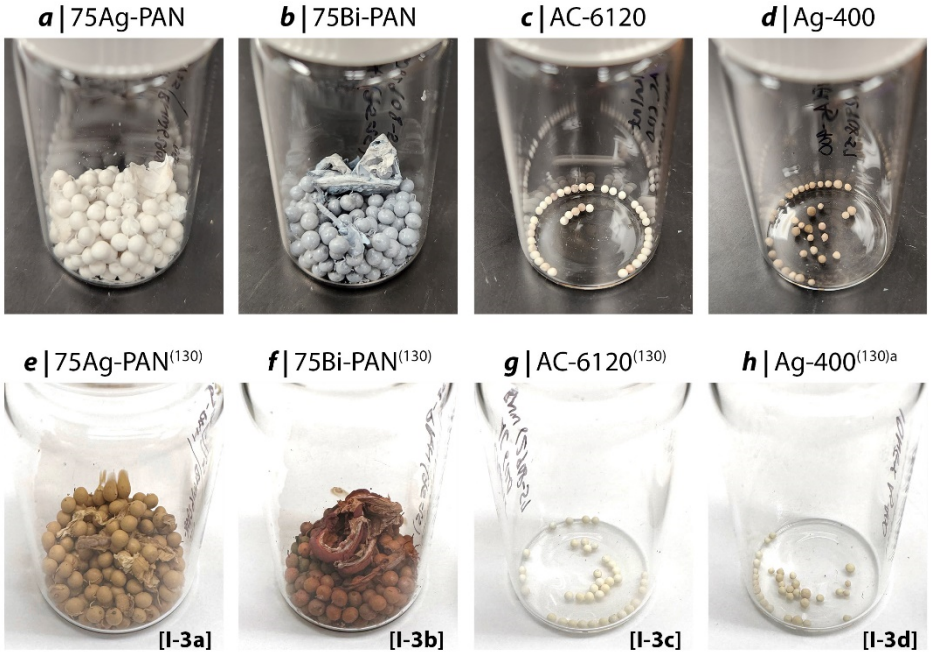

Figure 4-7. Pictures of iodine loading set-3 (a-d) before and (e-h) after iodine loading including (a,e) 75Ag-PAN$^{(130)}$, (b,f) 75Bi-PAN$^{(130)}$, (c,g) AC-6120$^{(130)}$, and (d,h) Ag-400$^{(130)a}$. Details for iodine loading and sample designations shown in the figure are provided in Table 4-3.

Figure 4-8. Pictures of iodine loading set-4 (a-d) before and (e-i) after iodine loading including (a) 80BiS-PAN, (b) 80CuS-PAN, (c) 80Cu-PAN, (d) 90Cu-PAN, (e) 80BiS-PAN$^{(130)}$, (f) 80CuS-PAN$^{(130)}$, (g) 80Cu-PAN$^{(130)}$, (h) 90Cu-PAN$^{(130)}$, and (i) Ag-400$^{(130)b}$. Details for iodine loading and sample designations shown in the figure are provided in Table 4-3.

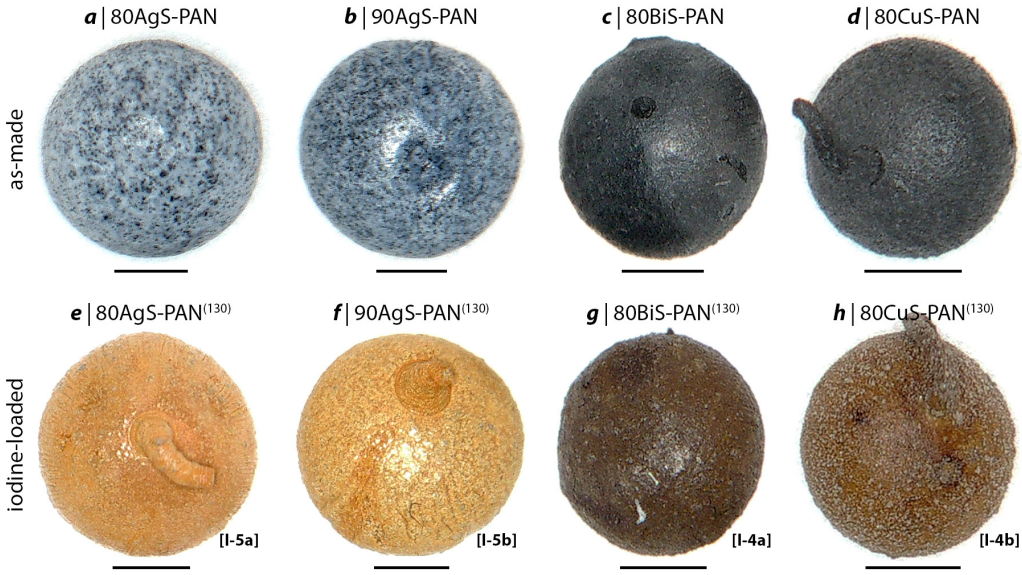

Figure 4-9. Pictures of MS_x-PAN composites (a-d) before iodine loading and (f-i) after iodine loading including (a) 80AgS-PAN, (b) 90AgS-PAN, (c) 80BiS-PAN, (d) 80CuS-PAN, (e) 80AgS-PAN$^{(130)}$, (f) 90AgS-PAN$^{(130)}$, (g) 80BiS-PAN$^{(130)}$, and (h) 80CuS-PAN$^{(130)}$. The lines below each image are 1 mm. This graphic was modified from the original (Riley et al. 2024).

4.4 Evaluating PAN Removal after Iodine Loading

Experiments were conducted to evaluate PAN phase removal after iodine loading of the PAN composites (see Section 3.5.3). Pictures of small-scale experiments to assess feasibility of this process are summarized in Figure 4-10 for 75Ag-PAN$^{(130)}$, 75Bi-PAN$^{(130)}$, and 75Cu-PAN$^{(150)}$. The initial test was conducted with 75Cu-PAN$^{(150)}$ using intact beads but the dissolution rate was so slow that crushed beads were used for the next set of samples which were 75Ag-PAN$^{(130)}$ and 75Bi-PAN$^{(130)}$ to see if this changed the dissolution rate. For the 75Cu-PAN$^{(150)}$ test, a timelapse of solution appearance is provided in Figure 4-11; the initial color was light yellow and it gradually turned darker and dark until it was completely opaque after 1165 min. For 75Ag-PAN$^{(130)}$ and 75Bi-PAN$^{(130)}$, the dissolution behaviors were very different from one another. The 75Ag-PAN$^{(130)}$ sample appeared to dissolve the PAN fairly rapidly and a fine particulate product was left on the bottom. The solution turned a light yellowish orange color. For 75Bi-PAN$^{(130)}$, the solution immediately started to turn red and no evidence of residual particulates was observed after approximately 5-10 min; this time was difficult to determine due to the opacity of the solution. The last set of experiments conducted are shown in Figure 4-12 and included 80BiS-PAN$^{(130)}$, 80CuS-PAN$^{(130)}$, 80Cu-PAN$^{(130)}$, and 90Cu-PAN$^{(130)}$.

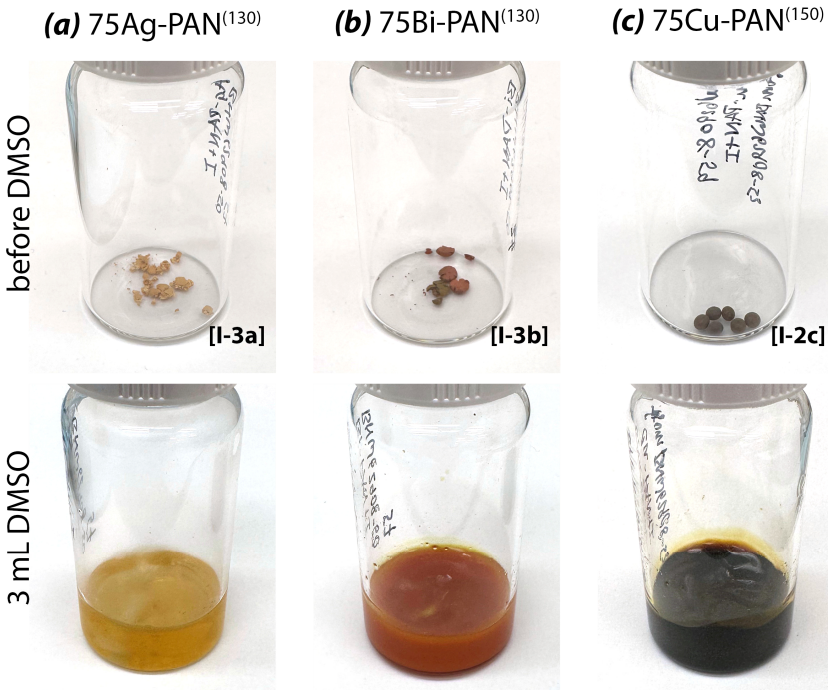

Figure 4-10. Pictures of (a) 75Ag-PAN$^{(130)}$ [I-3a], (b) 75Bi-PAN$^{(130)}$ [I-3b], and (c) 75Cu-PAN$^{(150)}$ [I-2c] (top) pellets and (bottom) in 3 mL DMSO. The time elapsed since DMSO was added are ~20 min for (a) and (b) and 5 days for (c).

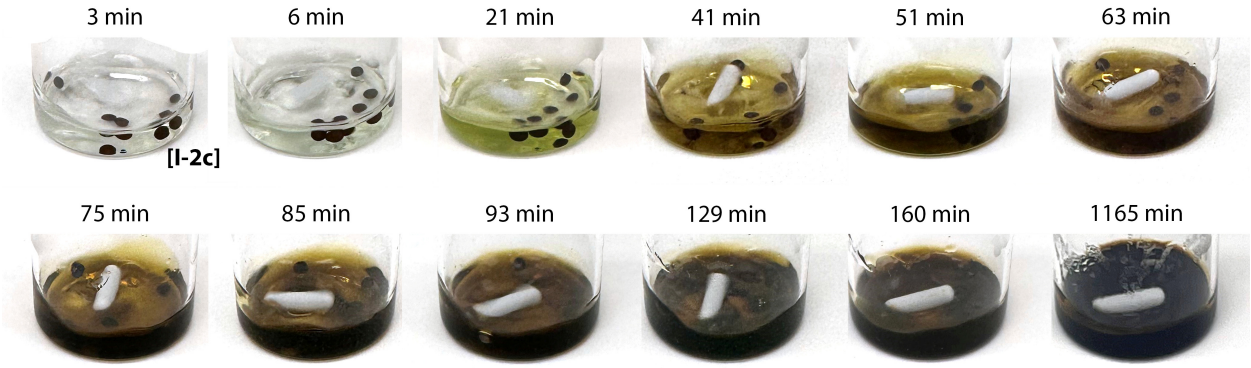

Figure 4-11. Timelapse pictures for 75Cu-PAN$^{(150)}$ [I-2c] dissolution in DMSO over 1165 min.

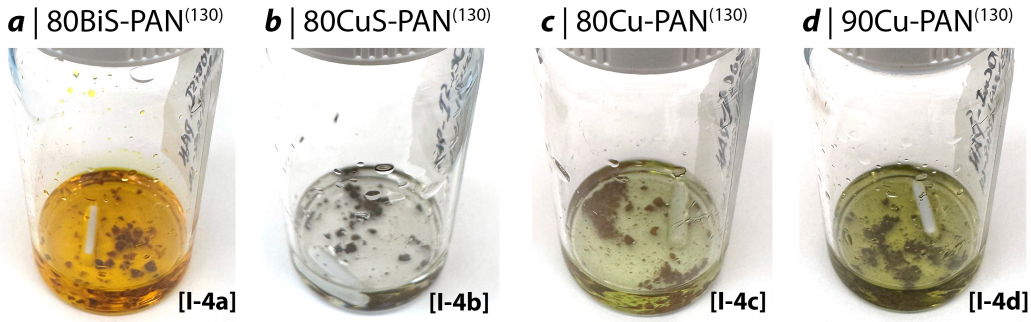

Figure 4-12. Pictures of (a) 80BiS-PAN$^{(130)}$ [I-4a], (b) 80CuS-PAN$^{(130)}$ [I-4b], (c) 80Cu-PAN$^{(130)}$ [I-4c], and (d) 90Cu-PAN$^{(130)}$ [I-4d] after sitting in DMSO for ≈ 1 minute.

The 75Ag-PAN$^{(130)}$ and 75Bi-PAN$^{(130)}$ samples showed the most promise based on the solids volume reduction and visible solid size reduction. The rest of the materials [i.e., 75Cu-PAN$^{(150)}$, 80BiS-PAN$^{(130)}$, 80CuS-PAN$^{(130)}$, 80Cu-PAN$^{(130)}$, and 90Cu-PAN$^{(130)}$] showed visible solids left and incomplete polymer dissolution. For all of the Cu-based sorbents [i.e., 75Cu-PAN$^{(150)}$, 80CuS-PAN$^{(130)}$, 80Cu-PAN$^{(130)}$, and 90Cu-PAN$^{(130)}$], the solutions turned very dark black (all similar in color to the 1165-min mark in Figure 4-11). The process of recovering the solid insoluble particulates from samples 75Ag-PAN$^{(130)}$ and 75Bi-PAN$^{(130)}$ (discussed in Section 3.6) was most promising for 75Ag-PAN$^{(130)}$ where particles settled nicely and the DIW above the particles was very clear whereas the DIW for 75Bi-PAN$^{(130)}$ was notably orange suggesting either some dissolution or fine particles that remained suspended after the centrifugation process (Figure 4-13).

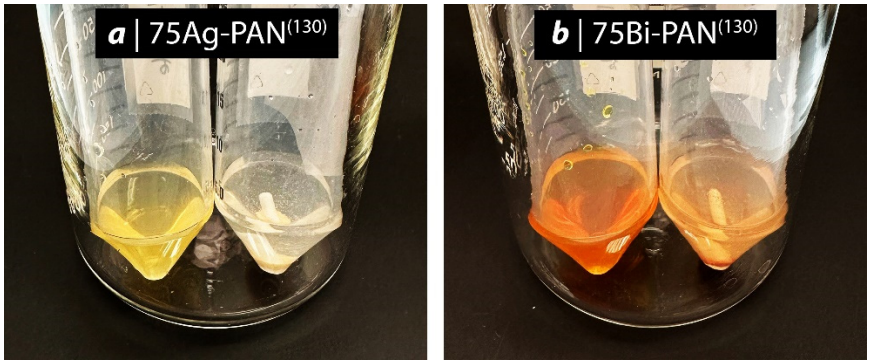

Figure 4-13. Pictures showing the DMSO dissolution phase in 50-mL centrifuge tubes for (a) 75Ag-PAN$^{(130)}$ and (b) 75Bi-PAN$^{(130)}$ samples. For each set, the tube on the left is the initial DMSO solution pipetted off the residual particles at the bottom and the tube on the right is the recovered particle pellet with fresh DIW added. The white stir bars can be seen in the tubes.

After pelletization of the recovered products at the bottom of the tubes shown on the right side of each image in Figure 4-13, the tubes were centrifuged at 2500 RPM for 5 min (Thermo Sorval Legend Mach 1.6). The DIW above the pellets was carefully removed with a 1-mL pipette and discarded. The remaining products were dried in a vacuum desiccator over the course of a few days at room temperature. Following drying, the products were analyzed with XRD and found to be phase-pure AgI (i.e., a mixture of hexagonal β-AgI called *iodargyrite* and cubic γ-AgI called *miersite*) and phase-pure BiOI for 75Ag-PAN$^{(130)}$ [i.e., experiment I-3a in Table 3-6] and 75Bi-PAN$^{(130)}$ [i.e., experiment I-3b in Table 3-6], respectively, as shown in Figure 4-14. This mixture of hexagonal β-AgI and cubic γ-AgI being present in iodine-loaded silver compounds has been documented many times in the past with some examples being provided by Riley et al. (Riley et al. 2017; Riley et al. 2021b; Riley et al. 2022a; Riley et al. 2022b) and Chong et al. (Chong et al. 2021; Chong et al. 2022). The MI_x yields from these experiments (mass% recovered, i.e., *R*%) were estimated at 77 mass% for AgI [sample 75Ag-PAN$^{(130)}$] and 35 mass% BiOI [sample 75Bi-PAN$^{(130)}$]. These estimates assume all captured iodine (from Table 4-3) converted to the target MI_x compound. The values are also a bit lower than the actual values due to difficultly weighing the small, recovered particle masses due to static. Additional mass losses could be due to MI_x dissolution in the DMSO. Details for these calculations are provided in Table 4-4.

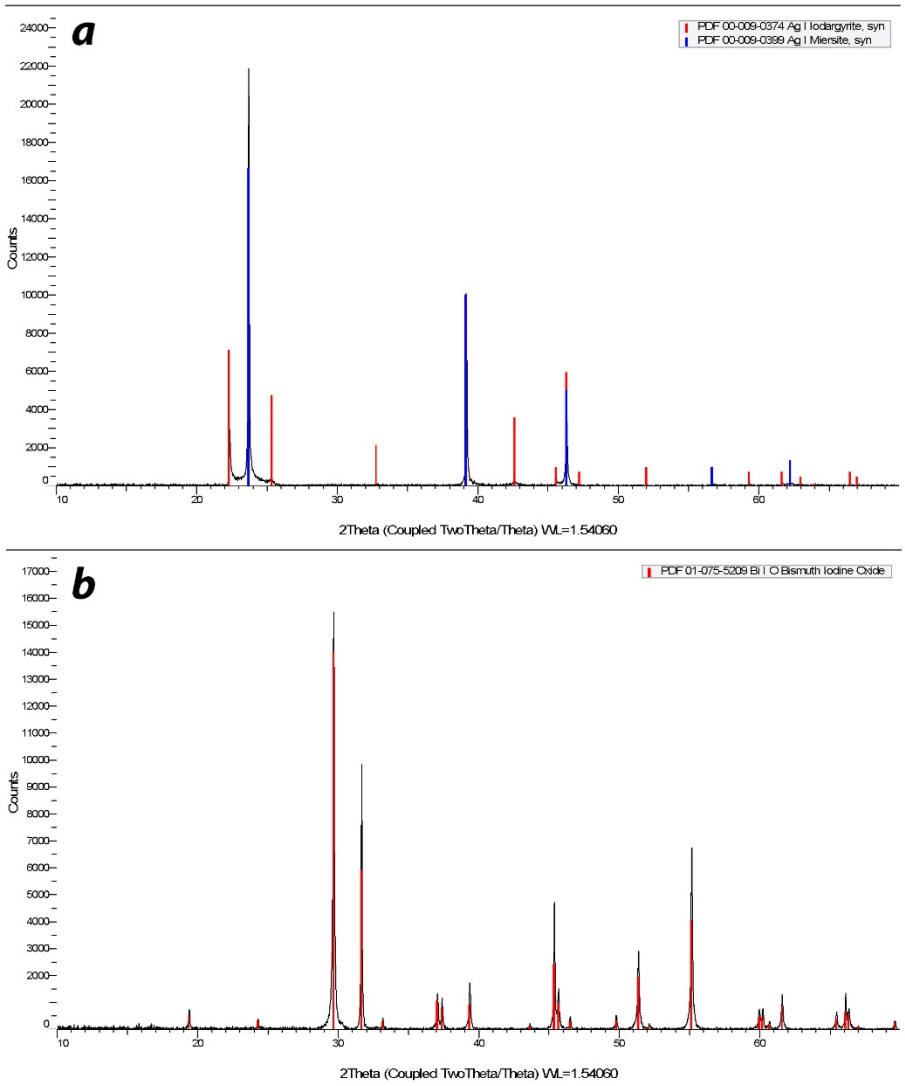

Figure 4-14. XRD data for recovered products from 75Ag-PAN(130) [i.e., experiment I-3a in Table 3-6] and 75Bi-PAN(130) [i.e., experiment I-3b in Table 3-6] after DMSO-PAN dissolution, product washing, and product drying (see Section 3.6).

Table 4-4. Summary of MI_x recoveries (R%) after DMSO dissolution tests described above including mass of sample used (m_s), estimated MIx present in the sample, and mass of recovered MI_x (assuming all mas is MI_x).

ID	Sample	m_s	MI_x	m_{recov}	R%
I-3a	75Ag-PAN(130	0.0317	0.0280	0.0217	77.4%
I-3b	75Bi-PAN(130)	0.0288	0.0205	0.0071	34.7%

4.5 Properties of Encapsulant Metals

The PSD data for the encapsulant metals are provided in Appendix A.3 (see Figure A-16, Figure A-17, Figure A-18 for Bi^0, Sn^0, and $BiSn^0$ eutectic, respectively). The melting points for the metals

($T_{m,m}$) for each encapsulant metal measured using the DSC and the ρ_b values are all summarized in Table 4-5. The $T_{m,m}$ values were determined as the onset off the endothermic peak for each dataset. A summary of the DSC data for all four encapsulant metals are shown in Figure 4-15. Based on the DSC data for the Bi-Pb alloy, it was clear that the eutectic compound did not form upon melting and showed distinctly different $T_{m,m}$ for each of the constituent metals, i.e., onset-1 (Bi at 269.2°C) and onset-2 (Pb at 323.5°C). Due to this issue for the Bi-Pb alloy, we decided not to move forward with this and send it back to the vendor for a credit.

Table 4-5. Summary of measured melting temperatures from DSC ($T_{m,m}$), average (AVE) measured bulk densities (ρ_b) and standard deviations (SD) from helium pycnometry.

Metal	$T_{m,m}$ (°C)	Density (ρ_b) data	
		AVE (g/cm^3)	SD (g/cm^3)
Bi	269.5	9.7828	0.0095
Sn	230.2	7.2900	0.0051
Bi-Sn	138.8	8.5588	0.0075

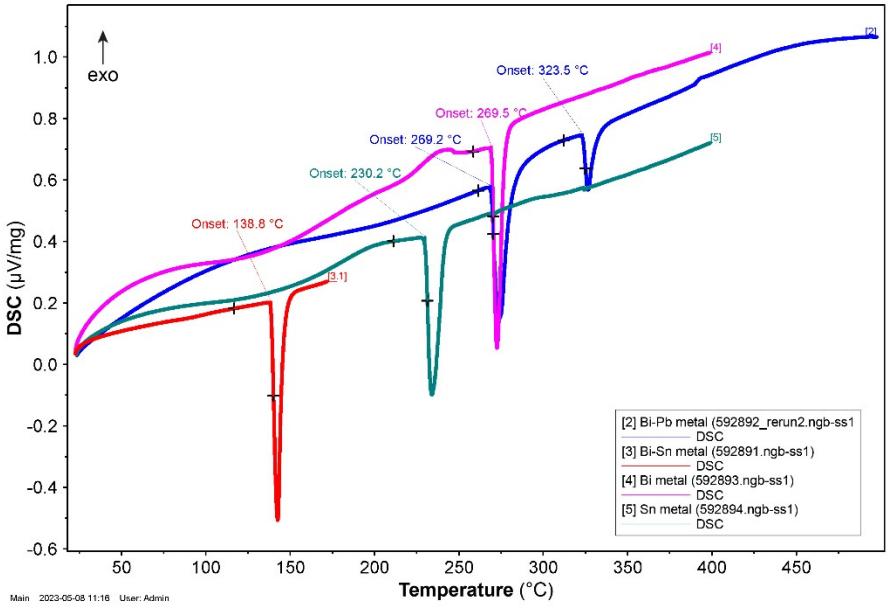

Figure 4-15. Summary of DSC data showing onset of melting.

4.6 Initial One-Phase Pellet (Set-1)

The initial pellet (set-1) was just a pure Bi^0 (100Bi) pressed with an initial target green pellet thickness ($t_{p,g}$) of 1.5 mm. Optical micrographs of the cross-sectioned pellet are provided in Figure 4-16 below and show some color gradations across the pellet with lighter appearance on one side than the other. The SEM micrograph collages shown in Figure 4-17 and Figure 4-18 show some striations in the metal particles as well as some intergranular gaps between the particles. The pellets after this run were heat treated under vacuum to help prevent metal oxidation during the heat treatment process. The cause for the differences in appearance between the top and bottom surfaces of the pellet are unknown but it could be different porosities resulting in epoxy-driven optical differences.

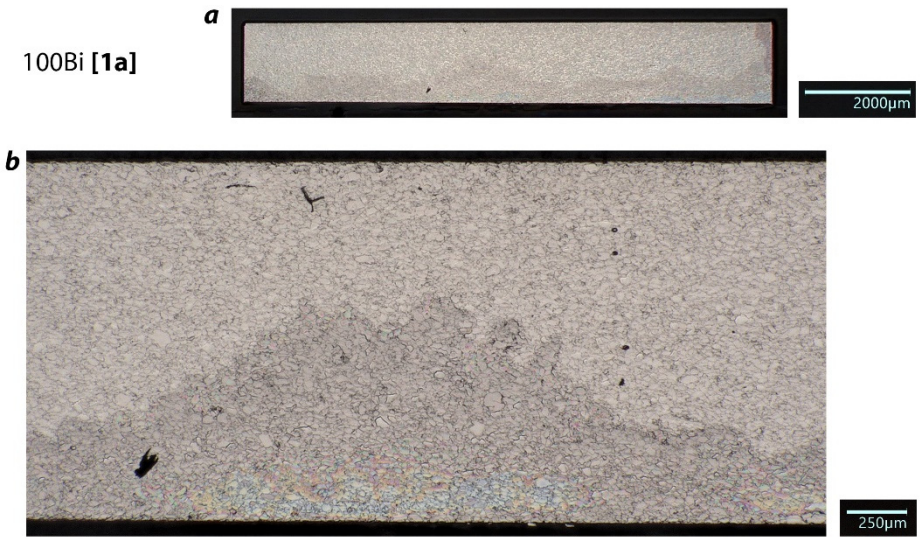

Figure 4-16. Optical micrographs of (Set-1) $100Bi^0$ [1a] pellet fired at 203°C for 22 hours taken at (a) 20× and (b) 100× magnifications.

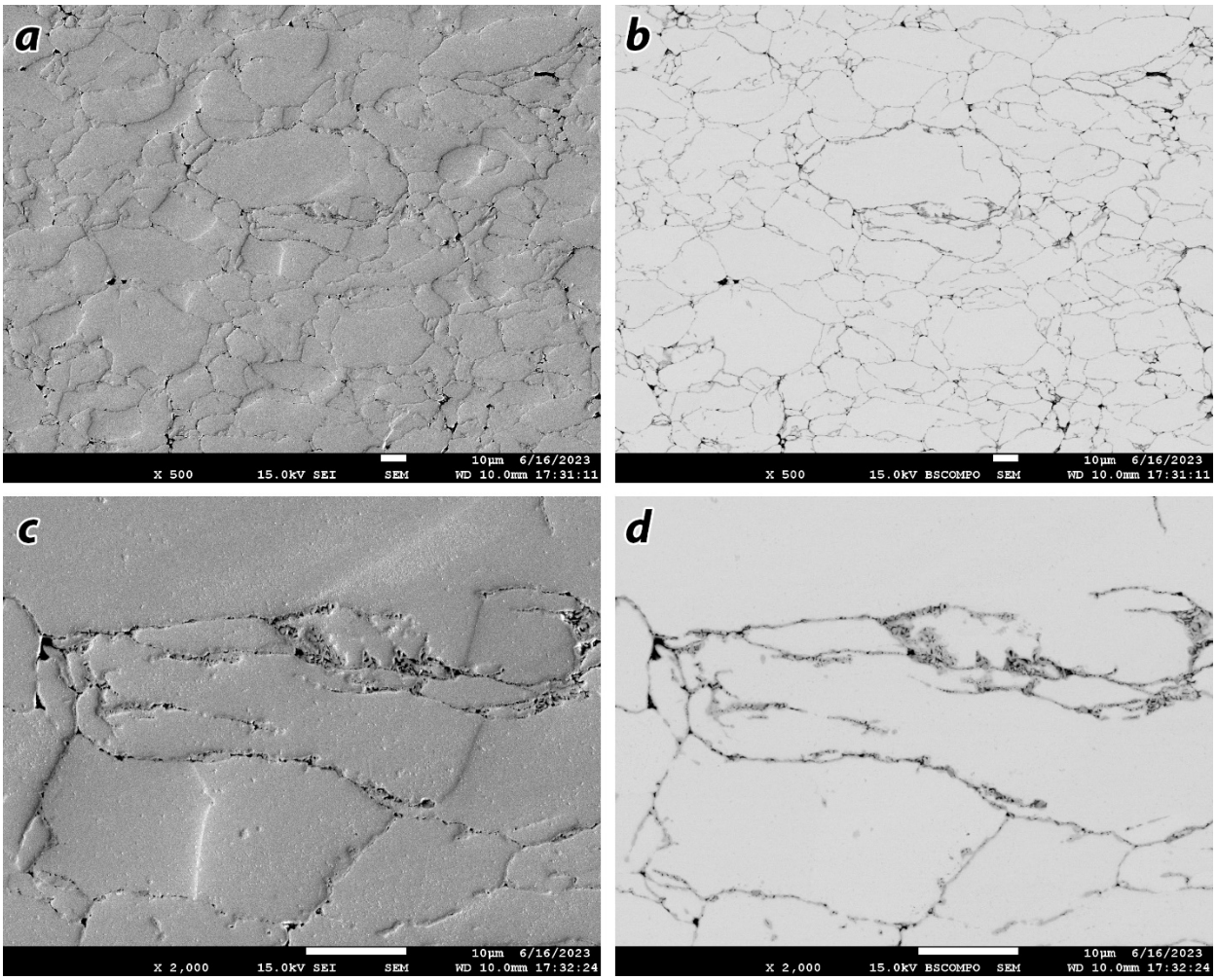

Figure 4-17. SEM including (a,c) SEI and (b,d) BSE micrographs of the left side of the Set-1 pellet.

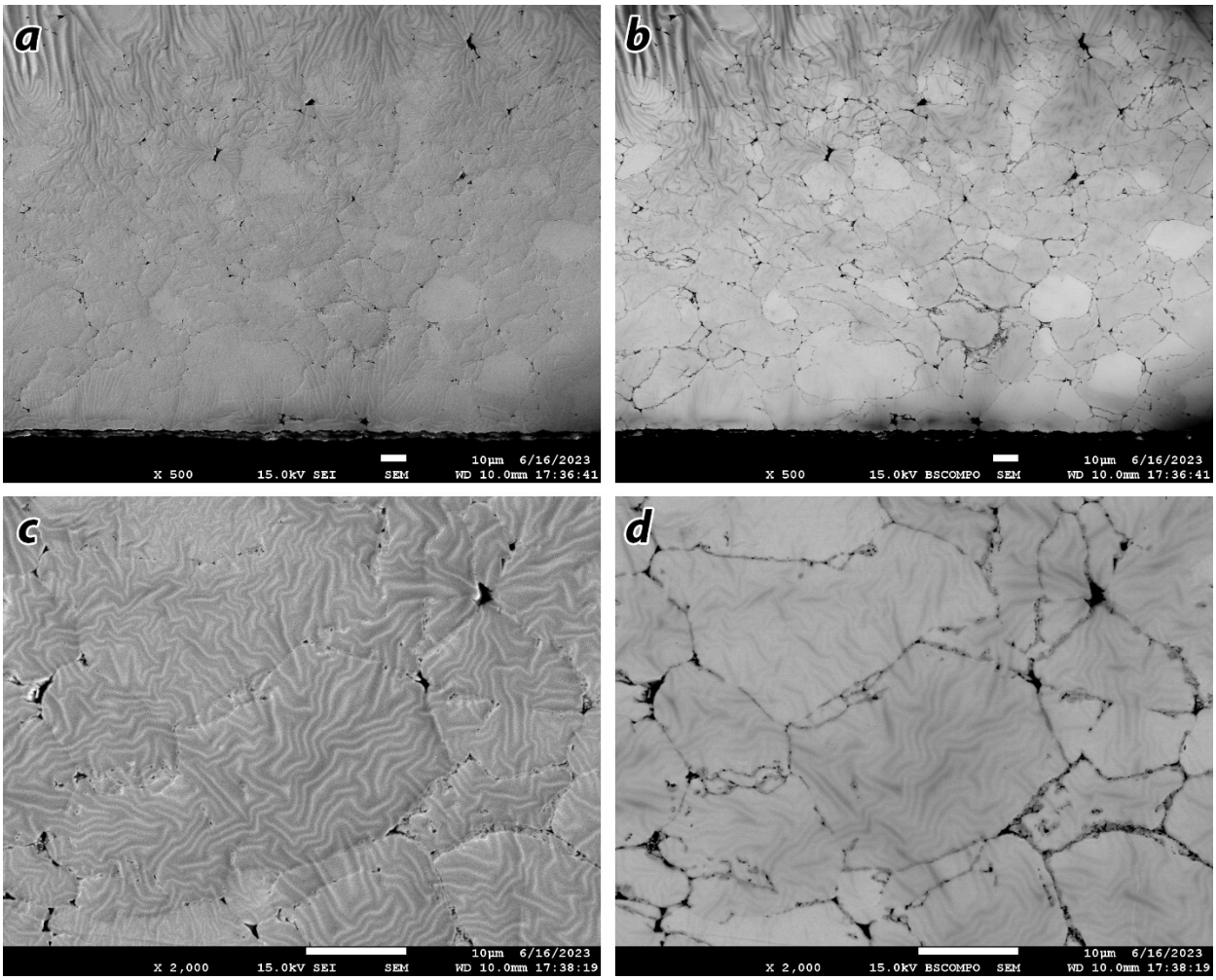

Figure 4-18. SEM including (a,c) SEI and (b,d) BSE micrographs of the right side of the Set-1 pellet.

4.7 Two-Phase Pellets Without Iodine (Set-2)

The details for the two-phase pellets made without iodine using Al_2O_3 as a surrogate ceramic phase are summarized in Table 4-6. The incompressibility of these pellets was very noticeable where the Set-2b pellet and Set-2c pellets were ~152% and ~175% the predicted volumes ($V\%_T$) based solely on density predictions of the individual phases (assuming no mixing) demonstrating a large open porosity. This porosity was confirmed with the optical micrographs shown in Figure 4-19. SEM micrographs for Set-2a are shown in Figure 4-20 and Figure 4-21, for Set-2b are shown in Figure 4-22 and Figure 4-23, and for Set-2c are shown in Figure 4-24 and Figure 4-25. In the Al_2O_3-containing samples (2b and 2c), the dark regions are comprised of the Al_2O_3 phase or void spaces filled with epoxy. It is also expected that the Al_2O_3 particles likely contain porosity that assisted in preventing pelletization without excess void space.

Table 4-6. Summary of Set-2 pellets made with Al_2O_3 surrogate ceramic phase.

Pellet Number:	2a	2b	2c
Alternative ID:	100Bi	90Bi-Al	85Bi-Al
Date:	5/18/2023	5/18/2023	5/18/2023
Phase-a (comp.)	Bi	Bi	Bi
Phase-b (comp.)	–	Al_2O_3	Al_2O_3
Phase-a (mass, g)	1.9294	1.5095	1.3399
Phase-b (mass, g)	–	0.1673	0.2360
$m_{p,g}$ (g)	1.9157	1.6619	1.559
Atmosphere type	Air	Air	Air
T_{ht} (°C)	203	203	203
t_{ht} (h)	8	8	8
Ramp (°C/min)	5	5	5
$t_{p,f}$ (mm)	2.533	3.797	4.389
$m_{p,f}$ (g)	1.9239	1.6712	1.5697
Δm (m%)	0.43%	0.56%	0.69%
ρ_b (g/cm^3)	9.6707	5.6045	4.5540
$\rho_{b,em}$ (g/cm^3)	9.7828	9.7828	9.7828
$V\%_T$ (vol%)	101.6%	151.8%	175.4%

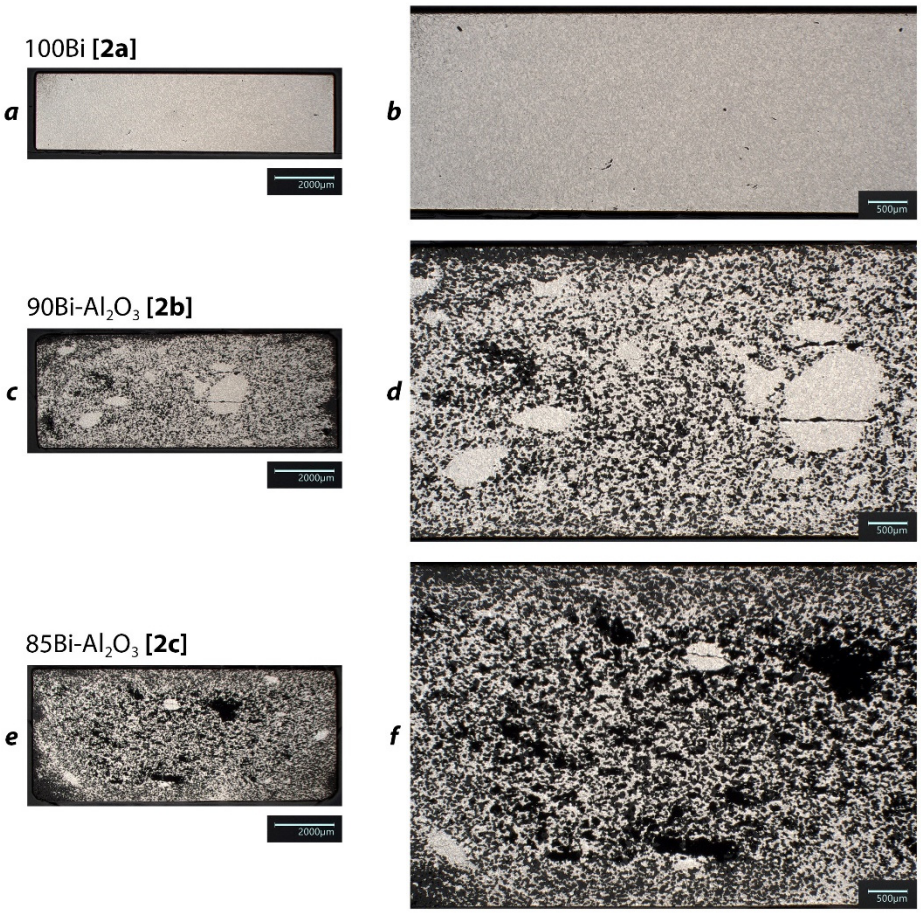

Figure 4-19. Cross-sectional optical micrographs of two-phase set-2 pellets including (a,b) 100Bi(v) [2a], (c,d) 90Bi-Al_2O_3 [2b], and (e,f) 85Bi-Al_2O_3 [2c] taken at (a,c,e) 20× and (b,d,f) 50× magnifications. Darker regions include voids and Al_2O_3. These pellets were fired at 203°C for 8 h in the vacuum oven under vacuum.

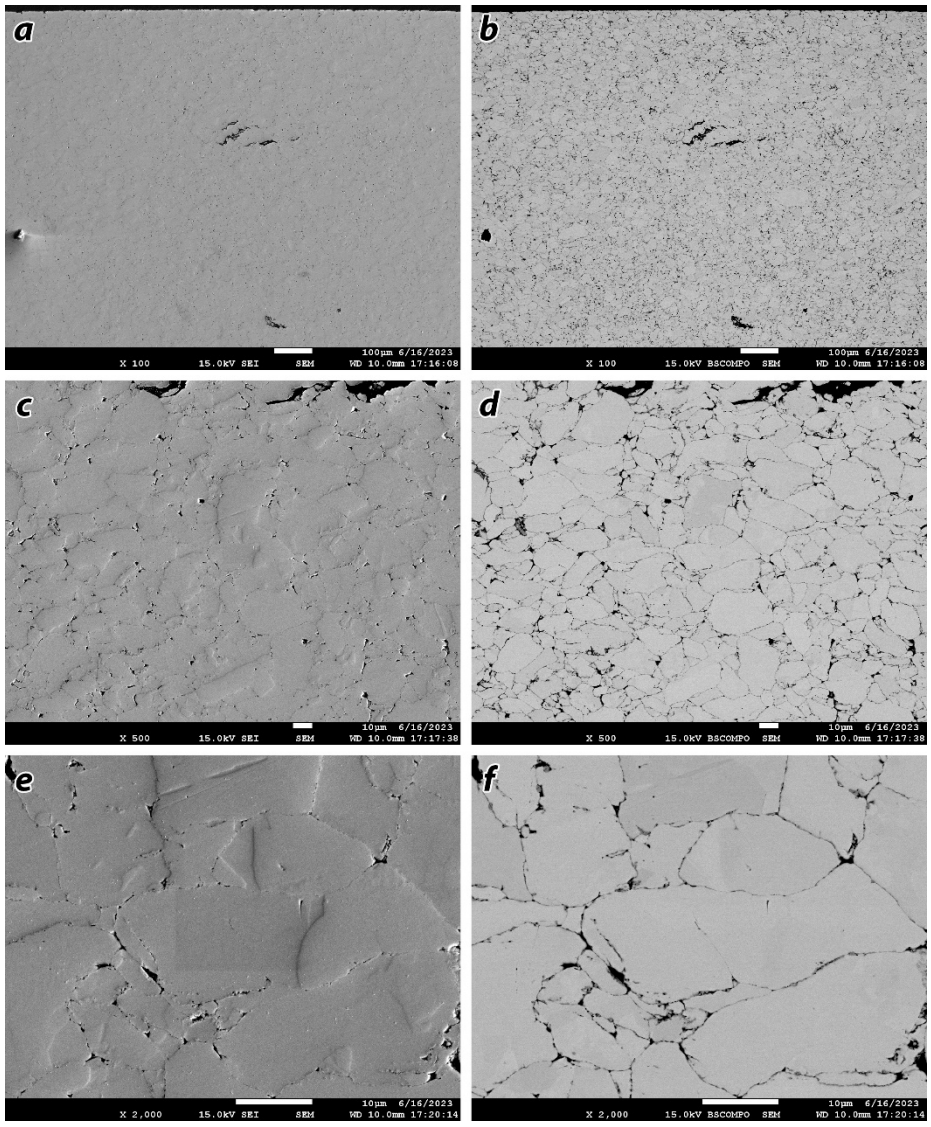

Figure 4-20. SEM including (a,c,e) SEI and (b,d,f) BSE micrographs of side-1 of the Set-2a pellet taken at (a,b) 100×, (c,d) 500×, and (e,f) 2k× magnifications.

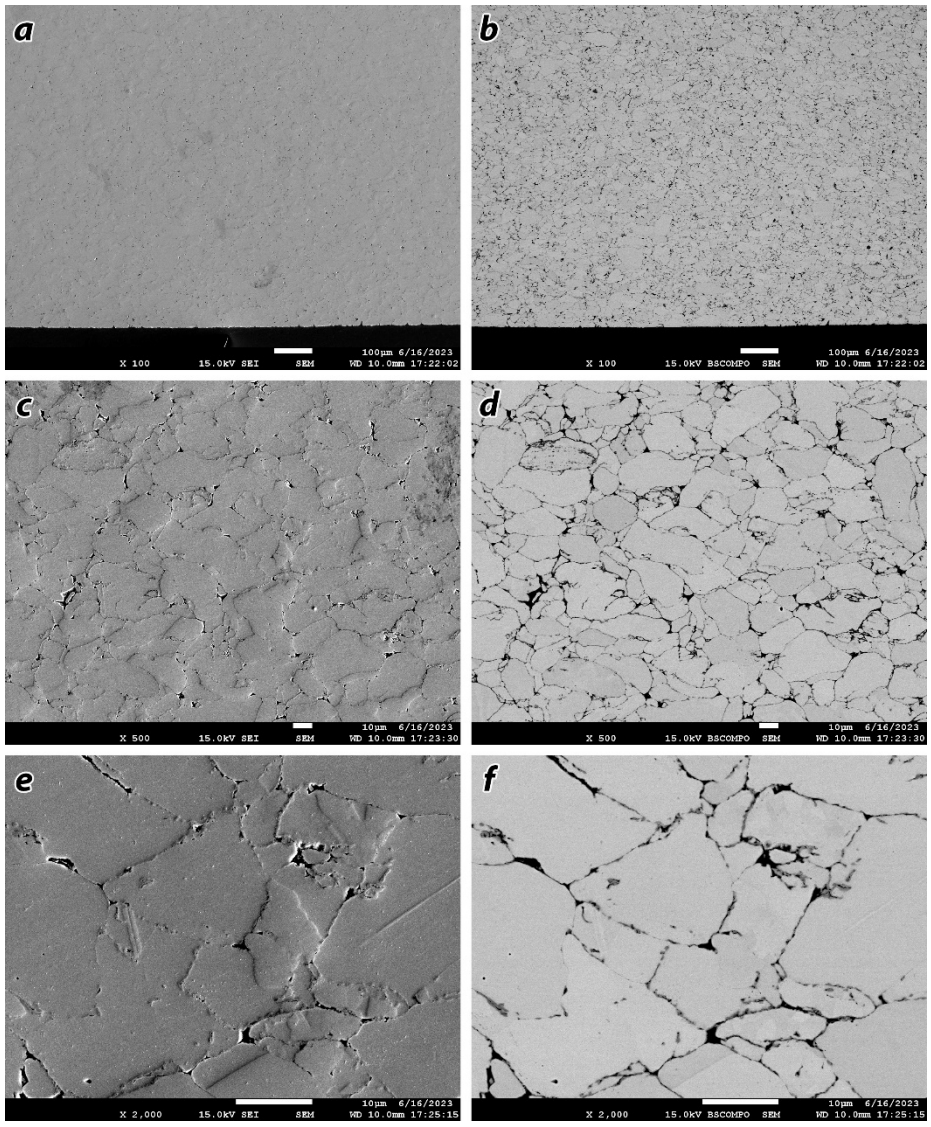

Figure 4-21. SEM including (a,c,e) SEI and (b,d,f) BSE micrographs of side-2 of the Set-2a pellet taken at (a,b) 100×, (c,d) 500×, and (e,f) 2k× magnifications.

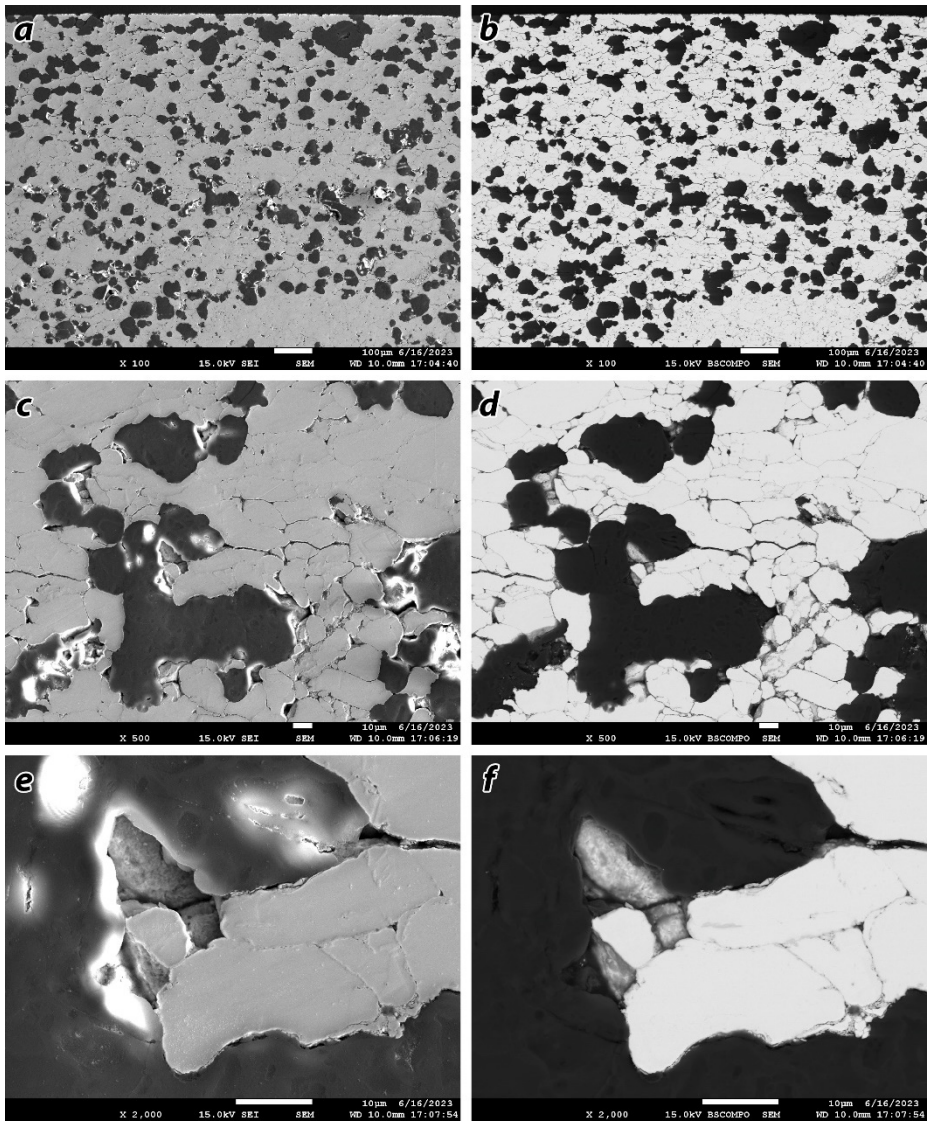

Figure 4-22. SEM including (a,c,e) SEI and (b,d,f) BSE micrographs of side-1 of the Set-2b pellet taken at (a,b) 100×, (c,d) 500×, and (e,f) 2k× magnifications.

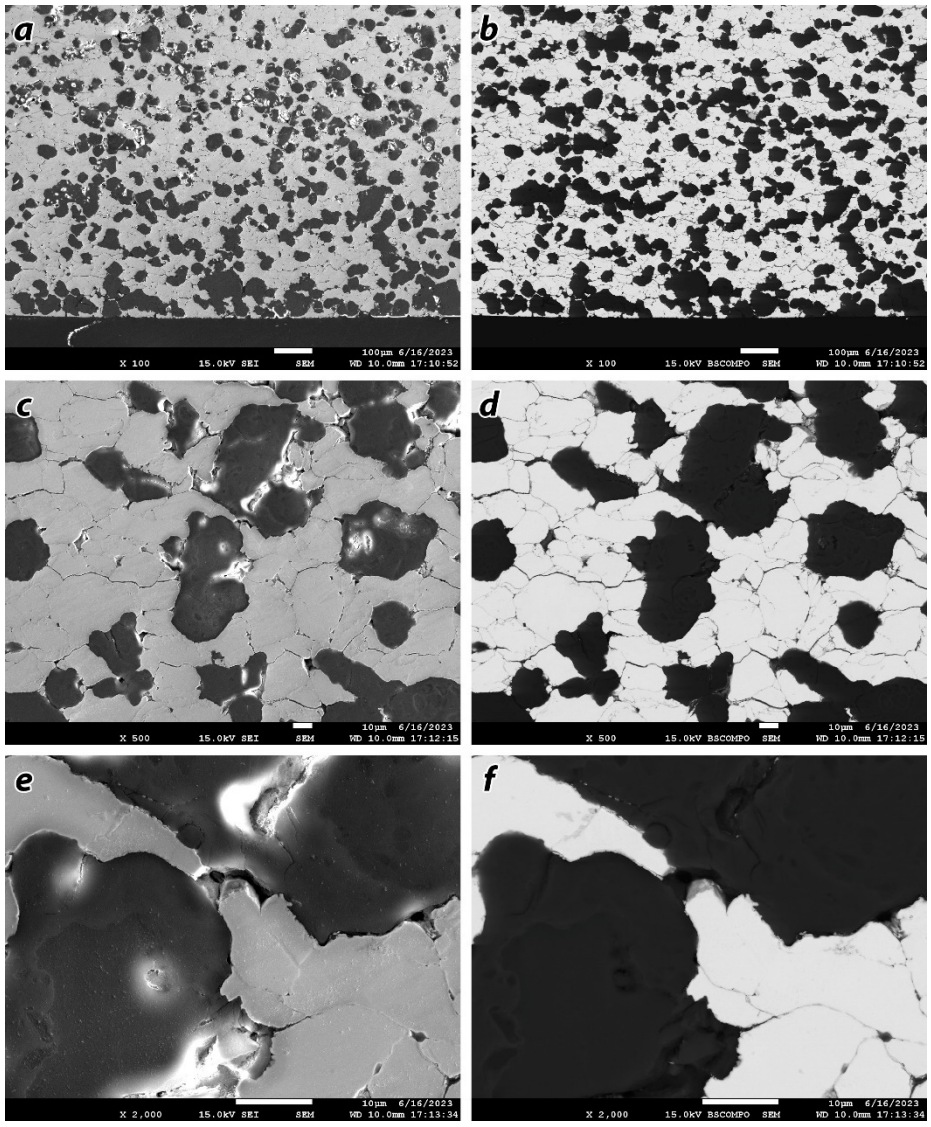

Figure 4-23. SEM including (a,c,e) SEI and (b,d,f) BSE micrographs of side-2 of the Set-2b pellet taken at (a,b) 100×, (c,d) 500×, and (e,f) 2k× magnifications.

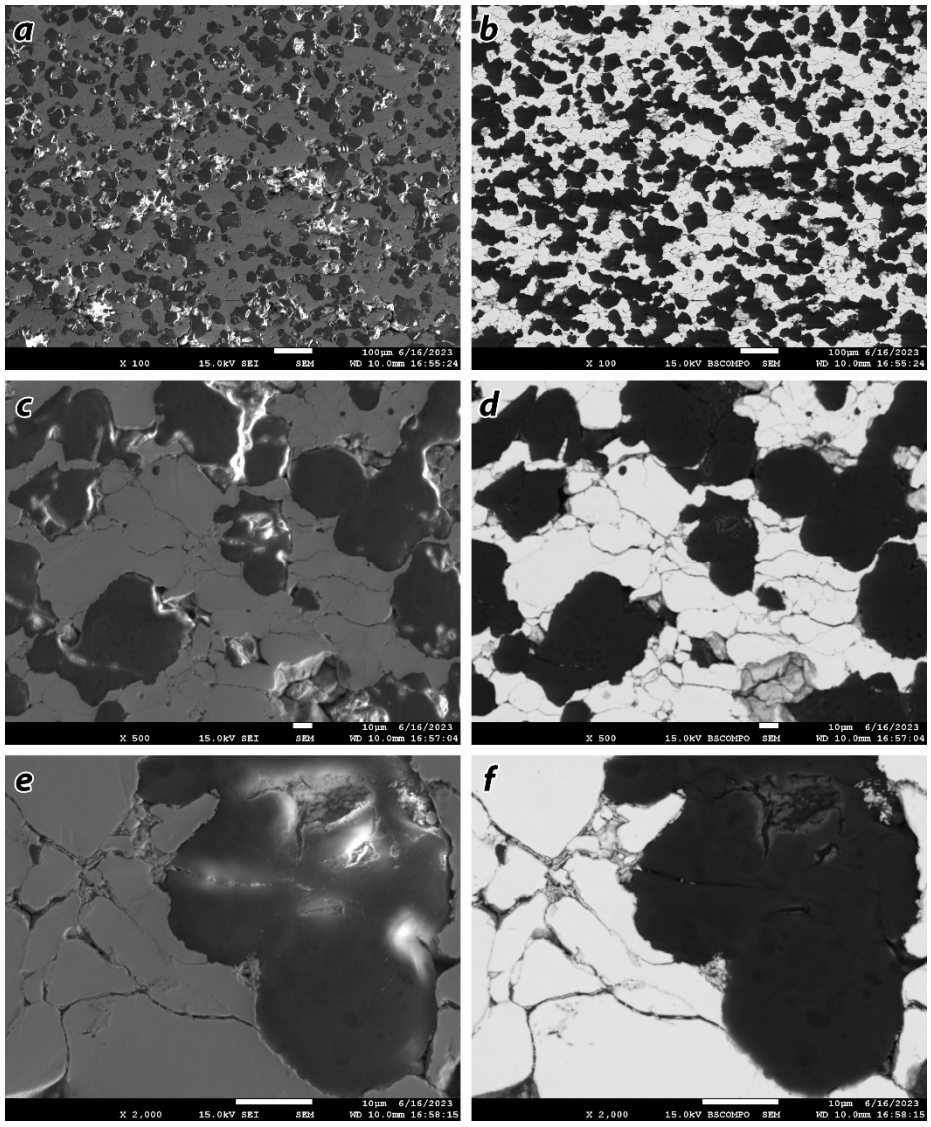

Figure 4-24. SEM including (a,c,e) SEI and (b,d,f) BSE micrographs of side-1 of the Set-2c pellet taken at (a,b) 100×, (c,d) 500×, and (e,f) 2k× magnifications.

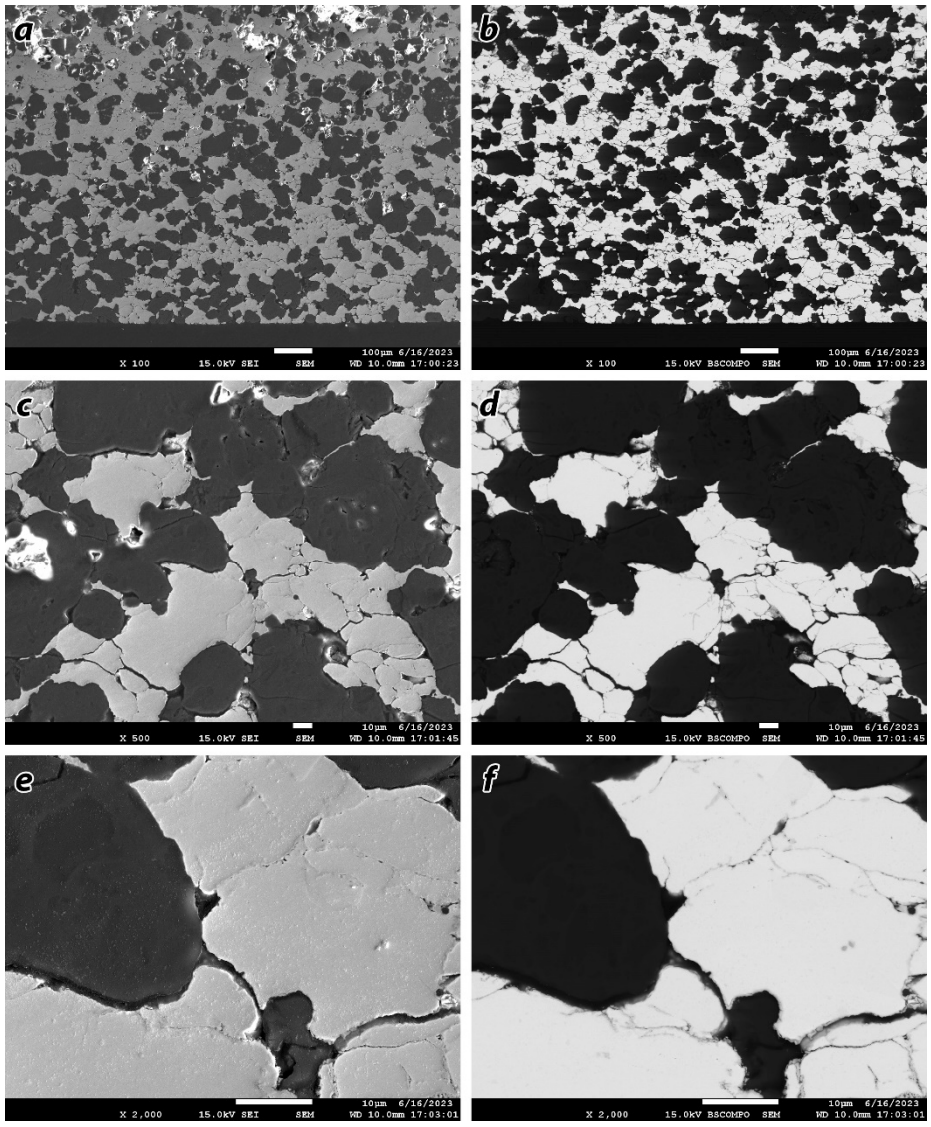

Figure 4-25. SEM including (a,c,e) SEI and (b,d,f) BSE micrographs of side-2 of the Set-2c pellet taken at (a,b) 100×, (c,d) 500×, and (e,f) 2k× magnifications.

4.8 Two-Phase Pellets with Iodine (Set-3, Set-4, & Set-5)

A summary of the data from the two-phase waste form pellets containing MI_x phases is provided in Table 4-7 that includes Set-3, Set-4, and Set-5 pellets. The specific details for each set are described in the subsections below.

Table 4-7. Summary of data from Set-3, Set-4, and Set-5 pellets.

Pellet Number:	3a	3b	3c	4a	5a	5b
Alternative ID	100Bi(v)	85Bi-AgI(v)	70Bi-AgI(v)	70Bi-CuI(v)	70BiSn-CuI	70BiSn-AgI
Date	5/22/2023	5/22/2023	5/22/2023	5/24/2023	5/24/2023	5/24/2023
Phase-a (comp.)	Bi^0	Bi^0	Bi^0	Bi^0	$BiSn^0$	$BiSn^0$
Phase-b (comp.)	–	AgI	AgI	CuI	CuI	AgI
Phase-a (mass, g)	1.9253	1.4750	1.1061	1.1041	1.0207	1.0217
Phase-b (mass, g)	–	0.2611	0.4747	0.4734	0.4373	0.4373
C%m (MI_x, m%)	0.00%	100.00%	100.00%	100.00%	100.00%	100.00%
mf_I (mass fract.)	0.00%	54.05%	54.05%	66.63%	66.63%	54.05%
$t_{p,g}$ (mm)	2.59	2.56	2.58	2.59	2.57	2.61
$m_{p,g}$ (g)	1.9108	1.7091	1.5628	1.5599	1.4447	1.4484
Atmosphere type	Vac	Vac	Vac	Vac	Air	Air
T_{ht} (°C)	203	203	203	203	104	104
t_{ht} (h)	22	22	22	20	8	8
Ramp (°C/min)	–	–	–	–	5	5
$t_{p,f}$ (mm)	2.593	2.553	2.510	2.583	2.550	2.530
$m_{p,f}$ (g)	1.9192	1.7097	1.564	1.5609	1.4448	1.4493
Δm (mass%)	0.44%	0.04%	0.08%	0.06%	0.01%	0.06%
ρ_b (g/cm^3)	9.4226	8.5256	7.9347	7.6932	7.2140	7.2937
$\rho_{b,em}$ (g/cm^3)	9.7828	9.7828	9.7828	9.7828	8.5588	8.5588
$\rho_{b,MIx}$ (g/cm^3)	–	5.68	5.68	5.67	5.67	5.68
$WL_{I,m}$ (m%)	0.00%	8.13%	16.23%	20.00%	19.99%	16.20%
$WL_{MI,v}$ (vol%)	0.00%	23.36%	42.50%	42.52%	39.27%	39.21%
$V_{\%T}$ (vol%)	104.3%	101.9%	100.2%	103.3%	102.0%	101.2%

4.8.1 Bismuth with AgI (Set-3)

The set-3 pellet data are summarized in this section. This set included a pure Bi^0 pellet (3a) and Bi^0 mixed with different amounts of AgI including 15 mass% AgI (Set-3b) and 30 mass% AgI (Set-3c). Images of each pellets from Set-3 are shown in Figure 4-26 and a summary of the optical micrographs are shown in Figure 4-27.

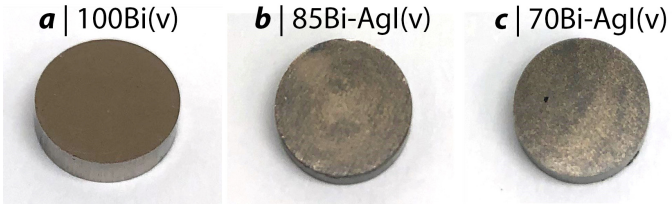

Figure 4-26. Pictures of the Set-3 (3a, 3b, 3c) pellets that include (a) 100Bi(v), (b) 85Bi-AgI(v), and (c) 70Bi-AgI(v). All pellets are 1-cm diameter.

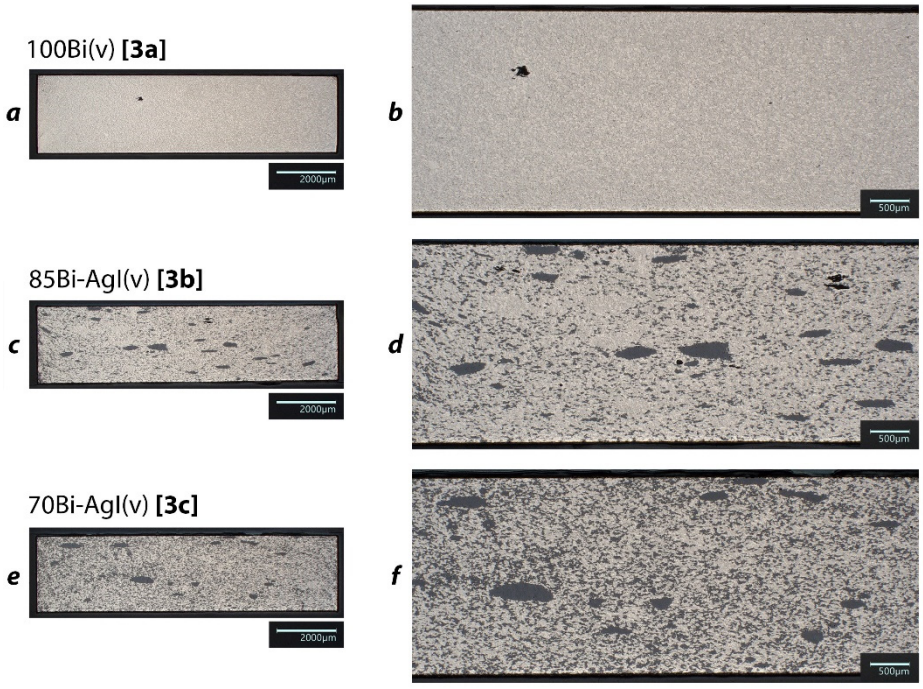

Figure 4-27. Cross-sectional optical micrographs of two-phase set-3 pellets including (a,b) 100Bi(v) [3a], (c,d) 85Bi-AgI(v) [3b], and (e,f) 70Bi-AgI(v) [3c] taken at (a,c,e) 20× and (b,d,f) 50× magnifications. These pellets were fired under vacuum at 203°C for 22 h in the vacuum oven.

The SEM micrographs for the Set-3a pellet are shown in Figure 4-28 and Figure 4-29, for Set-3b are shown in Figure 4-30 and Figure 4-31, and for Set-3c are shown in Figure 4-33 and Figure 4-34. EDS micrographs of Set-3b and Set-3c pellets are shown in Figure 4-32 and Figure 4-35, respectively. The SEM micrographs in Figure 4-30, Figure 4-31, and Figure 4-32 show the uniform distribution of AgI and Figure 4-33, Figure 4-34, and Figure 4-35 show the distribution of CuI in the Bi^0 matrix. In some cases, it is clear that large agglomerates of the metal iodide were present in the pellet. These could be broken up prior to pelletization and heat treatment using ball milling or another size reduction technique. Grain boundaries between the Bi^0 particles are seen clearly in the BSE SEM micrographs in all Set-3 pellets. These could likely be reduced with a higher heat-treatment temperature, but the sintering temperature used in this study for Bi^0 encapsulant pellets was done to remain near the T_d for PAN (see Table 2-3).

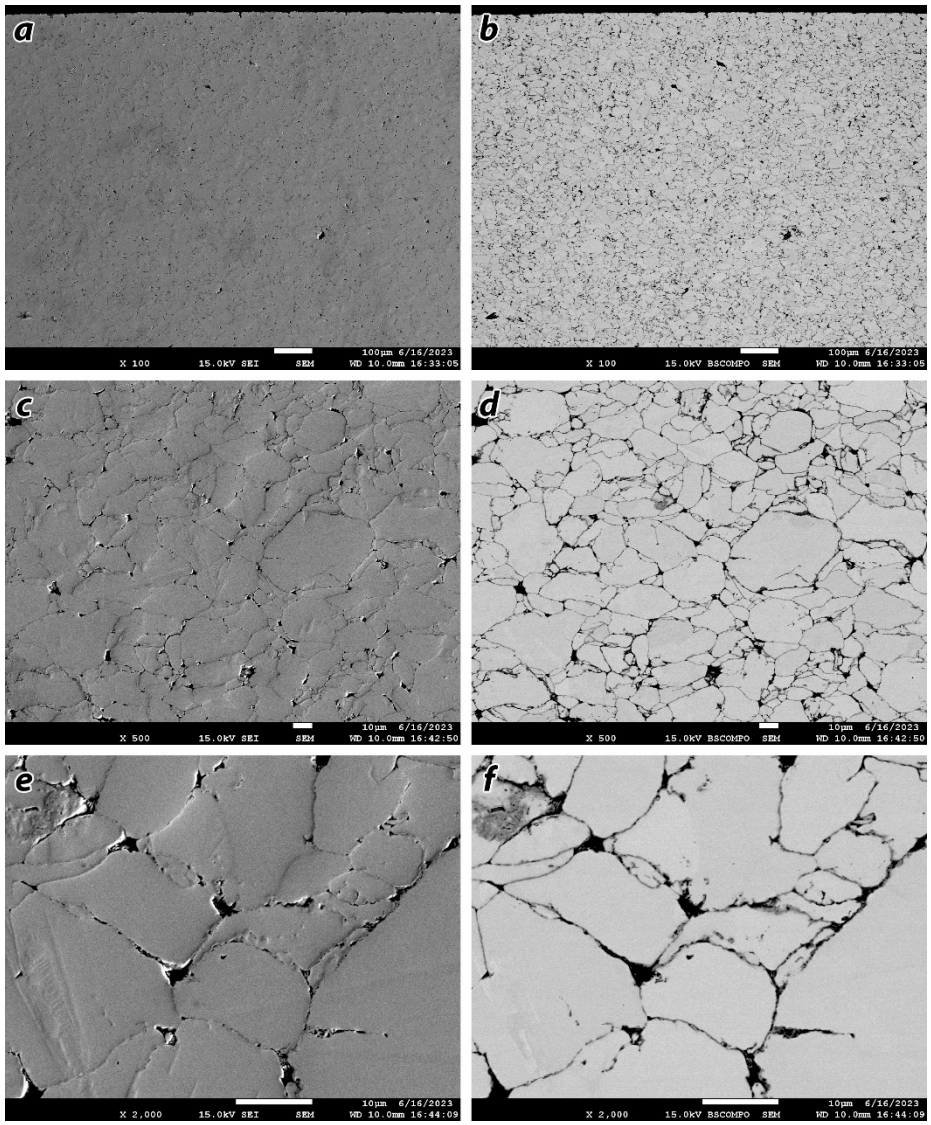

Figure 4-28. SEM including (a,c,e) SEI and (b,d,f) BSE micrographs of side-1 of the Set-3a pellet taken at (a,b) 100×, (c,d) 500×, and (e,f) 2k× magnifications.

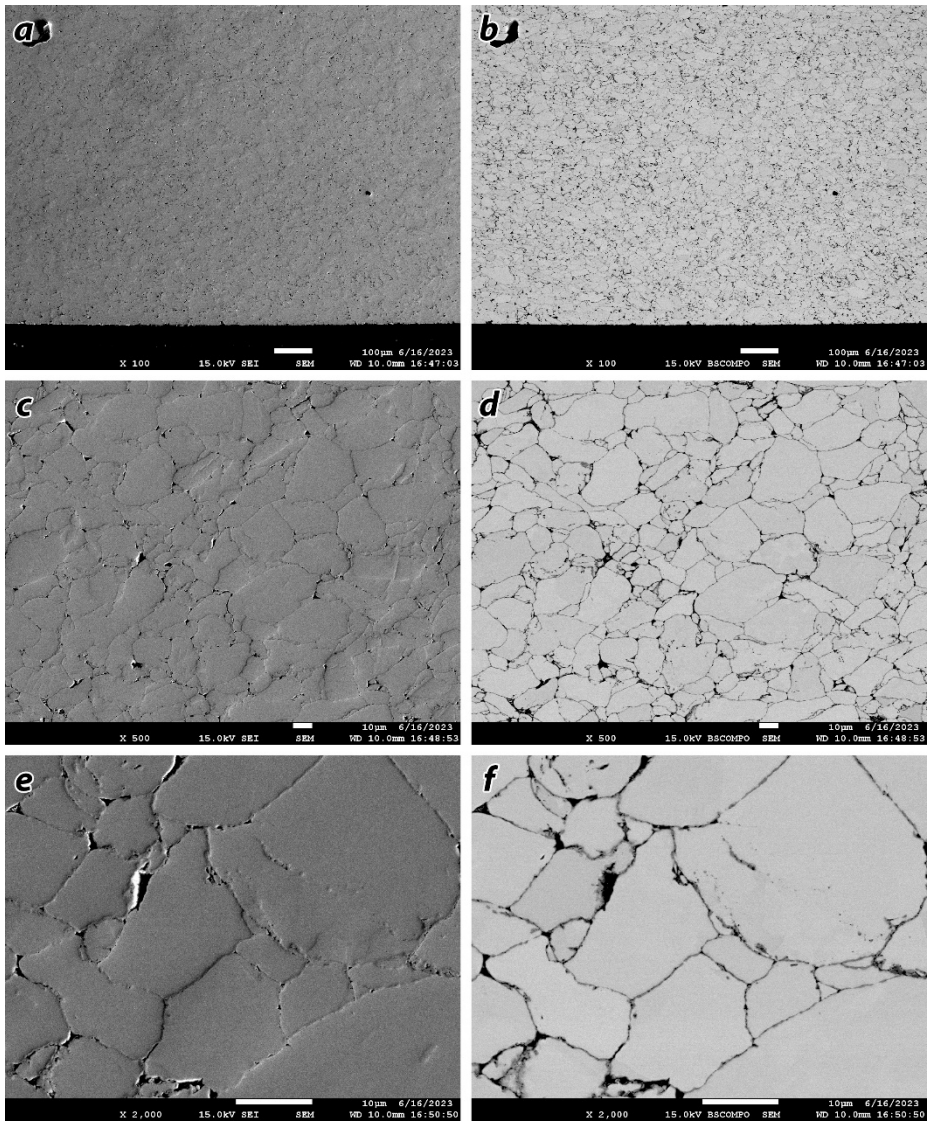

Figure 4-29. SEM including (a,c,e) SEI and (b,d,f) BSE micrographs of side-2 of the Set 3a pellet taken at (a,b) 100×, (c,d) 500×, and (e,f) 2k× magnifications.

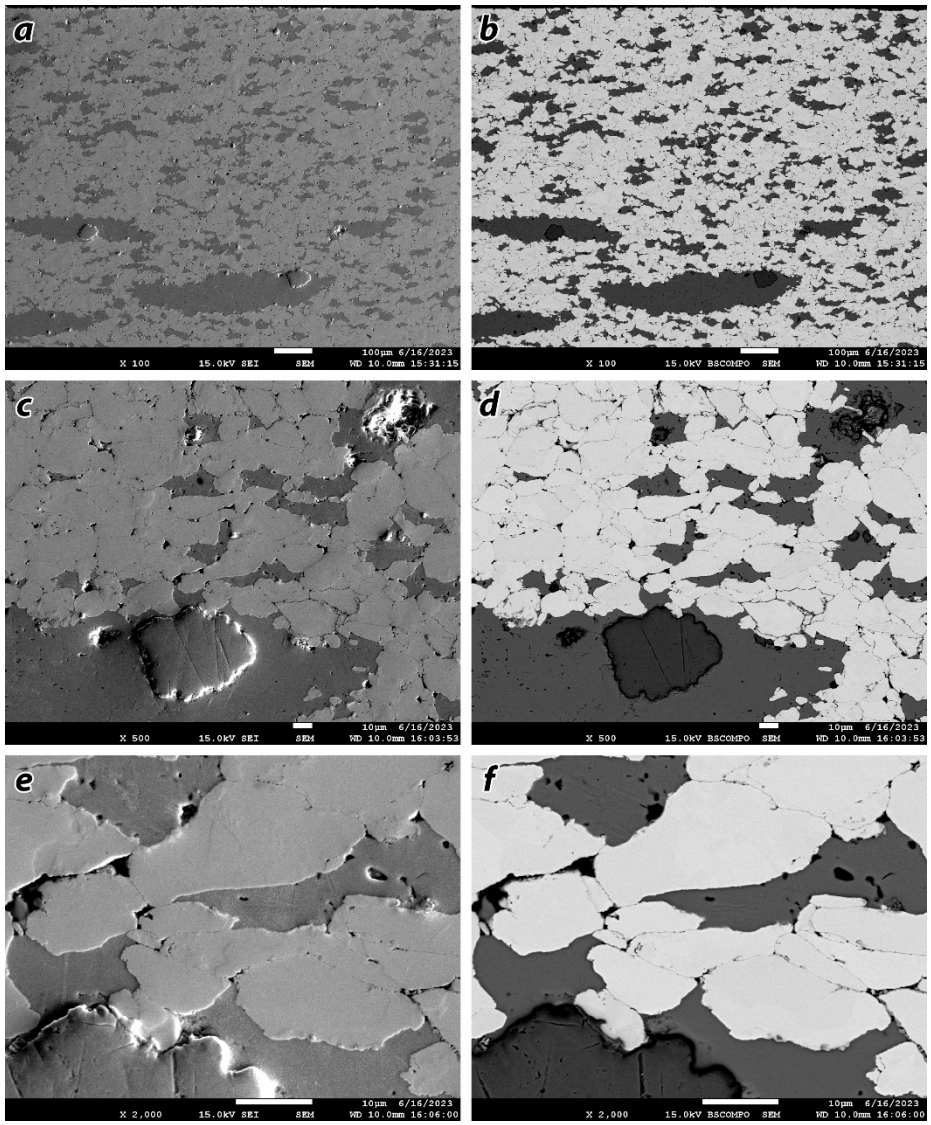

Figure 4-30. SEM including (a,c,e) SEI and (b,d,f) BSE micrographs of side-1 of the Set-3b pellet taken at (a,b) 100×, (c,d) 500×, and (e,f) 2k× magnifications.

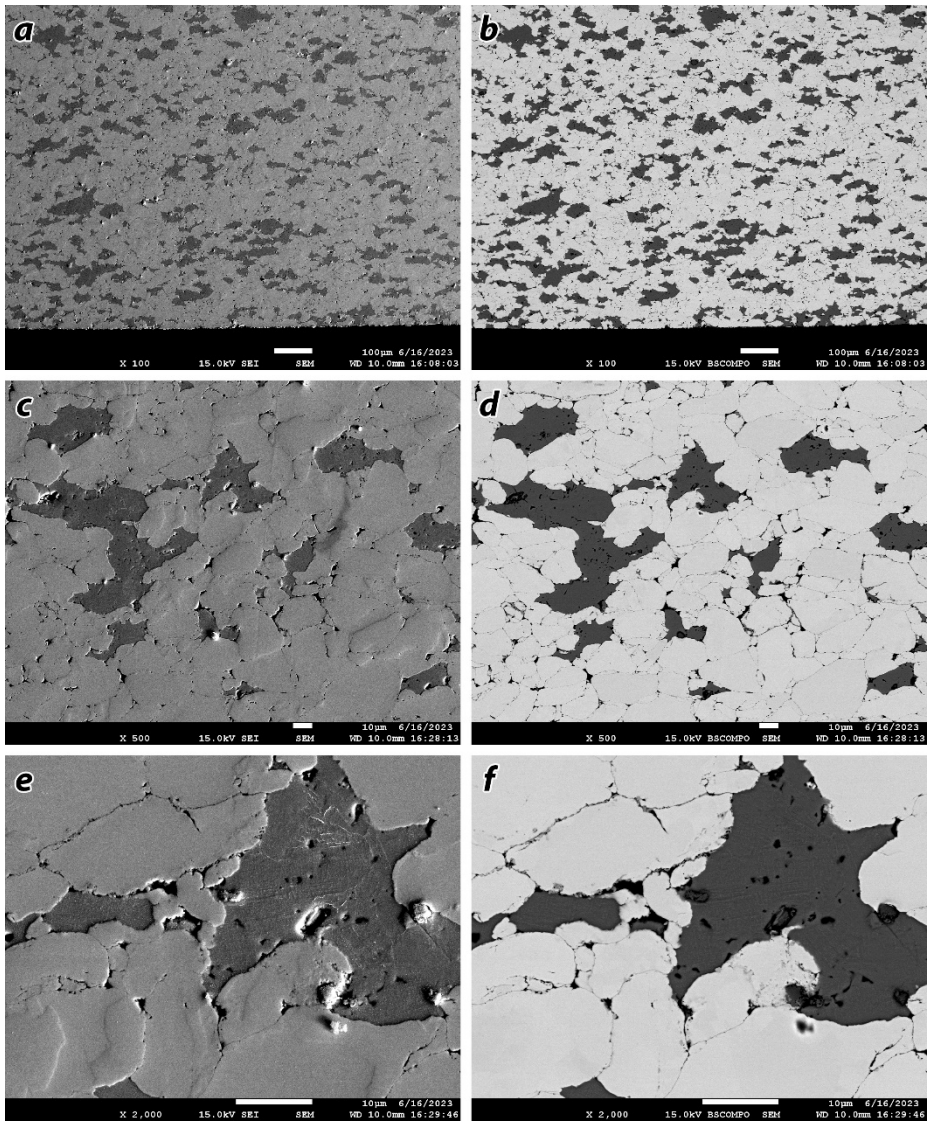

Figure 4-31. SEM including (a,c,e) SEI and (b,d,f) BSE micrographs of side-2 of the Set-3b pellet taken at (a,b) 100×, (c,d) 500×, and (e,f) 2k× magnifications.

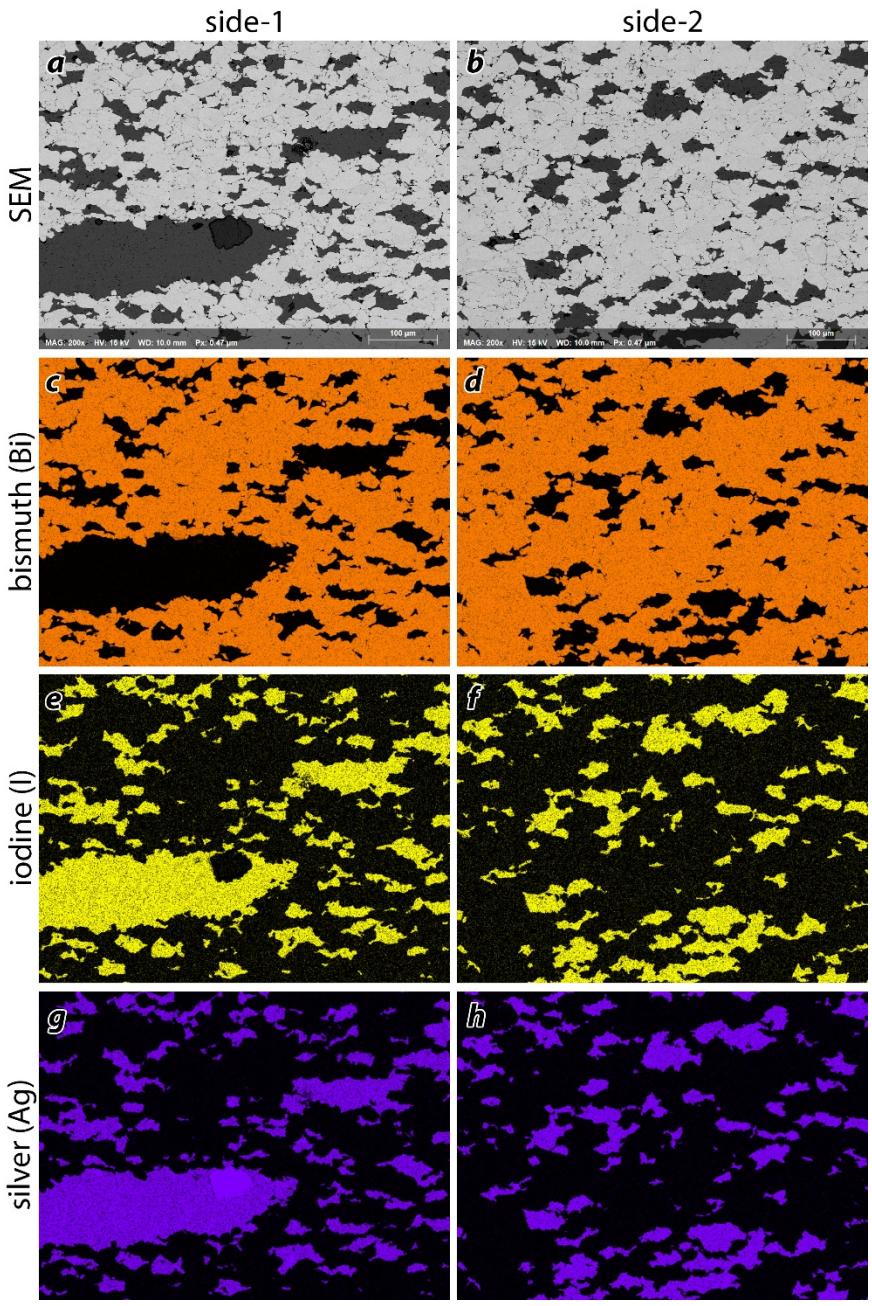

Figure 4-32. EDS collage of the Set-3b pellet at two different locations showing the distribution of the metal (Bi) matrix and the AgI phase.

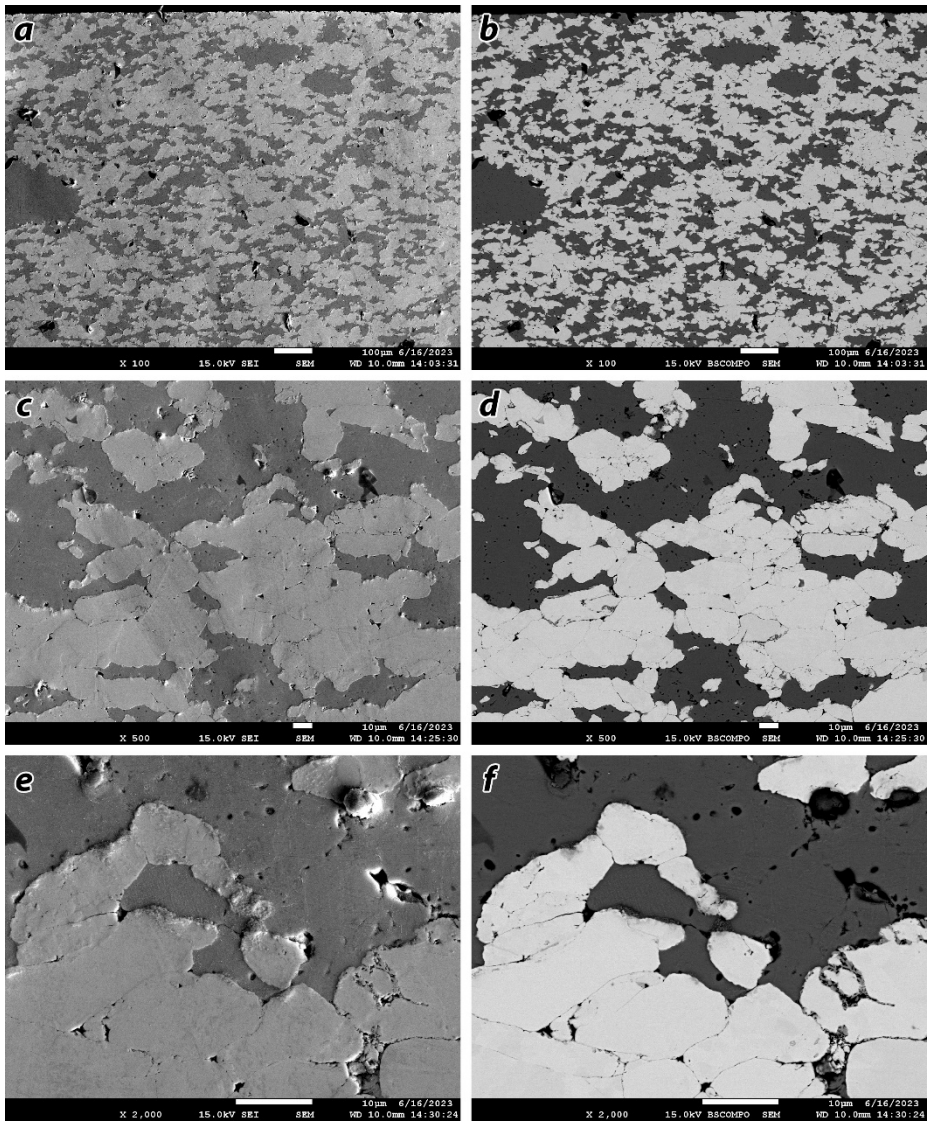

Figure 4-33. SEM including (a,c,e) SEI and (b,d,f) BSE micrographs of side-1 of the Set-3c pellet taken at (a,b) 100×, (c,d) 500×, and (e,f) 2k× magnifications.

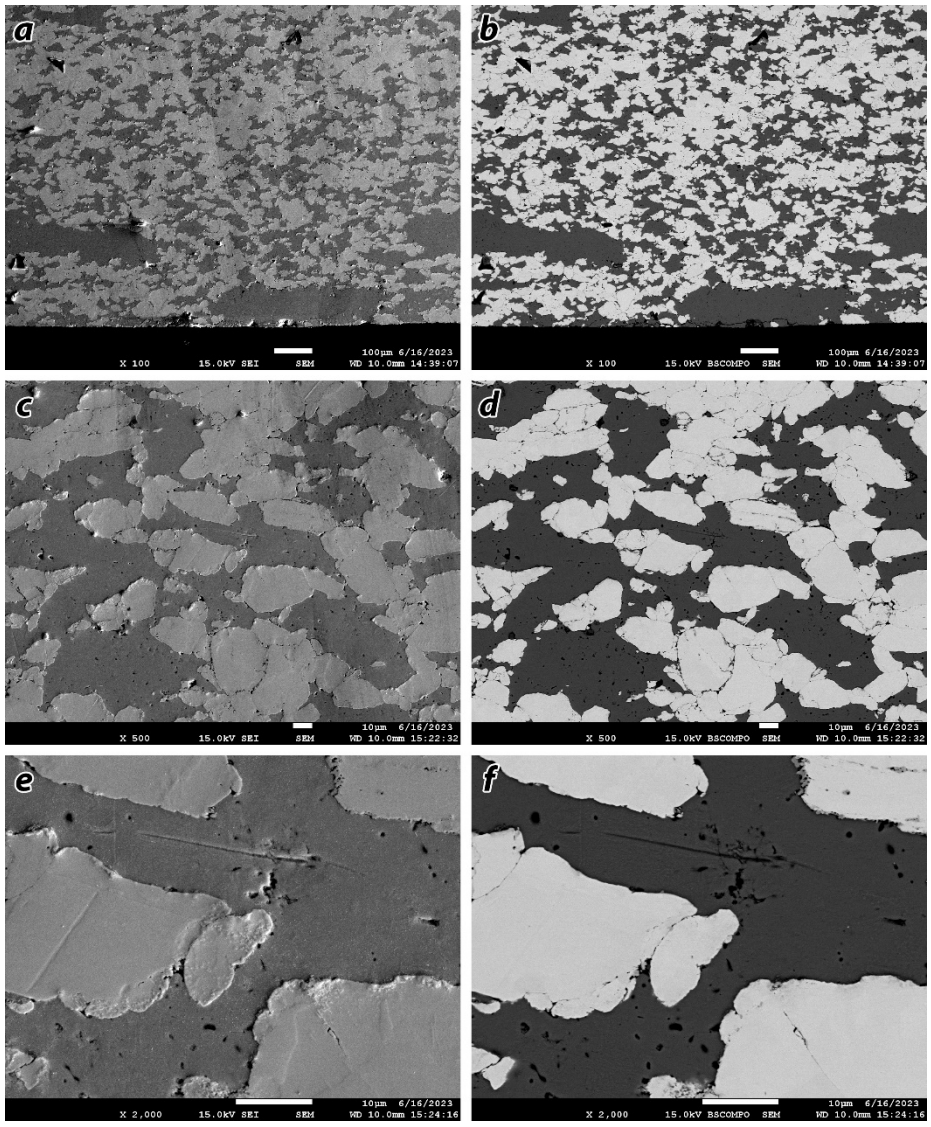

Figure 4-34. SEM including (a,c,e) SEI and (b,d,f) BSE micrographs of side-2 of the Set-3c pellet taken at (a,b) 100×, (c,d) 500×, and (e,f) 2k× magnifications.

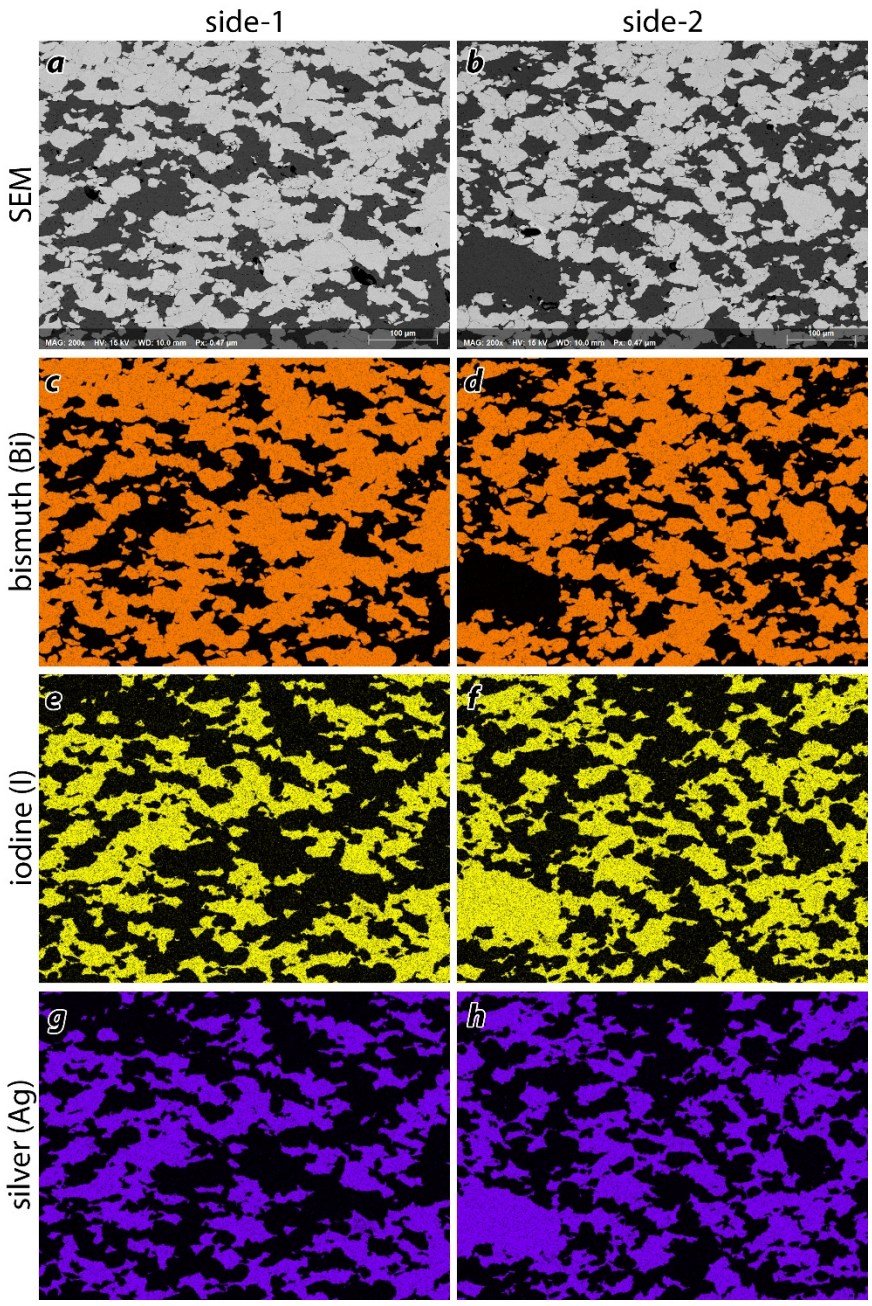

Figure 4-35. EDS collage of the Set-3c pellet at two different locations showing the distribution of the metal (Bi) matrix and the AgI phase.

4.8.2 Bismuth with CuI (Set-4)

The Set-4 pellet data are summarized in this section. This set included 30 mass% CuI inside a Bi^0 encapsulant. Optical micrographs of Set-4 pellet are provided in Figure 4-36. SEM micrographs are provided for this sample in Figure 4-37 and Figure 4-38 and an EDS map is provided in Figure 4-39. In this sample, the CuI was evenly distributed around the Bi-metal matrix.

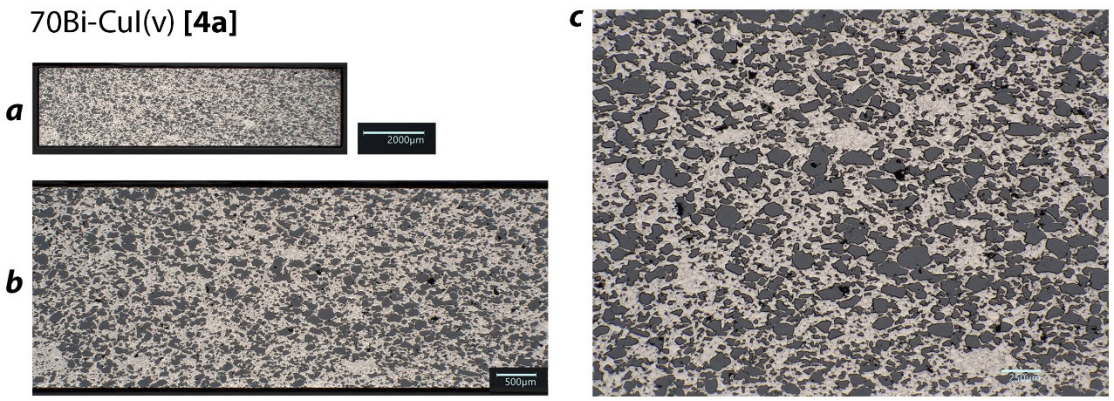

Figure 4-36. Cross-sectional optical micrographs of two-phase set-4 pellet of 70Bi-CuI(v) [4a] taken at (a) 20×, (b) 50×, and (c) 100× magnifications. This pellet was fired under vacuum at 203°C for 20 h in the vacuum oven.

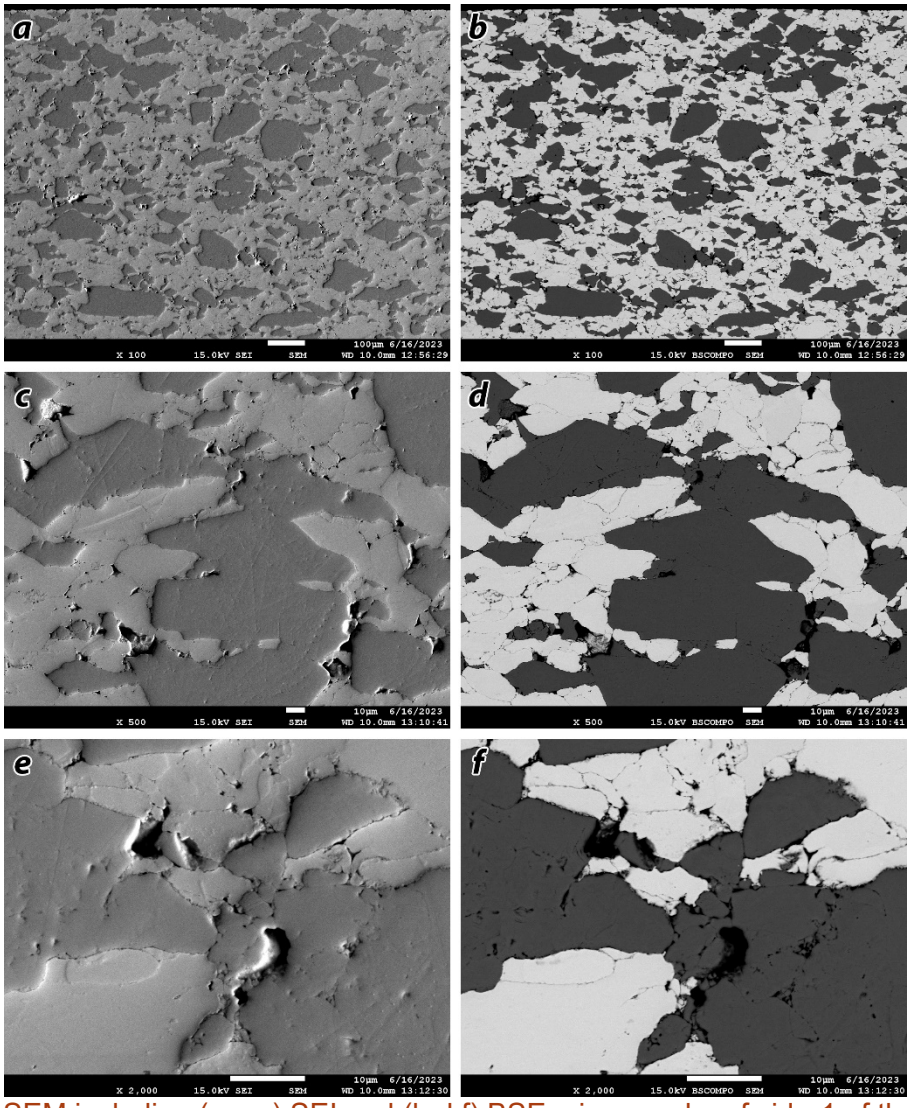

Figure 4-37. SEM including (a,c,e) SEI and (b,d,f) BSE micrographs of side-1 of the Set-4 pellet taken at (a,b) 100×, (c,d) 500×, and (e,f) 2k× magnifications.

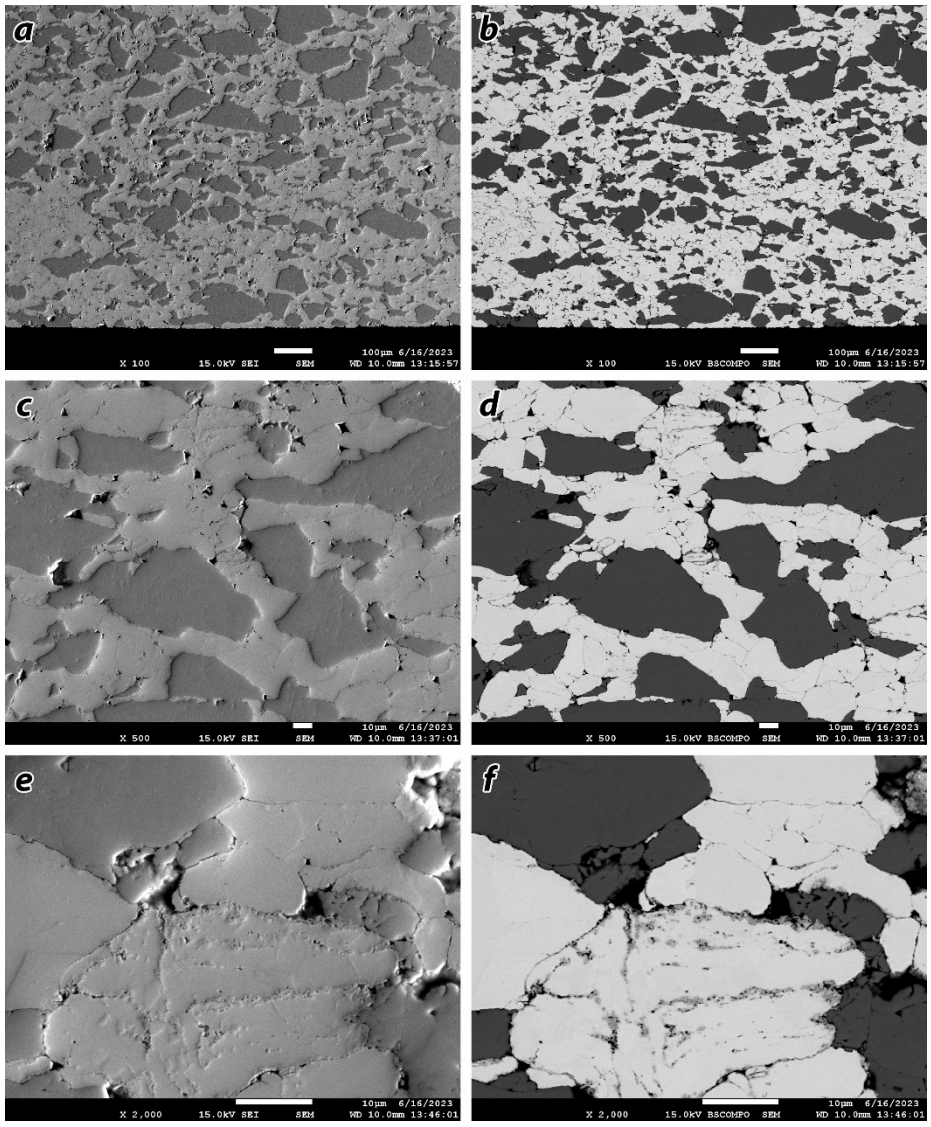

Figure 4-38. SEM including (a,c,e) SEI and (b,d,f) BSE micrographs of side-2 of the Set-4 pellet taken at (a,b) 100×, (c,d) 500×, and (e,f) 2k× magnifications.

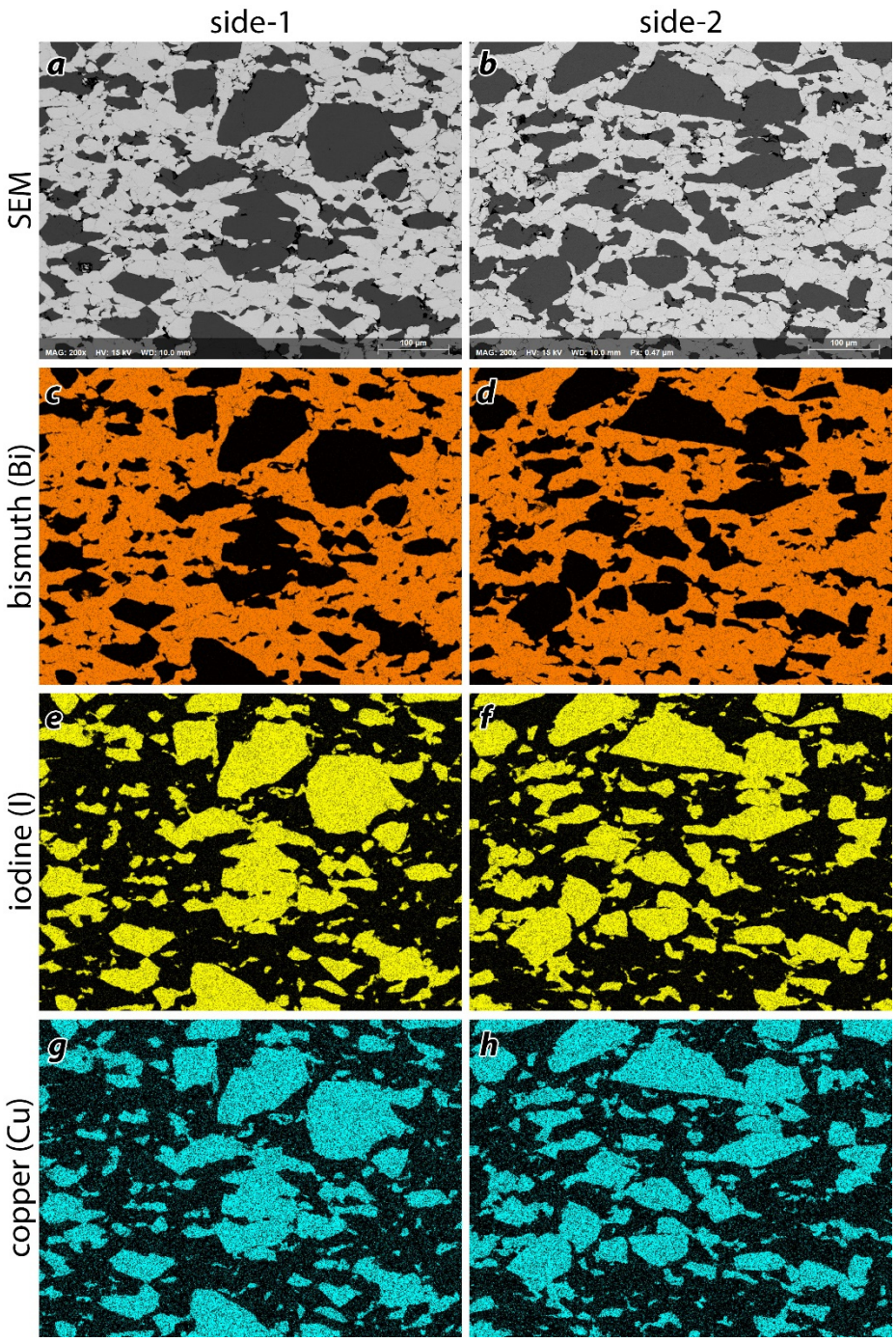

Figure 4-39. EDS collage of the Set-4 pellet at two different locations showing the distribution of the metal (Bi) matrix and the CuI phase.

4.8.3 Bismuth-Tin Alloy with AgI or CuI (Set-5)

Pictures of the Set-5 pellets are provided in Figure 4-40 and optical micrographs are provided in Figure 4-41. The Bi-Sn alloy did not work as effectively as a metal encapsulant as the pure Bi^0 based on some strange partitioning observed in Set-5b. This conclusion was based off of several factors described below.

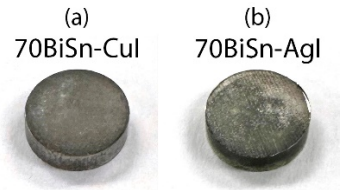

Figure 4-40. Pictures of Set-5 pellets (5a, 5b) that include (a) 70BiSn-CuI and (b) 70BiSn-AgI. Both pellets are 1-cm diameter.

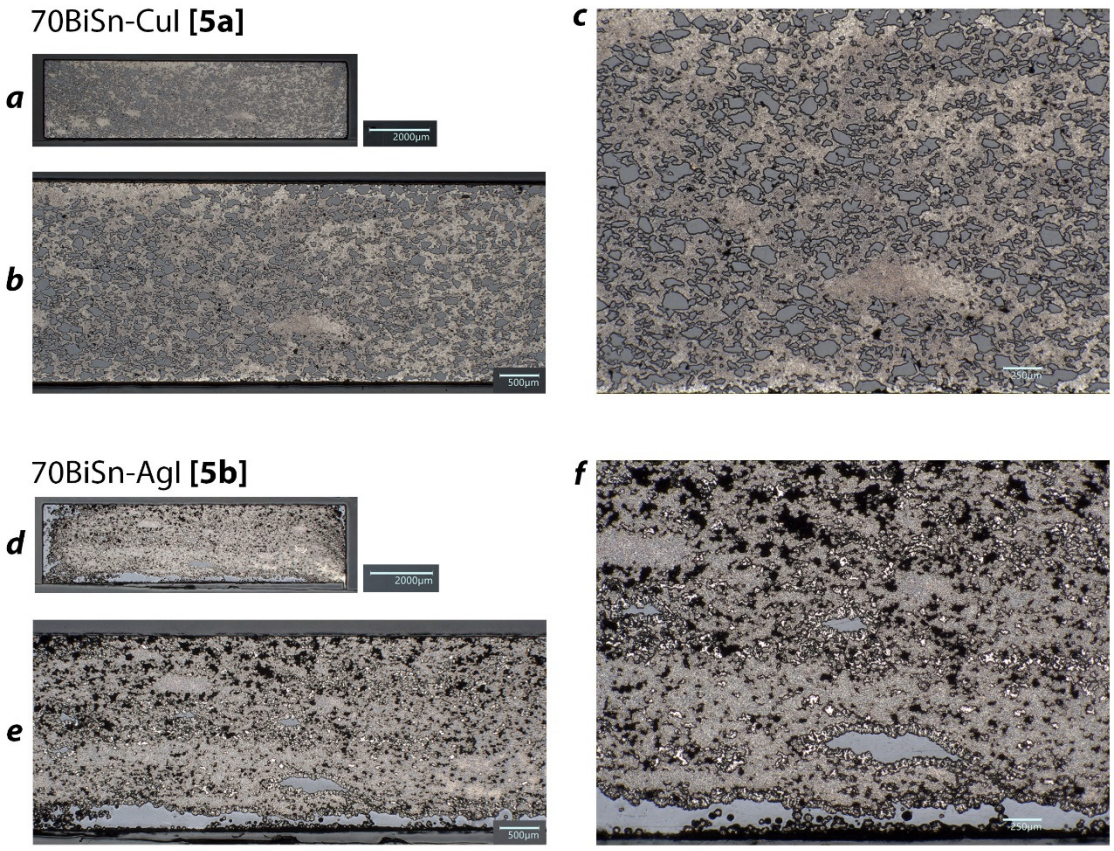

Figure 4-41. Cross-sectional optical micrographs of two-phase set-5 pellets including (a–c) 70BiSn-CuI [5a] and (d–f) 70BiSn-AgI [5b] taken at (a,d) 20×, (b,e) 50×, and (c,f) 100× magnifications. These pellets were fired in air at 104°C for 8 h in a Thermolyne box furnace.

SEM micrographs for Set-5a and Set-5b are provided in Figure 4-42 and Figure 4-44, respectively, with EDS maps provided in Figure 4-43 and Figure 4-45, respectively. Some clear differences were observed in these pellets compared to the previous sets with the primary difference being the use of the Bi-Sn alloy in this set versus Bi^0 only in the previous sets. The Bi-Sn metal shows up as a heterogeneous matrix as expected but with what looks like Sn-rich regions around the metallic boundaries; this Sn segregation suggests some heterogeneity regarding Sn-rich regions and Bi-rich regions. While the Set-5a (CuI) pellet looked very consistent from region to region within the pellet, the Set-5b (AgI) pellet looked very different. The AgI pellet showed evidence of AgI decomposition, which is quite strange considering that these were heat treated at a much lower temperature (104°C) than the previous AgI-containing pellets (203°C). In the Set-5b pellet, regions showing compositional inconsistencies were observed including Ag-rich and I-rich areas along with large regions on the pellet edges that appeared to be AgI. Another strange observation is the structure of the metallic regions where the Set-5b metallic phase

appears as interconnected spherical (circular) areas (see Figure 4-44 and Figure 4-45), which was not the case with the Set-5a pellet (see Figure 4-42 and Figure 4-43).

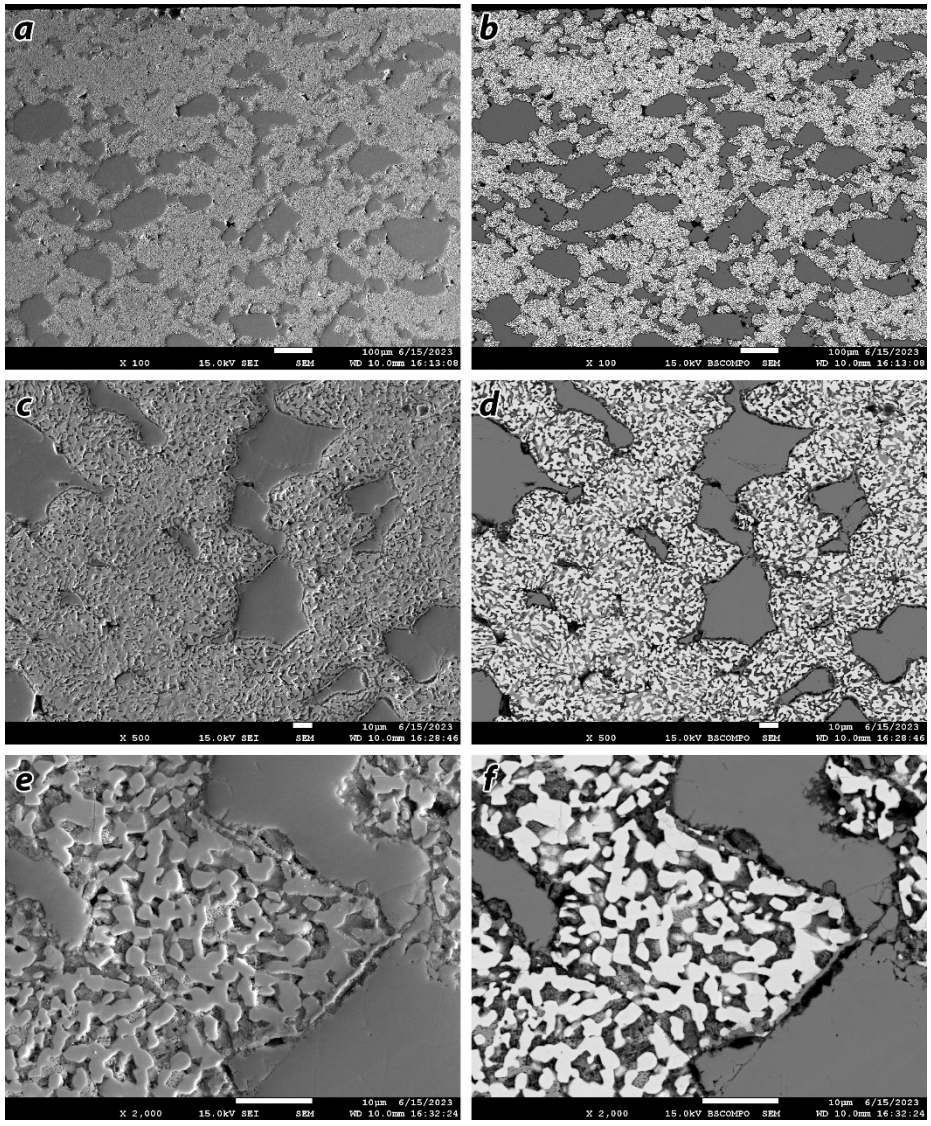

Figure 4-42. SEM including (a,c,e) SEI and (b,d,f) BSE micrographs of the Set-5a pellet taken at (a,b) 100×, (c,d) 500×, and (e,f) 2k× magnifications.

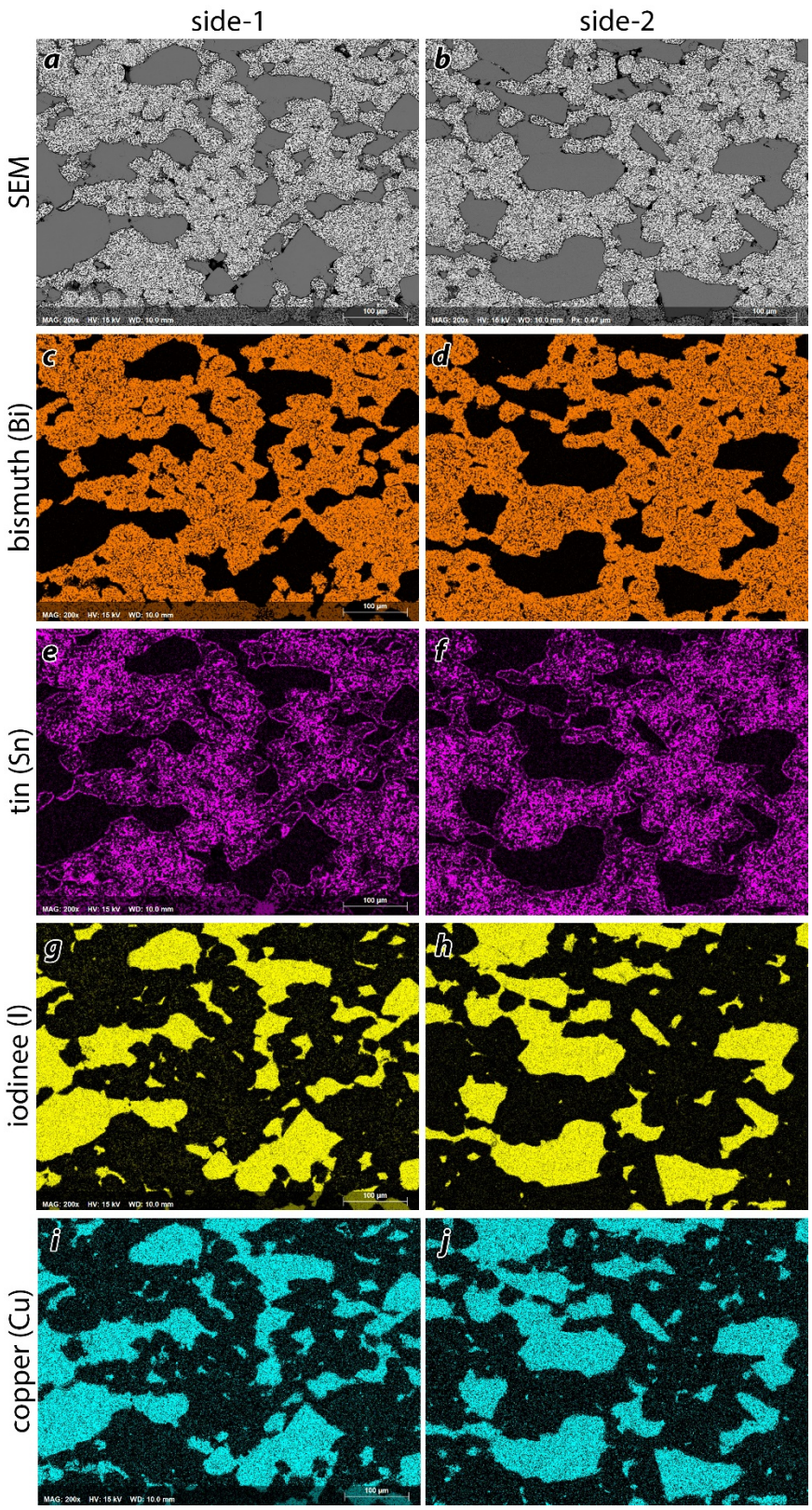

Figure 4-43. EDS collage of the Set-5a pellet at two different locations showing the distribution of the metal (Bi-Sn) matrix and the CuI phase.

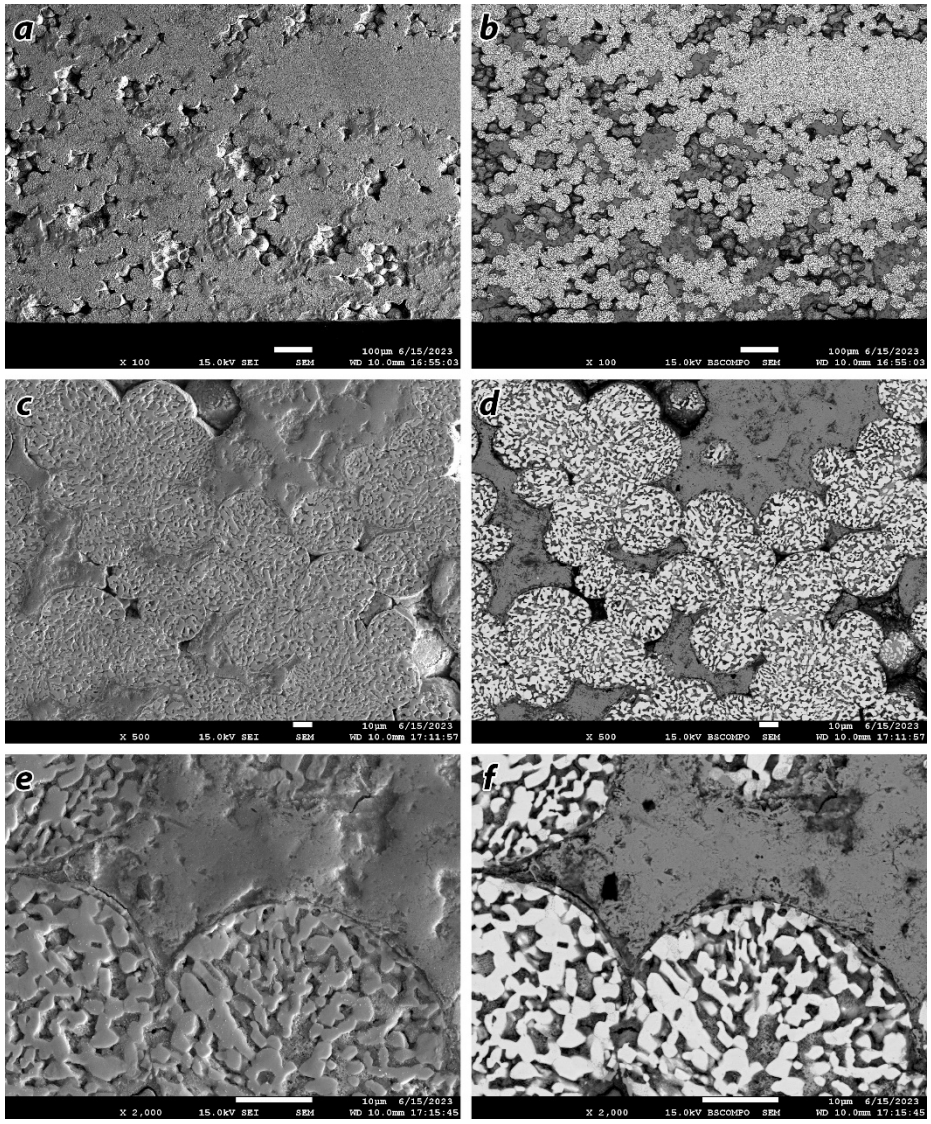

Figure 4-44. SEM including (a,c,e) SEI and (b,d,f) BSE micrographs of the Set-5b pellet taken at (a,b) 100×, (c,d) 500×, and (e,f) 2k× magnifications.

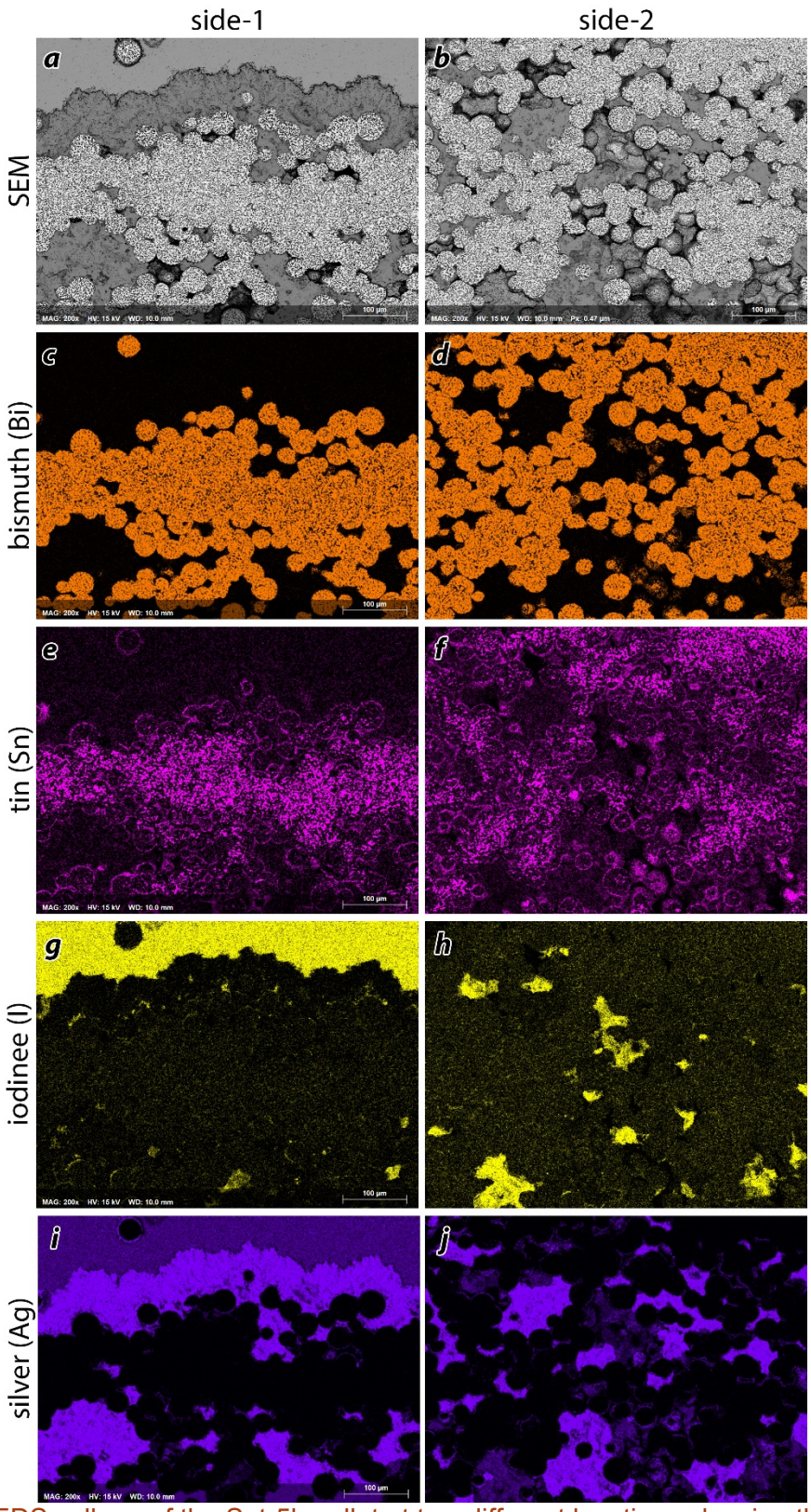

Figure 4-45. EDS collage of the Set-5b pellet at two different locations showing the distribution of the metal (Bi-Sn) matrix and the AgI phase.

The spot EDS data for the Set-5b pellet is provided in Figure 4-46 and Table 4-8 in terms of both mass% (Figure 4-46b) and atomic% (Figure 4-46c). From these, it appears that the darkest layer (regions 6-10) is rich in Ag and contains the highest fraction of oxygen (i.e., 10.86 ± 0.7 at%). The top layer (regions 1-5) was stoichiometrically very close to AgI on an atomic basis (i.e., 47.4 ± 1.7 at% Ag and 50.3 ± 2.0 at% I). The middle region was pretty close to the eutectic Bi-Sn compound at 43.2 at% Sn and 56.8 at% Bi (renormalized) but oxygen was detected in this phase (>10 at%).

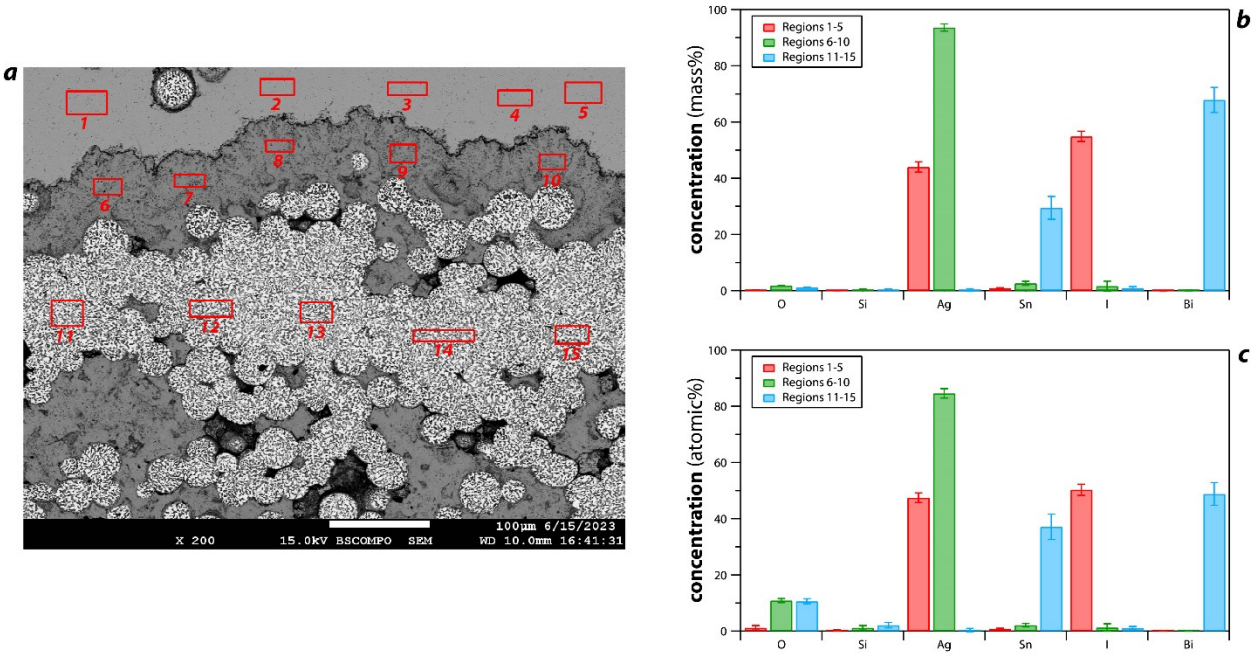

Figure 4-46. Spot EDS data for Set-5b pellet including (a) SEM micrograph with EDS locations, (b) EDS data in mass%, and (c) EDS data in atomic%.

Table 4-8. Summary of spot EDS analysis on Set-5b pellet (see Figure 4-46) shown as AVE values (top) and SD values (bottom, ± 1σ).

Element	Mass%			Atomic%		
Regions:	**1-5**	**6-10**	**11-15**	**1-5**	**6-10**	**11-15**
O	0.16	1.78	1.13	1.16	10.86	10.59
	0.11	0.13	0.10	0.80	0.70	0.91
Si	0.06	0.34	0.39	0.27	1.19	2.11
	0.06	0.23	0.17	0.24	0.79	0.93
Ag	44.02	93.60	0.25	47.43	84.55	0.34
	1.85	1.26	0.43	1.73	1.64	0.60
Sn	0.84	2.59	29.44	0.83	2.13	37.13
	0.22	0.72	4.07	0.22	0.60	4.50
I	54.90	1.63	0.90	50.30	1.25	1.05
	1.82	1.76	0.53	1.98	1.35	0.62
Bi	0.01	0.05	67.89	0.01	0.02	48.77
	0.03	0.10	4.42	0.02	0.04	4.06

Based on these data, it is unclear what occurred during the heat treatment of this sample. It appears as though the AgI decomposed, the residual Ag oxidized partially, and likely some iodine

evolved. The Ag-rich phase also contained some Sn (>2 at%). However, based on a review of the Sn-Ag phase diagram (Kim et al. 2010; Kabatesi and Wang 2022), the eutectic Ag-Sn compound (i.e., 96.5Sn-3.5Ag) melts at 221°C, which is well below the temperature where these pellets were heat treated. The presence of Si in these materials is attributed to contamination from the processes used to create the pellets and are likely near the signal-to-noise limits of the EDS detector.

4.9 Three-Phase Waste Forms (Set-6 and Set-7)

4.9.1 Without Grinding the Samples (Set-6)

The data for Set-6 pellets are provided in Table 4-9 below. Images of these pellets are provided in Figure 4-47. For Set-6b and Set-6c, the AgI-PAN$^{(c)}$ material was used (i.e., sample I-2b in Table 4-3). The AgI-PAN(a) was loaded directly into the die as full-sized beads along with added Bi^0 particles (approach shown in Figure 3-4b). In the (b2) image shown in Figure 4-47, it is clear that the Bi^0 particles added with the AgI-PAN(a) beads did not full encapsulate the AgI-PAN(a) phase. Thus, for the Set-6c pellet, another Bi-metal layer was added on top of the middle layer with the intent to sandwich the AgI-PAN(a) within a Bi^0 matrix (see Figure 3-4c).

Table 4-9. Summary of data from Set-6 pellets. Note that for 3-phase pellets, phase-b and phase-c were mixed together in the die prior to pelletization.

Pellet Number:	6a	6b	6c
Alternative ID	100Bi	Bi-AgIPAN	Bi-AgIPAN-Bi
Date	6/8/2023	6/8/2023	6/8/2023
Iodine loading source	–	I-2b in Table 4-3	I-2b in Table 4-3
Phase-a (comp.)	Bi	Bi	Bi
Phase-b (comp.)	–	AgI-PAN$^{(150)}$	AgI-PAN$^{(150)}$
Phase-c (comp.)	–	Bi^0	Bi^0
Phase-d (comp.)	–	–	Bi^0
Phase-a (mass, g)	0.3838	0.3848	0.3835
Phase-b (mass, g)	0.0000	0.1112	0.1274
Phase-c (mass, g)	0.0000	0.6337	0.6288
Phase-d (mass, g)	0.0000	0.0000	0.3834
***C*%m (*MI*$_x$, m%)**	0.00%	94.31%	94.31%
***mf*$_I$ mass fract.**	0.00%	45.42%	45.42%
$t_{p,g}$ (mm)	0.56	1.83	2.55
$m_{p,g}$ (g)	0.3753	1.1170	1.5111
Atmosphere type	Vac	Vac	Vac
T_{ht} (°C)	203	203	203
t_{ht} (h)	22	22	22
Ramp (°C/min)	–	–	–
$t_{p,f}$ (mm)	0.55	1.95	2.565
$m_{p,f}$ (g)	0.3761	1.1160	1.5108
Δm (*m*%)	0.21%	-0.09%	-0.02%
ρ_b (g/cm^3)	8.7066	7.2868	7.4995
$\rho_{b,em}$ (g/cm^3)	9.7828	9.7828	9.7828
$\rho_{b,MIx}$ (g/cm^3)	–	5.68	5.68
$WL_{I,m}$ (m%)	0.00%	4.47%	3.80%
V_{MIx}/m_{LS} (cm^3/g)	–	0.1479	0.1479
$WL_{MI,v}$ (vol%)	0.00%	13.64%	11.67%
$V\%_T$ (vol%)	112.6%	114.6%	114.2%

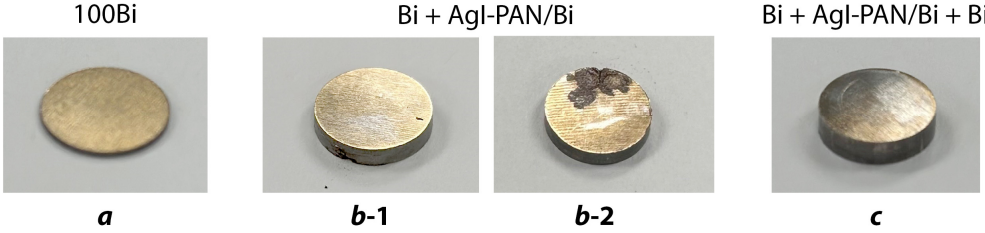

Figure 4-47. Pictures of 3-phase pellets including (a) pellet-6a (500-µm thick 100Bi^0 pellet), (b) pellet-6b (2-layer pellet including 500-µm thick Bi-layer under AgI-PAN+Bi^0 layer where b1 is Bi^0 layer side and b2 is the AgI-PAN+Bi^0 layer side), and (c) pellet-6c [the same approach as in (b) but with a 3rd layer of 100Bi^0 (500-µm thick) on the top of the AgI-PAN+Bi^0 layer]. All pellets are 1-cm diameter.

Optical micrographs of the set-6 pellets are provided in Figure 4-48. The different layers included in the pellets are shown on the far-right side of Figure 4-48c-f. It is also clear to see that the different layers did not adhere well to the nearby layers where clear gaps exist (Figure 4-48c-f).

The gaps around the AgIPAN layers could be due to different compressibilities and stresses around the PAN composite beads from the pellet pressing process or due to off-gas release from the beads (e.g., water) during the heat treatment process where pressure was built up in the pellet resulting in localized volume expansion.

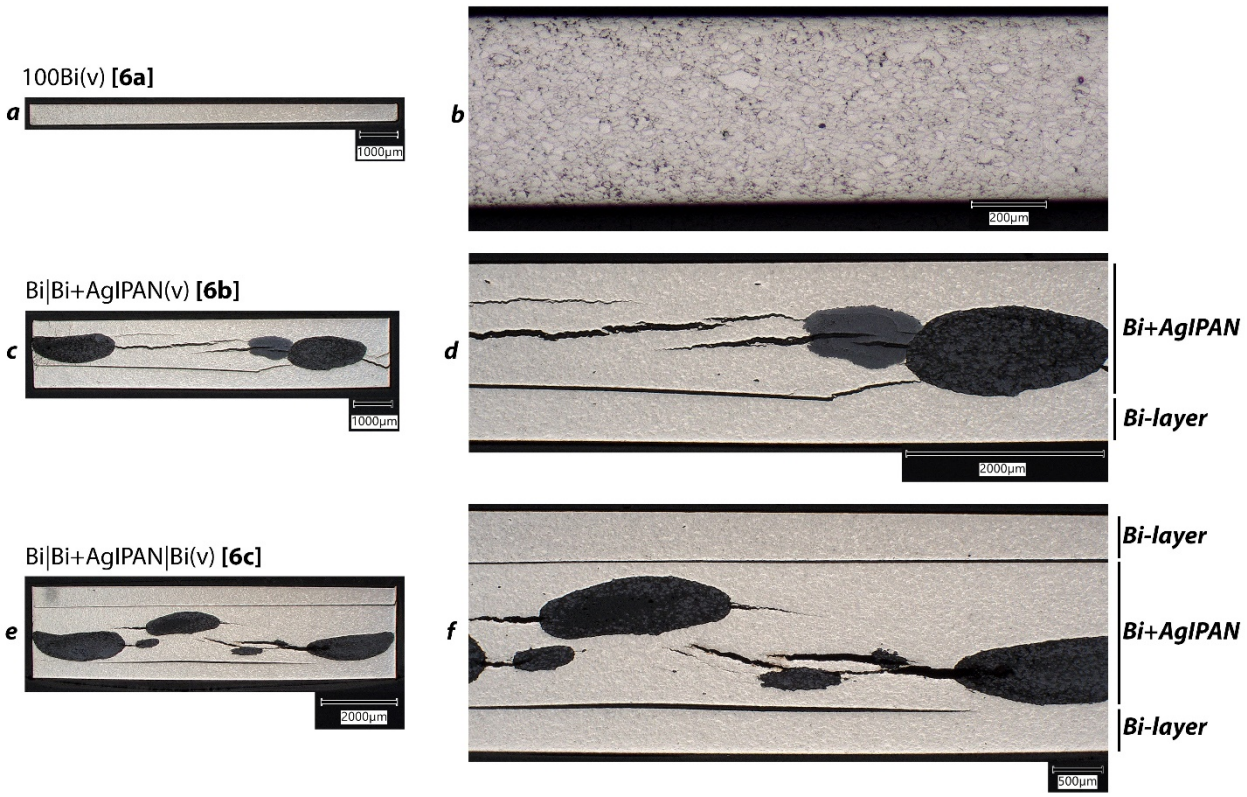

Figure 4-48. Cross-sectional optical micrographs of set-6 pellets including (a,b) 100Bi(v) [6a], (c,d) Bi|Bi+AgIPAN(v) [6b], and Bi|Bi+AgIPAN|Bi(v) [6c] taken at (a,c,e) 20×, (d,f) 50×, and (b) 200× magnifications. These pellets were fired in air at 203°C for 22 h in the vacuum oven.

4.9.1.1 Set-6a Pellet

The Set-6a pellet was fairly uniform in thickness and very similar in appearance to the other $100Bi^0$ pellets discussed previously (i.e., 1a, 2a, 3a) up to this point in the project. It is clear that grain boundaries still exist in the pure Bi^0 pellets. The SEM micrographs are provided in Figure 4-49.

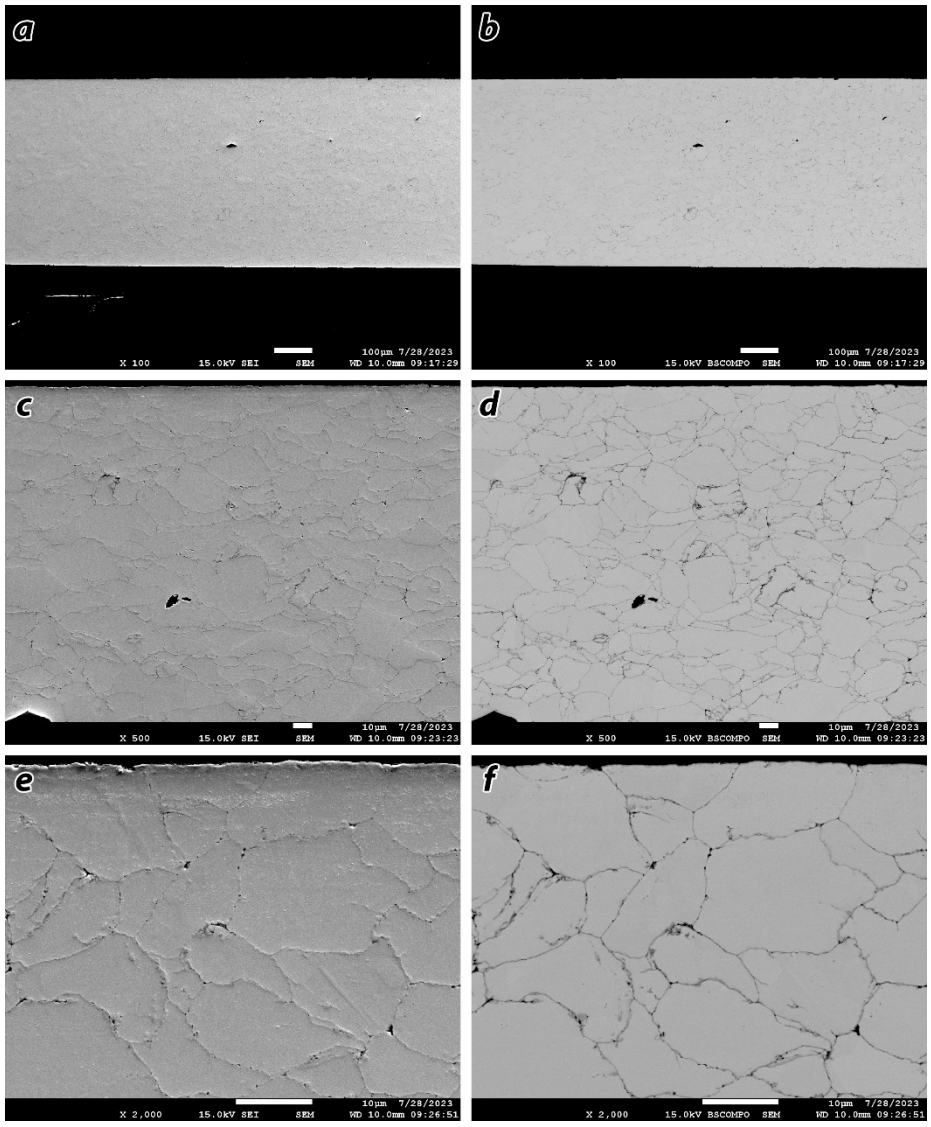

Figure 4-49. SEM including (a,c,e) SEI and (b,d,f) BSE micrographs of Set-6a pellet taken at (a,b) 100×, (c,d) 500×, and (e,f) 2k× magnifications.

4.9.1.2 Set-6b Pellet

The Set-6b pellet is the first example in the project where a polyhalmet was produced and the polymer-containing phase was AgI-PAN. Looking at Figure 4-50 and Figure 4-51, it is clear where the different phases sit in the composite, especially when combined with the EDS data shown in Figure 4-52. The brightest phases in the micrographs in Figure 4-50, Figure 4-51, and Figure 4-52 represent the Bi-metal phase, the darker gray phase is AgI, and the darkest phase is a mixture of epoxy-filled voids and the PAN matrix. It appears that some portions of the AgI-PAN compressed more than other portions and the carbon distribution is uneven throughout the AgI-PAN phase. It is also apparent that cracks exist in the Bi-metal layer that seem to connect to the AgI-PAN beads as well as within the beads. All of these voids could likely be collapsed if hot pressing technique were used for the work.

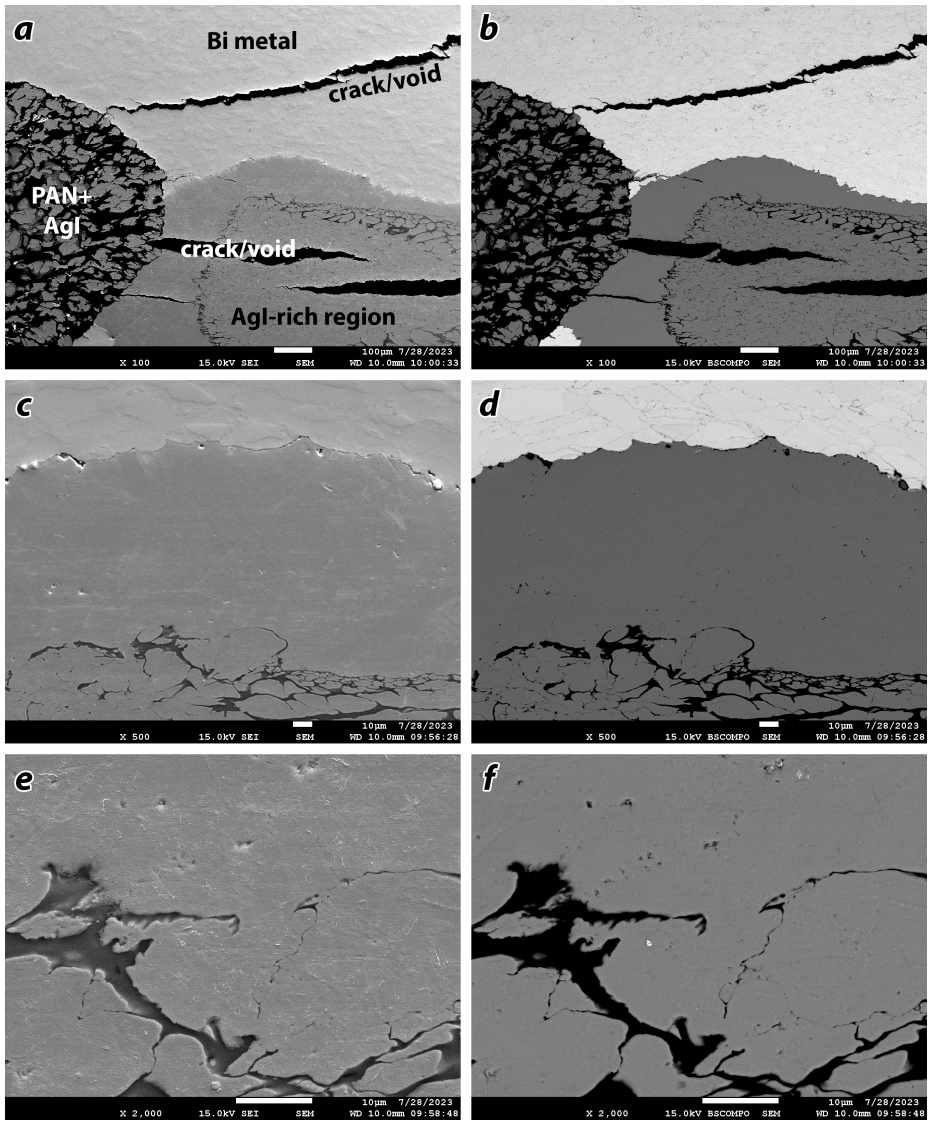

Figure 4-50 SEM including (a,c,e) SEI and (b,d,f) BSE micrographs of the left side of Set-6b pellet taken at (a,b) 100×, (c,d) 500×, and (e,f) 2k× magnifications.

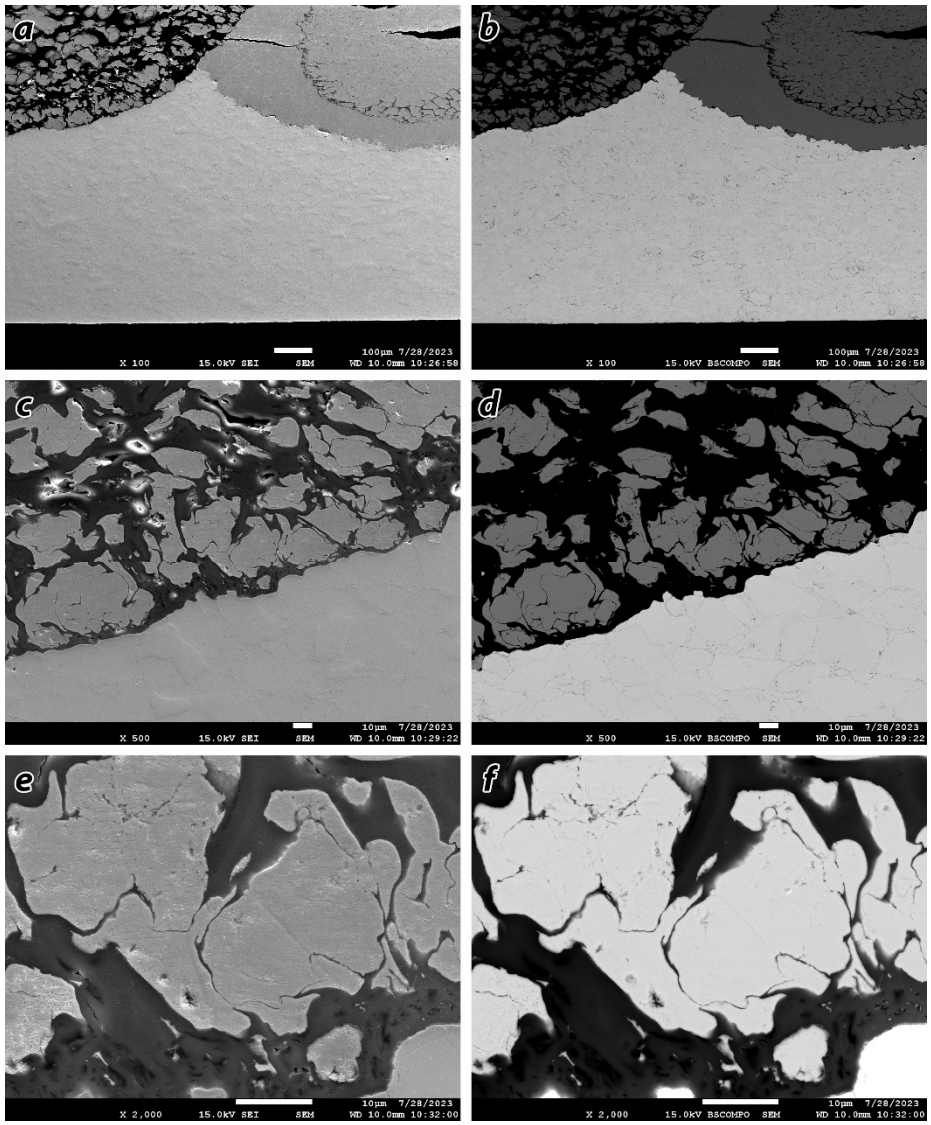

Figure 4-51. SEM including (a,c,e) SEI and (b,d,f) BSE micrographs of the right side of Set-6b pellet taken at (a,b) 100×, (c,d) 500×, and (e,f) 2k× magnifications.

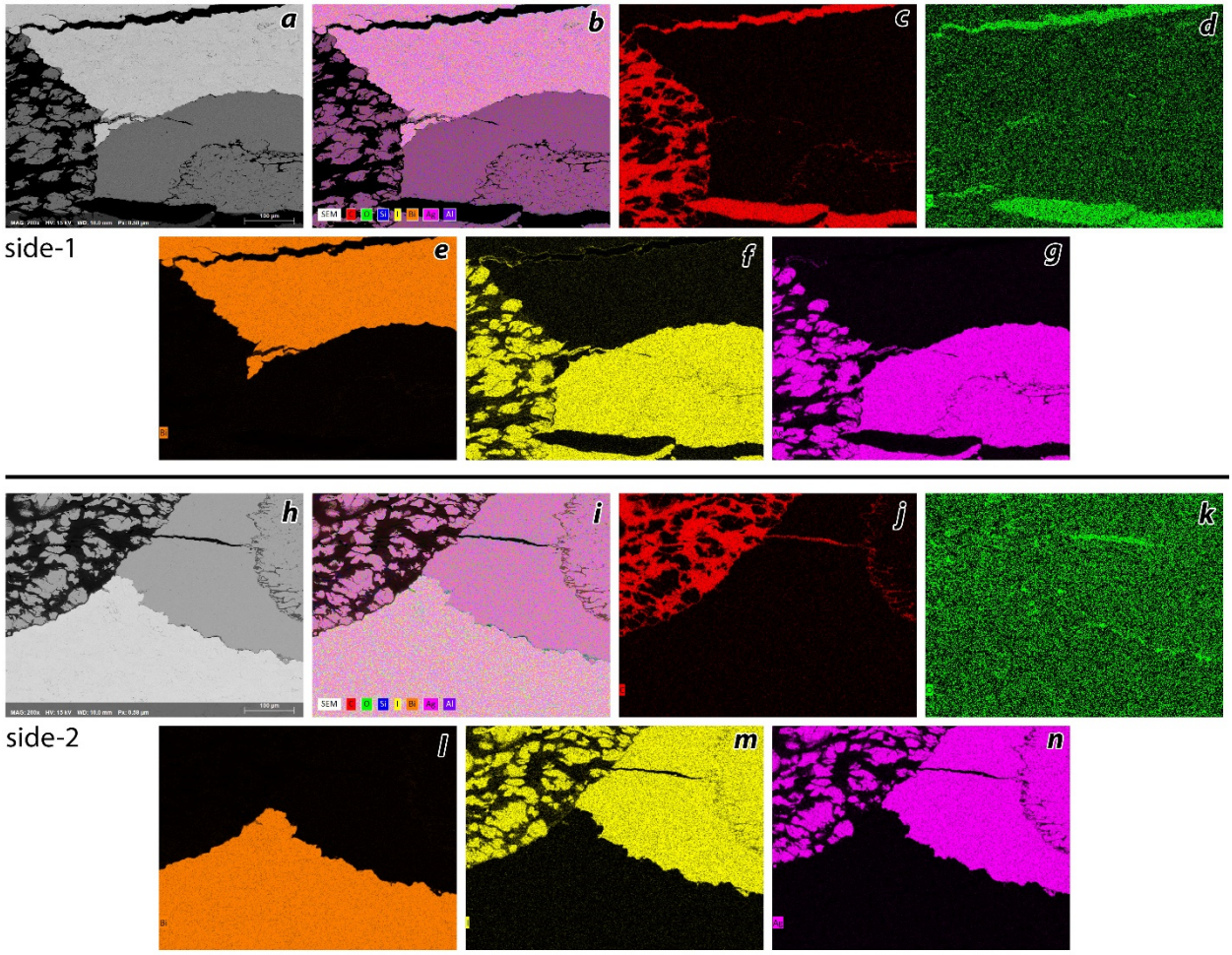

Figure 4-52. EDS dot map of Set-6b pellet on both sides (top, bottom) including (a,h) BSE-SEM micrographs, (b,i) the overlays, (c,j) the C-maps, (d,k) the O-maps, (e,l) the Bi-maps, (f,m) the I-maps, and (g,n) the Ag-maps.

4.9.1.3 Set-6c Pellet

The Set-6c pellet is the first example in the project where a polyhalmet was produced with two Bi-layers on top and bottom. Looking at Figure 4-53 and Figure 4-54, it is clear where the different phases sit in the composite, especially when combined with the EDS data shown in Figure 4-55. The brightest phases in the micrographs in Figure 4-53, Figure 4-54, and Figure 4-55 represent the Bi-metal phase, the darker gray phase is AgI, and the darkest phase is a mixture of epoxy-filled voids and the PAN matrix. It appears that some portions of the AgI-PAN compressed more than other portions and the carbon distribution is uneven throughout the AgI-PAN phase. It is also apparent that cracks exist in the Bi-metal layer that seem to connect to the AgI-PAN beads as well as within the beads; this is also seen very evidently in Figure 4-48e,f. Based on these visual observations, it is readily apparent that pressing the individual layers separately probably leads to less adhesion once the pellet is fired. To prevent these gaps and to improve adhesion between layers, a lower pressing pressure could be used to form the intermediate layers followed by a final high-pressure press of the full composite form. Another option that would likely work even better would be to use a hot-pressing technique where the voids could be evacuated (pulling a vacuum) prior to the pressing step such as using HIP.

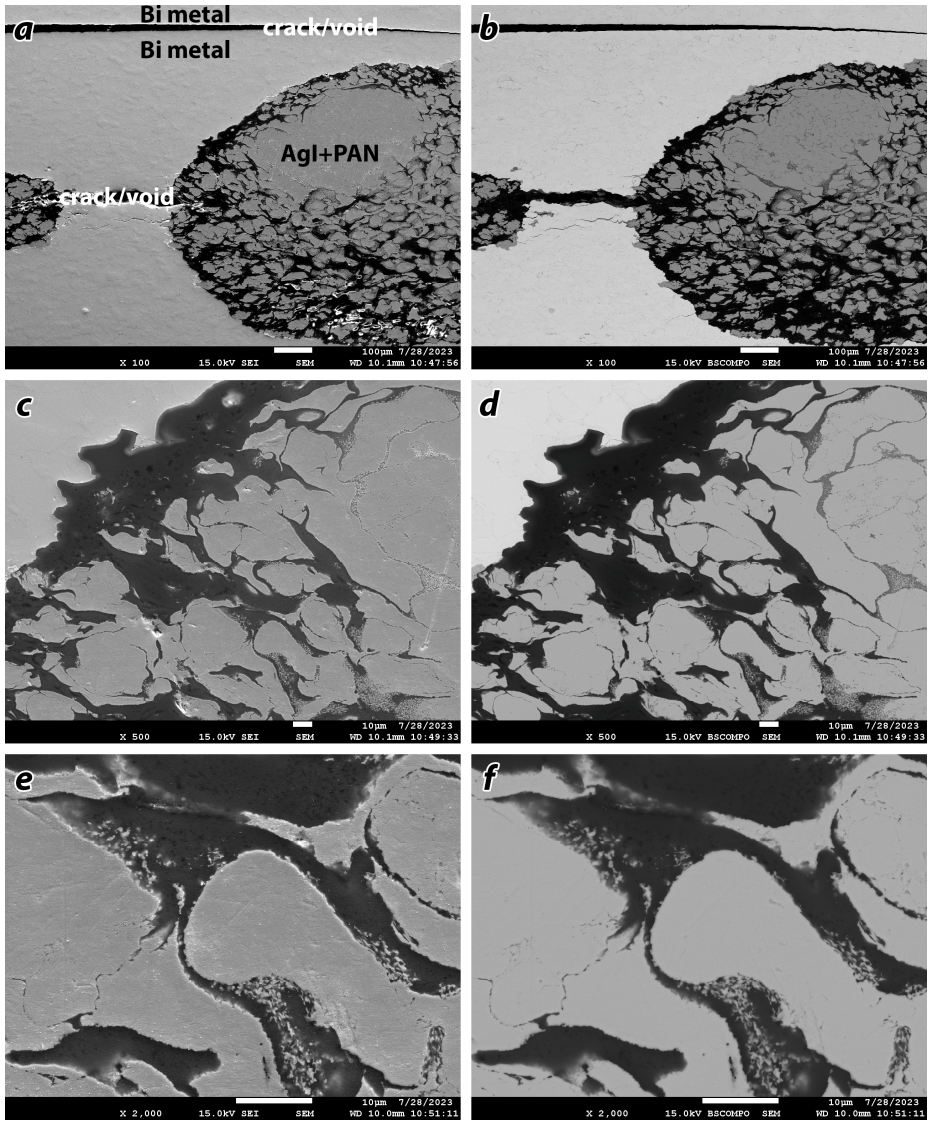

Figure 4-53. SEM including (a,c,e) SEI and (b,d,f) BSE micrographs of the left side of Set-6c pellet taken at (a,b) 100×, (c,d) 500×, and (e,f) 2k× magnifications.

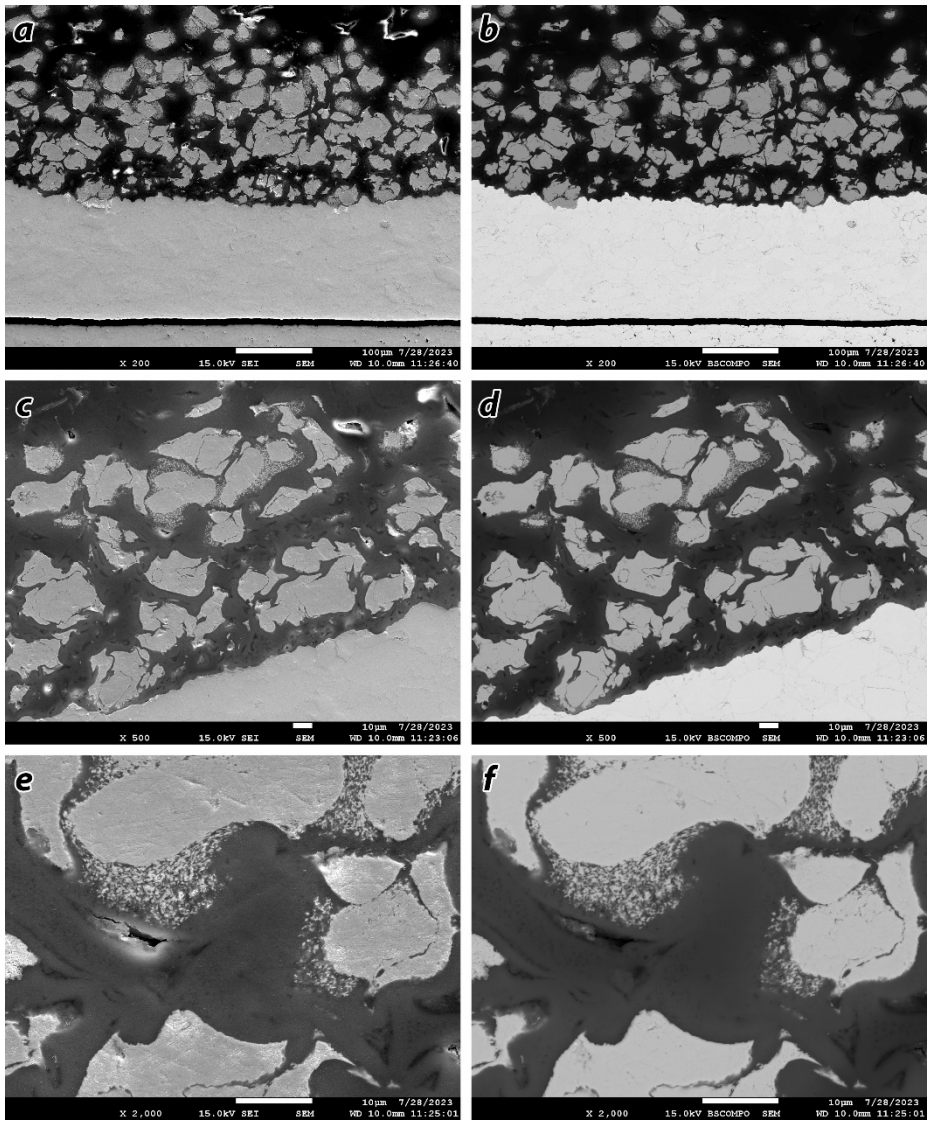

Figure 4-54. SEM including (a,c,e) SEI and (b,d,f) BSE micrographs of the right side of Set-6c pellet taken at (a,b) 200×, (c,d) 500×, and (e,f) 2k× magnifications.

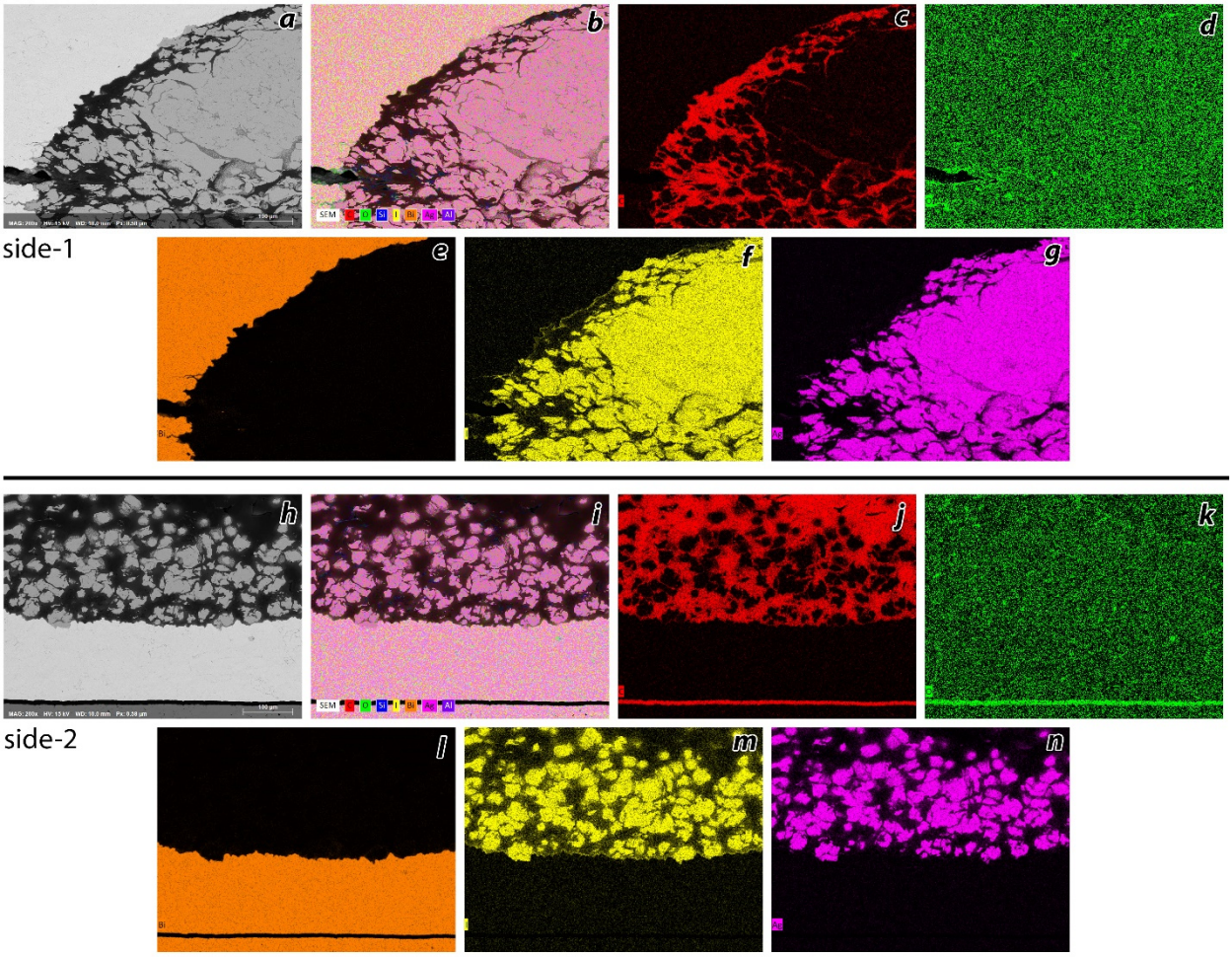

Figure 4-55. EDS dot map of Set-6c pellet on both sides (top, bottom) including (a,h) BSE-SEM micrographs, (b,i) the overlays, (c,j) the C-maps, (d,k) the O-maps, (e,l) the Bi-maps, (f,m) the I-maps, and (g,n) the Ag-maps.

4.9.2 Grinding the Samples before Pelletization (Set-7)

The Set-7 pellets include a few different pure Bi^0 pellets of different target thicknesses of 0.5 mm (7a), 0.4 mm (7b), and 0.3 mm (7c). Also, two three-phase pellets were made including one made with 75Cu-PAN[(a)] loaded with iodine [i.e., CuI-PAN[(150)]; see sample I-2c in Table 4-3] and one made with AgX[(b)] loaded with iodine [i.e., AgIX[(150)]; see I-2a in Table 4-3]. The two three-phase pellets were made using the sandwich approach outlined in see Figure 3-4c.

Pictures of all Set-7 pellets are shown in Figure 4-56 after heat treatment under vacuum and the data from the pellets is provided in Table 4-10. From the appearances of the sintered samples (Figure 4-56), it is clear that some oxidation occurred to the metal before sintering, to the sample (or just the metal phase) during sintering, or perhaps both. It also appeared that the Bi^0 in the container from American Elements was oxidizing based on a reddish (rosy) color visually present on the particles. This means that pellet pressing might be complete with this metal unless a method can be employed to reduce it back to metal without changing the other properties (i.e., the particle size, purity, and bulk density). Based on information for Bi^0 oxidation found in the literature (Sanderson 2023), it was expected that surface oxidation would not occur at room temperature in air, or it would have been stored in a vacuum desiccator.

Table 4-10. Summary of data from Set-7 pellets.

Pellet Number:	7a	7b	7c	7d	7e
Alternative ID	100Bi	100Bi	100Bi	Bi-CuIPAN-Bi	Bi-AgIX-Bi
Date	6/21/2023	6/21/2023	6/21/2023	6/21/2023	6/21/2023
Iodine loading (source)	–	–	–	I-2c in Table 4-3	I-2a in Table 4-3
Phase-a (composition)	Bi	Bi	Bi	Bi	Bi
Phase-b (composition)	–	–	–	CuI-PAN[150]	AgX+I[150]
Phase-c (composition)	–	–	–	Bi	Bi
Phase-d (composition)	–	–	–	Bi	Bi
Phase-a (mass, g)	0.3842	0.3072	0.2308	0.2310	0.2303
Phase-b (mass, g)	–	–	–	0.1889	0.2064
Phase-c (mass, g)	–	–	–	0.4125	0.4154
Phase-d (mass, g)	–	–	–	0.2312	0.2309
C%m (MI_x, m%)	0.00%	0.00%	0.00%	95.43%	68.73%
mf_i mass fract.	0.00%	0.00%	0.00%	58.84%	23.50%
$t_{p,g}$ (mm)	0.530	0.465	0.357	2.160	1.930
$m_{p,g}$ (g)	0.3770	0.3011	0.2257	1.0483	1.0653
Atmosphere type	Vac	Vac	Vac	Vac	Vac
T_{ht} (°C)	203	203	203	203	203
t_{ht} (h)	20	20	20	20	20
Ramp (°C/min)	–	–	–	–	–
$t_{p,f}$ (mm)	0.557	0.480	0.370	2.147	1.927
$m_{p,f}$ (g)	0.3787	0.3017	0.2259	1.0472	1.0671
Δm (m%)	0.45%	0.20%	0.09%	-0.10%	0.17%
ρ_b (g/cm^3)	8.6618	8.0028	7.7736	6.2112	7.0519
$\rho_{b,em}$ (g/cm^3)	9.7828	9.7828	9.7828	9.7828	9.7828
$\rho_{b,MIx}$ (g/cm^3)	–	–	–	5.67	5.68
$WL_{I,m}$ (m%)	–	–	–	10.45%	4.48%
V_{MIx}/m_{LS} (cm^3/g)	0.1479	0.1479	0.1479	0.1479	0.1479
V_{tot}/m_{LS} (cm^3/g)	0.2654	0.2654	0.2654	0.2654	0.2654
$WL_{MI,v}$ (vol%)	–	–	–	23.81%	25.41%
$V_{\%T}$ (vol%)	113.5%	122.5%	126.0%	120.8%	104.8%

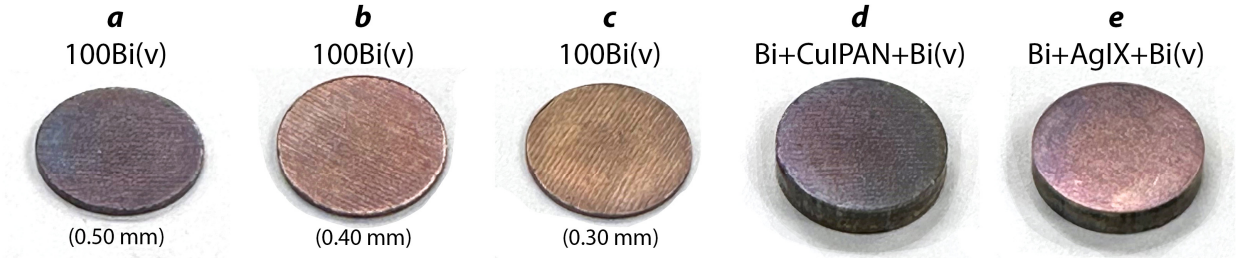

Figure 4-56. Pictures of the Set-7 pellets after heat treatments including (a) 7a, (b) 7b, (c) 7c, (d) 7d, and (e) 7e. All pellets are 1-cm in diameter.

Optical micrographs of the set-7 samples are provided in Figure 4-57. The goal with pellets 7a, 7b, and 7c was to evaluate options for making top and bottom layers for the pellet "sandwich" (see Figure 3-3e and Figure 3-4c). The target was the smallest pellet that could be pressed while maintaining a uniform pellet thickness. The 0.3 mm pellet (7c) showed fairly uniform thicknesses

(see Figure 4-57e,f) so these Bi^0 masses were used for the top and bottom layers for pellets 7d and 7e.

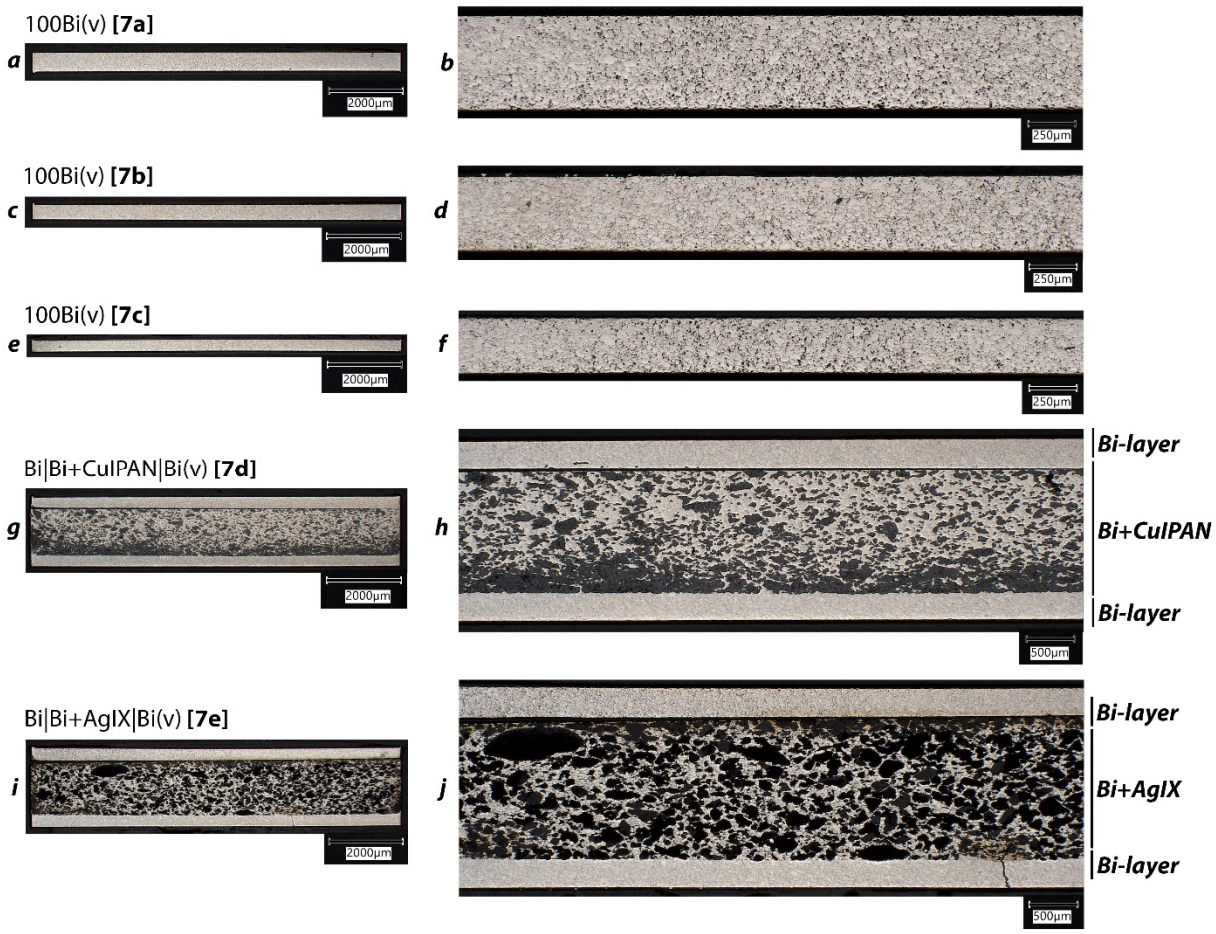

Figure 4-57. Cross-sectional optical micrographs of set-7 pellets including (a,b) 100Bi(v) [7a], (c,d) 100Bi(v) [7b], (e,f) 100Bi(v) [7c], (g,h) Bi|Bi+CuIPAN|Bi(v) [7d], and (i,j) Bi|Bi+AgIX|Bi(v) [7e] taken at (a,c,e,g,i) 20×, (d,f) 50×, and (b) 200× magnifications. These pellets were fired in under vacuum at 203°C for 20 h in the vacuum oven.

4.9.2.1 Set-7a, Set-7b, and Set-7c Pellets

SEM micrographs for Set-7a, Set-7b, and Set-7c pellets comprised of pure Bi^0 at different target thicknesses are provided in Figure 4-58, Figure 4-59, and Figure 4-60, respectively. The thicknesses measured using Adobe Photoshop on the 100× SEM micrographs are provided in Table 4-11 and align well with the target values. The pellets all look uniform and contain small pockets and voids throughout with noticeable grain boundaries. Higher firing temperatures would likely result in better particle-particle sintering.

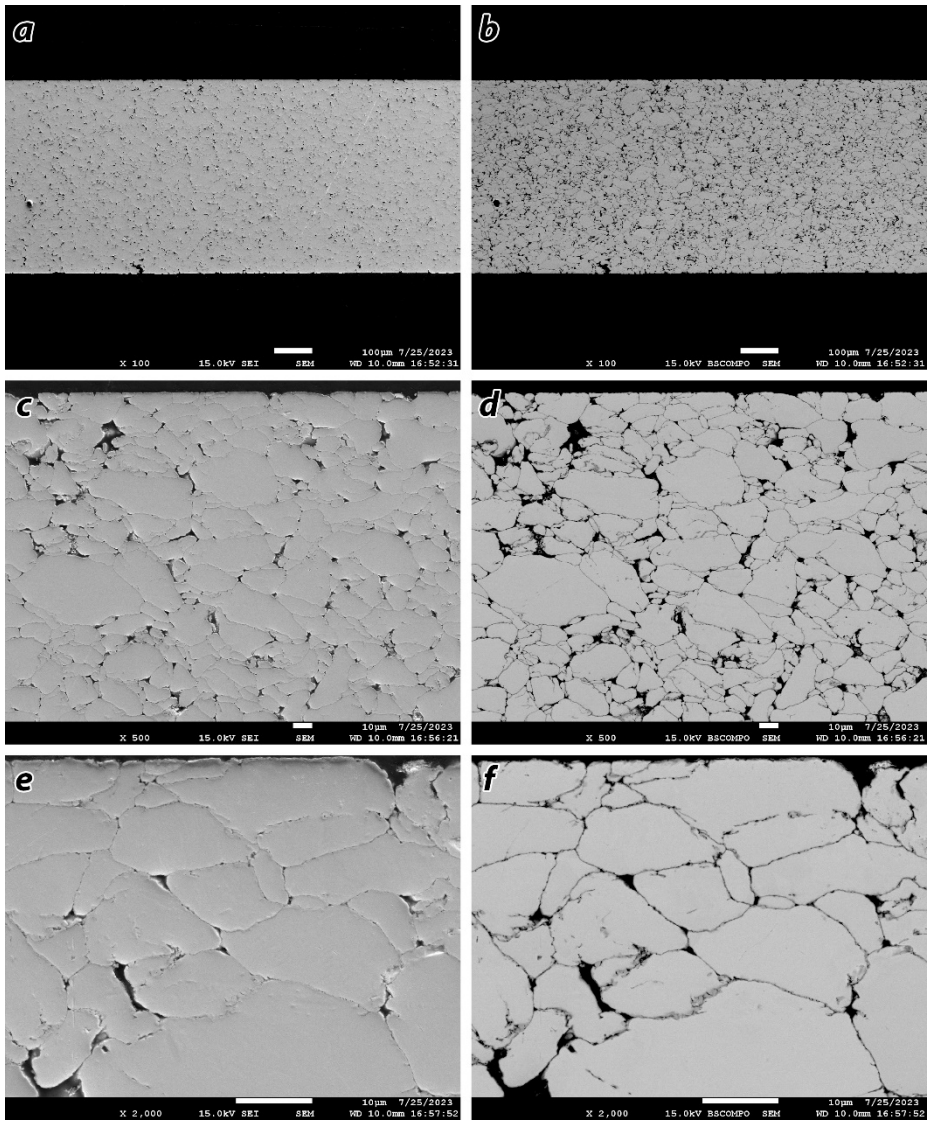

Figure 4-58. SEM including (a,c,e) SEI and (b,d,f) BSE micrographs of Set-7a pellet taken at (a,b) 100×, (c,d) 500×, and (e,f) 2k× magnifications.

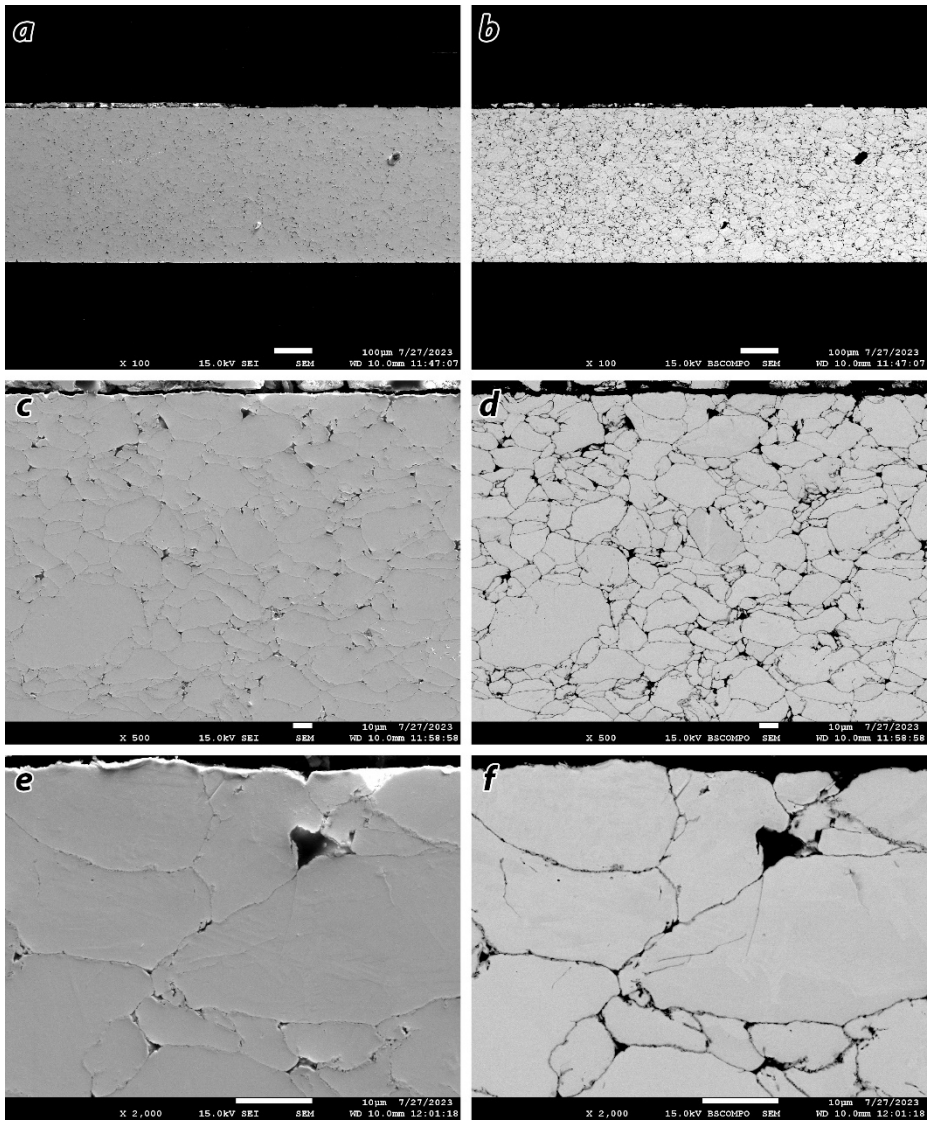

Figure 4-59. SEM including (a,c,e) SEI and (b,d,f) BSE micrographs of Set-7b pellet taken at (a,b) 100×, (c,d) 500×, and (e,f) 2k× magnifications.

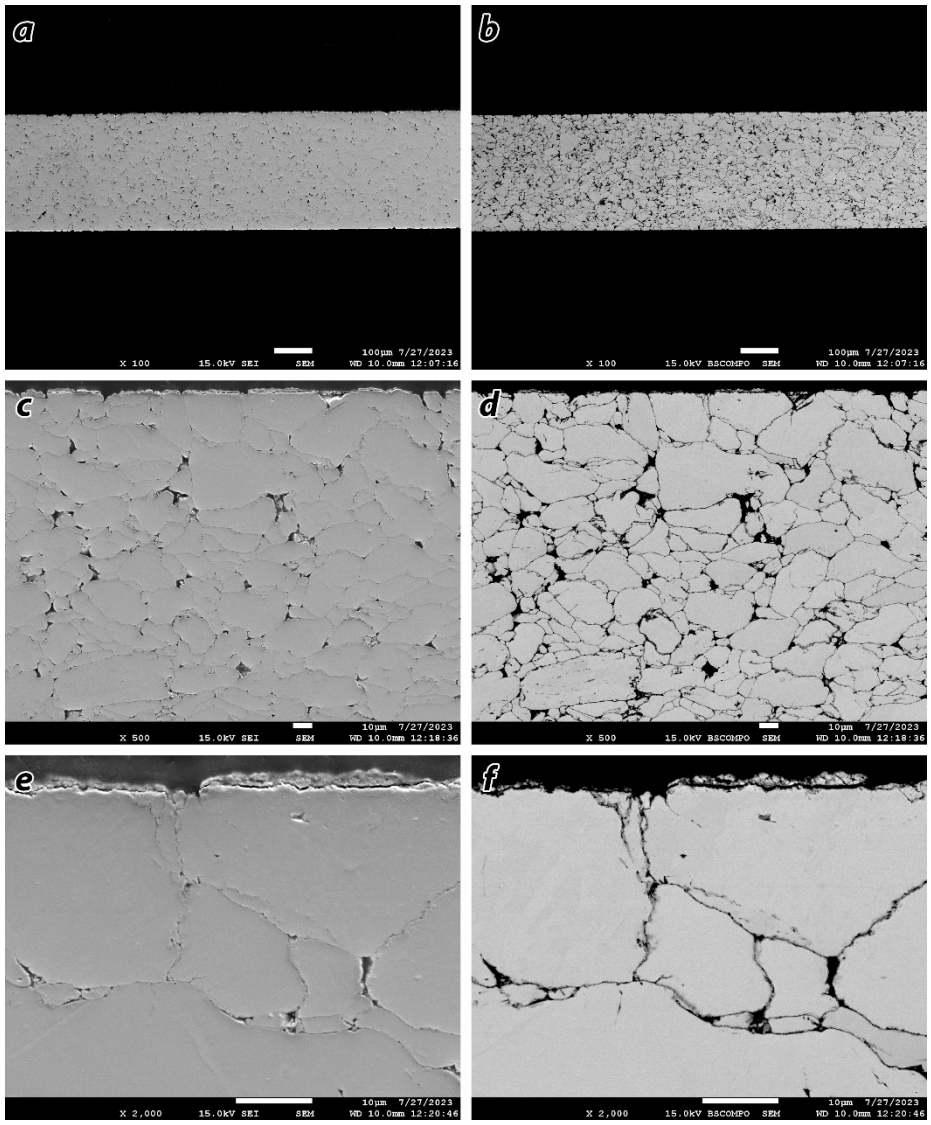

Figure 4-60. SEM including (a,c,e) SEI and (b,d,f) BSE micrographs of Set-7c pellet taken at (a,b) 100×, (c,d) 500×, and (e,f) 2k× magnifications.

Table 4-11. Summary of fired pellet thicknesses ($t_{p,f}$; in mm) for pure Bi^0 pellets Set-7a, Set-7b, and Set-7c measured using the measurement tool in Adobe Photoshop on the 100× SEM micrographs with target values of 0.5 mm, 0.4 mm, and 0.3 mm respectively.

Sample	Target (mm)	$t_{p,f}$ (mm)	Reference
Set-7a	0.5	0.507	Figure 4-58b
Set-7b	0.4	0.407	Figure 4-59b
Set-7c	0.3	0.308	Figure 4-60b

4.9.2.2 Set-7d Pellet

The Set-7d pellet was the first attempt at incorporating iodine-loaded PAN-based materials into a metal composite where the PAN beads were ground to a finer particle size prior to pelletization. The SEM micrographs for this sample are provided in Figure 4-61 and Figure 4-62. It is clear that some void spaces still exist around the PAN composites (darker phase) where the Bi^0 phase was not successful at fully closing the porosity around the pellets, but some of this carbon could also be PAN that was pushed out of the pellets towards the boundary between the CuI crystals and the Bi^0 encapsulant phase. It is likely that these pores could be closed if a hot-pressing technique were applied. An EDS dot map for this pellet is provided in Figure 4-63 where elemental distributions are clearly seen between the Bi^0 phase and the CuI-PAN phase. The C-map shows the void spaces (epoxy filled) as well as the PAN matrix and the CuI phase. Also, the adhesion was not the same between the bottom and top Bi-metal layers; one side adhered nicely to the middle layer.

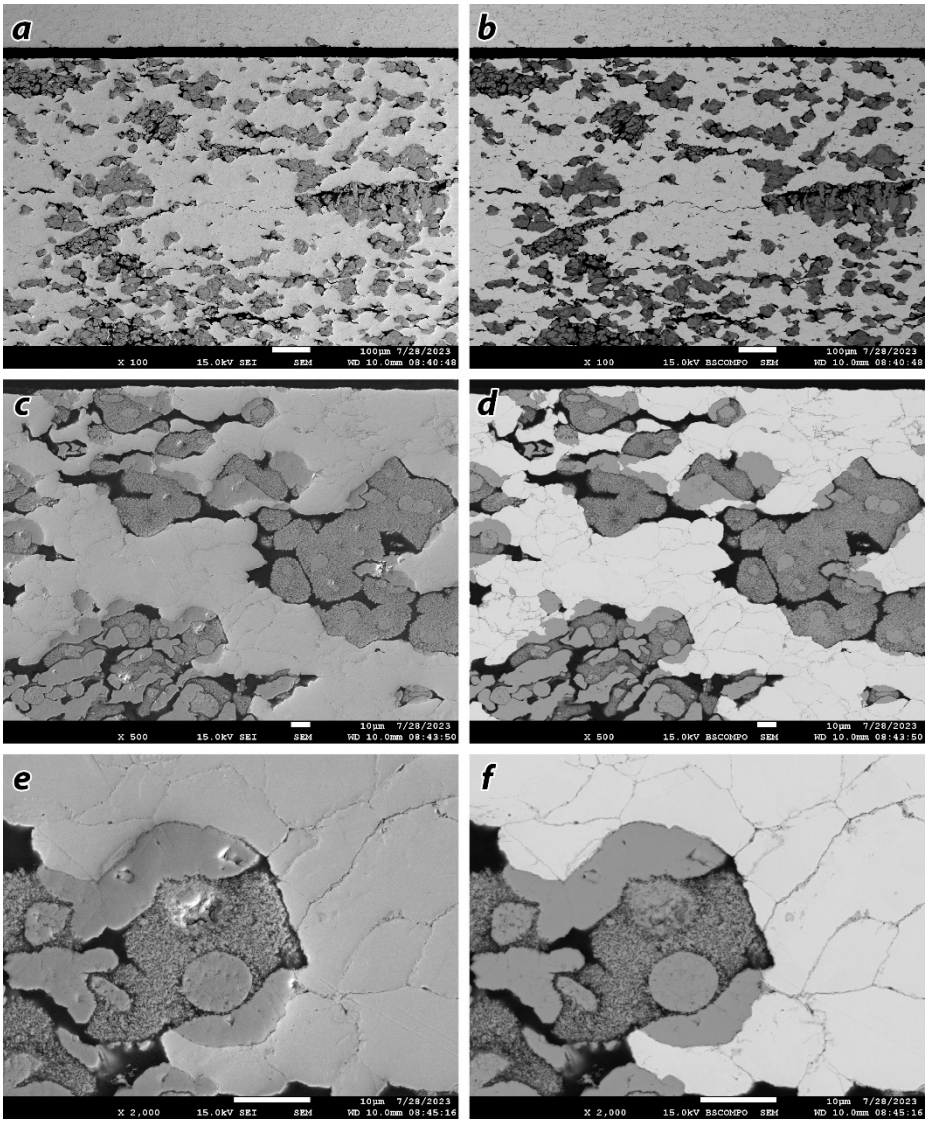

Figure 4-61. SEM including (a,c,e) SEI and (b,d,f) BSE micrographs of the left side of Set-7d pellet taken at (a,b) 100×, (c,d) 500×, and (e,f) 2k× magnifications.

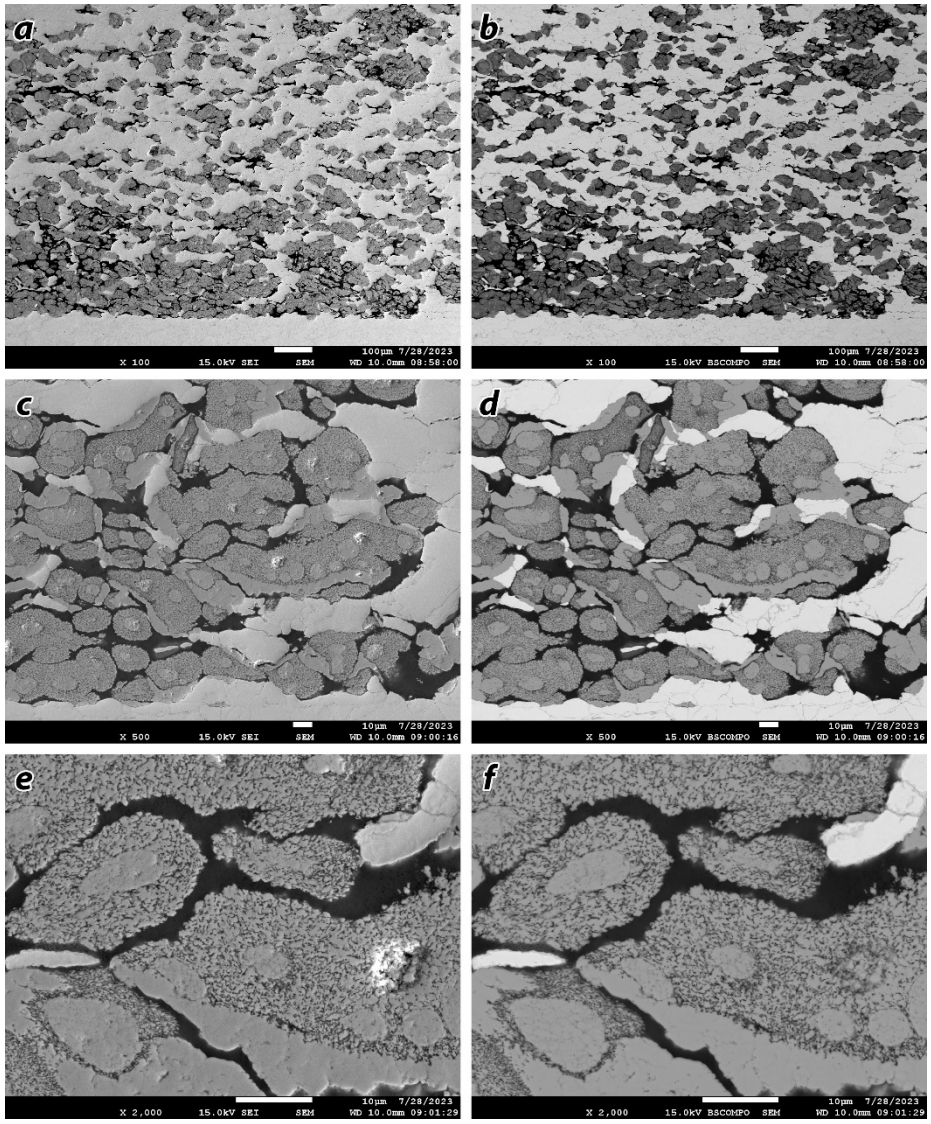

Figure 4-62. SEM including (a,c,e) SEI and (b,d,f) BSE micrographs of the right side of Set-7d pellet taken at (a,b) 100×, (c,d) 500×, and (e,f) 2k× magnifications.

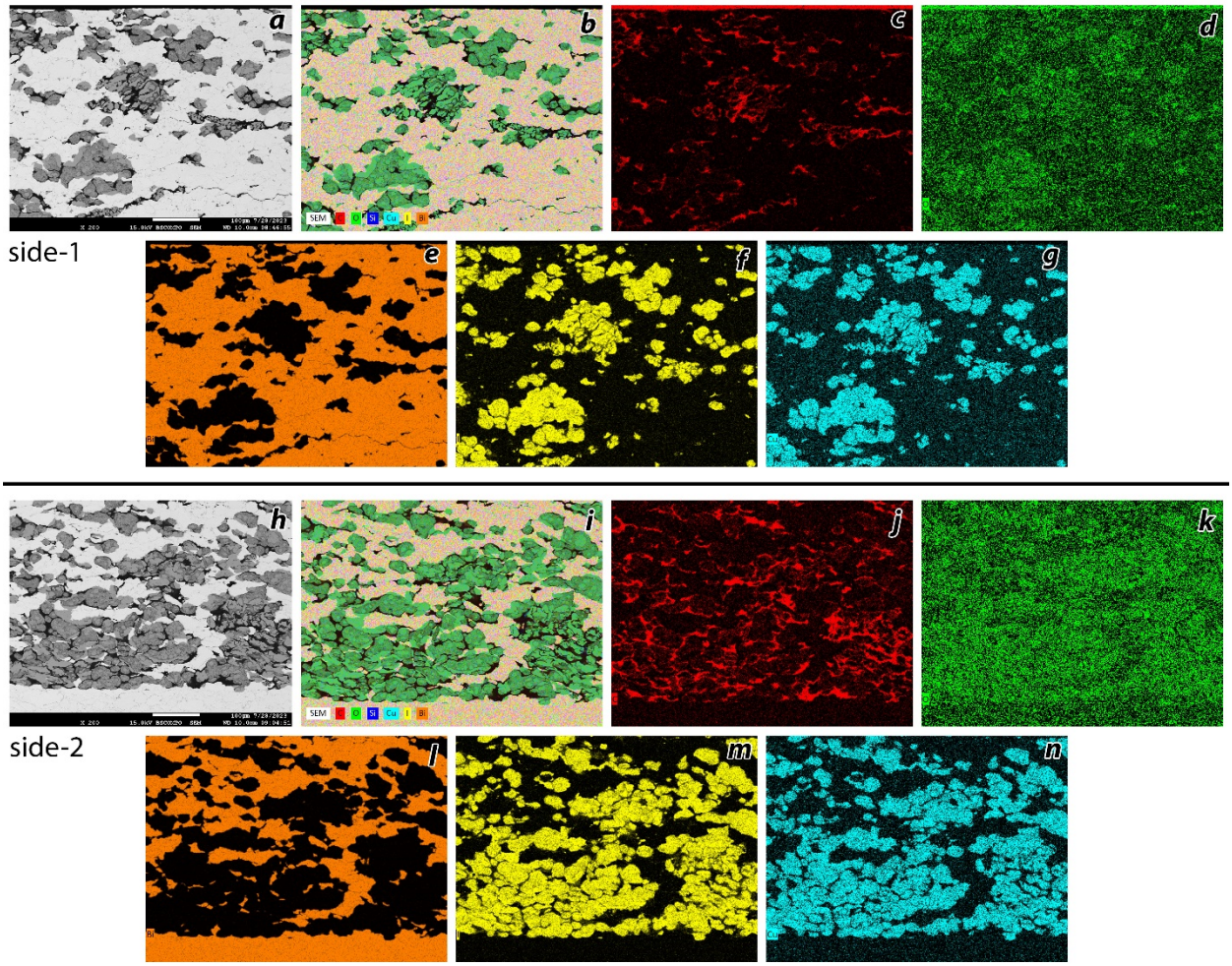

Figure 4-63. EDS dot maps for Set-7d pellet in two regions.

4.9.2.3 Set-7e Pellet

The Set-7e pellet was the first attempt at incorporating iodine-loaded IONEX Ag-400 silver faujasite into a metal composite; the AgIX beads were ground to a finer particle size prior to pelletization. The SEM micrographs for this sample are provided in Figure 4-64 and Figure 4-65. It is clear that some small void spaces still exist around the faujasite particles and agglomerates that could possibly be closed more effectively if a hot-pressing technique were applied. An EDS dot map for this pellet is provided in Figure 4-66 where elemental distributions are clearly seen between the Bi^0 phase and the AgI-containing faujasite (i.e., Ag, I, Al, Si, O). The C-map shows the void spaces (epoxy filled) as well as the PAN matrix.

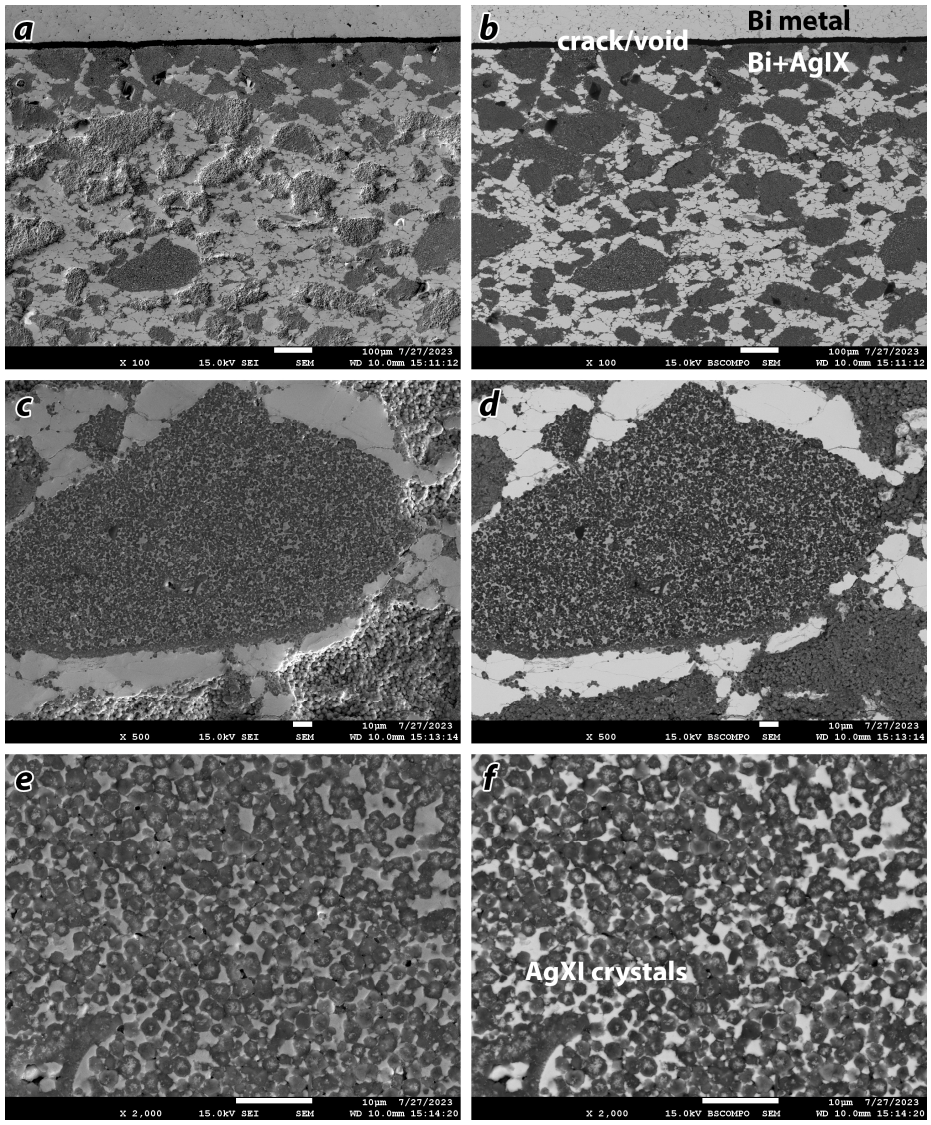

Figure 4-64. SEM including (a,c,e) SEI and (b,d,f) BSE micrographs of the left side of Set-7e pellet taken at (a,b) 100×, (c,d) 500×, and (e,f) 2k× magnifications.

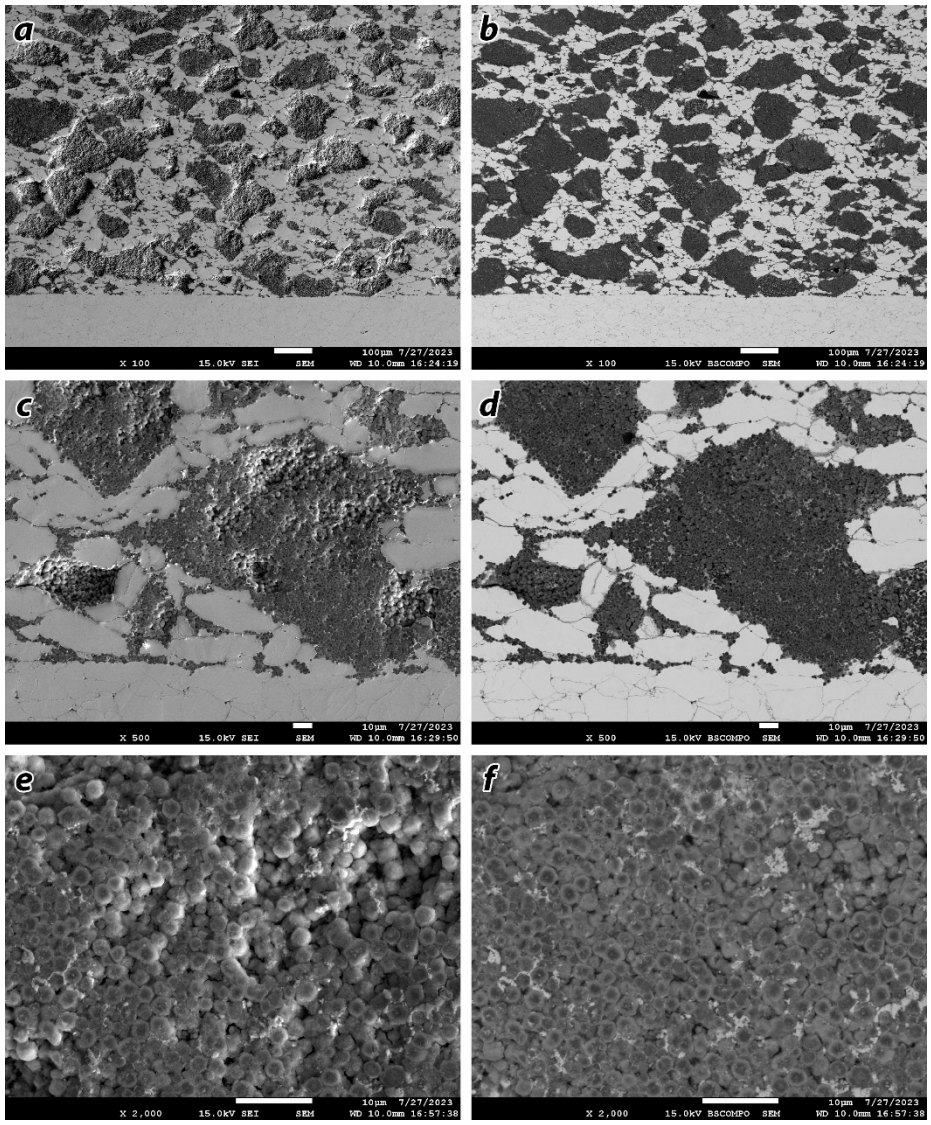

Figure 4-65. SEM including (a,c,e) SEI and (b,d,f) BSE micrographs of the right side of Set-7e pellet taken at (a,b) 100×, (c,d) 500×, and (e,f) 2k× magnifications.

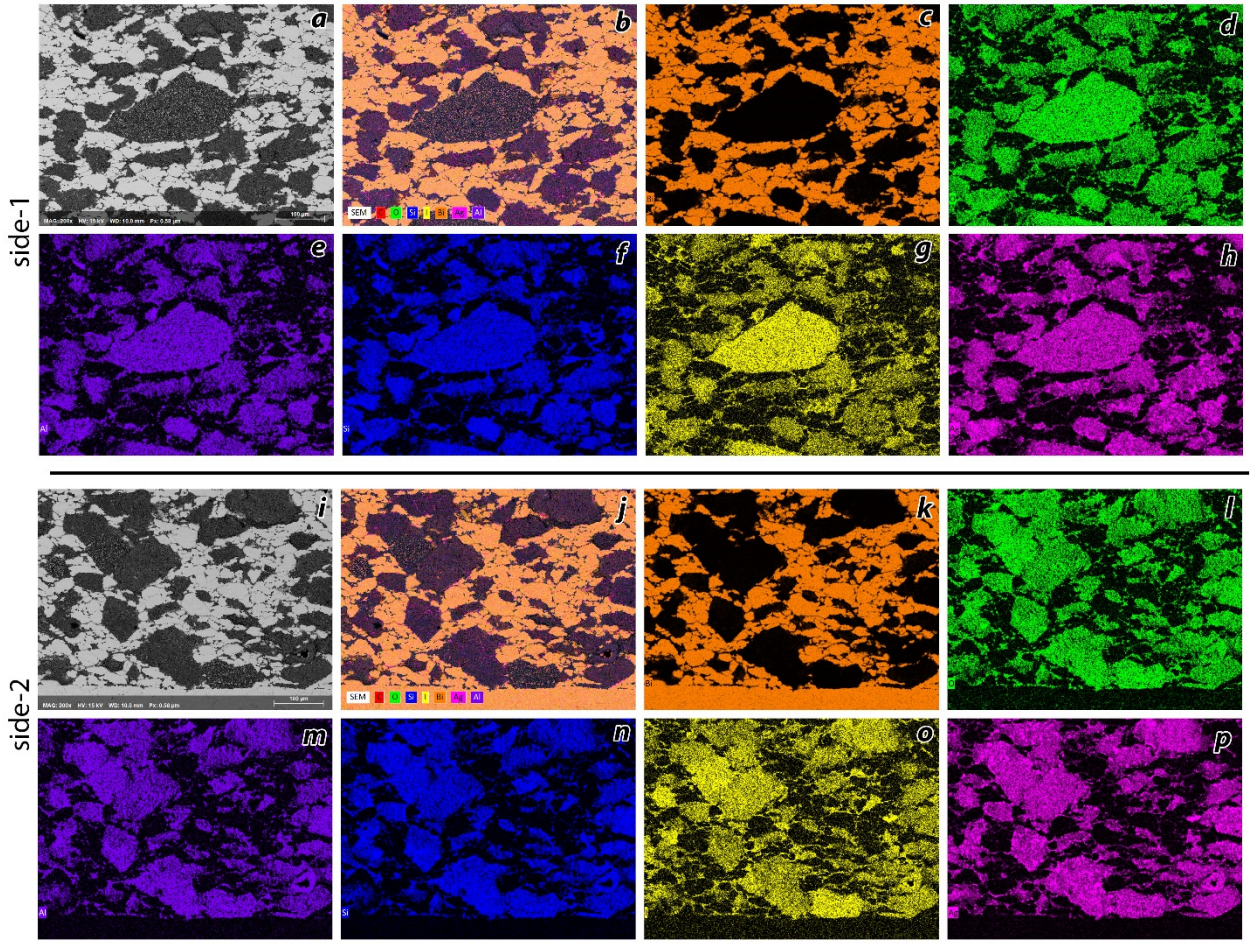

Figure 4-66. EDS dot maps for Set-7e pellet in two regions.

5.0 Summary, Conclusions, and Recommendations

This report covers experimental data collected and analyzed to understand the production of and efficacy of metal-encapsulation processes for immobilizing halides (halmets), ceramics (cermets), and halide-containing polymer composites (polyhalmets) using different halides (i.e., AgI, CuI), filler materials (i.e., polymers, zeolites), metals (i.e., Bi, Sn, Bi-Sn), temperatures, times, atmospheres, and pellet thicknesses. After each pellet was produced, they were mounted in resin and cross-section polished so that the phase distribution, elemental distribution, and microstructures could be studied across the full thickness of the pellet. During this study, a total of 18 pellets were produced with a general summary provided in Table 5-1 below.

Table 5-1. Summary of pellets produced within this project lifecycle including the sample set, the number of pellets produced in each set, the metal encapsulant used, other phases present within the set of samples produced for that set, the target metal-iodide complex (MI_x), and the atmosphere (atm) used in the heat treatment process.

Set	Pellets	Metal	Other(s)	Target MI_x	Atm
1	1	Bi	–	–	Air
2	3	Bi	Al_2O_3	–	Air
3	3	Bi	AgI	AgI	Vac
4	1	Bi	CuI	CuI	Vac
5	2	Bi-Sn	AgI, CuI	AgI, CuI	Air
6	3	Bi	AgI-PAN$^{(150)}$	AgI	Vac
7	5	Bi	CuI-PAN$^{(150)}$, AgIX$^{(150)}$	AgI, CuI	Vac

While the initial approach of using Al_2O_3 as a surrogate (i.e., pellets **2b** and **2c**) did not allow for pelletization of dense monoliths, this process worked well for pure metal iodides (MI_x) where low-porosity pellets were achieved using single-press pellets (i.e., pellets **3b**, **3c**, **4a**, **5a**, and **5b**). For pelletization of three-phase pellets containing a metal-iodide along with either a polymer phase (i.e., pellets **6b**, **6c**, **7d**) or aluminosilicate (decomposed zeolite) phase (i.e., pellet **7e**). All other pellets produced (i.e., pellets **1**, **2a**, **3a**, **6a**, **7a**, **7b**, and **7c**) were made of pure metal at different thicknesses and run with the samples as "standards" so that all samples were subject to the same conditions. It was also an internal "standard" for each set to see how the encapsulant metals behaved over time. For example, the Bi^0 was observed to oxidize more and more readily over the course of the project showing that this metal has a shelf life (with storage in air) before it starts to oxidize at room temperature. For the Set-6 and Set-7 pellets, a multi-layer approach was used with different pressings prior to pellet removal from the die. The aim of this was to create barrier layers below and above the middle iodine-containing layer. Also, additional fill metal was added to the middle layer to fill in void spaces around the MI_x-containing phase in between the pure metal layers; in these cases, the same metal was used in all metal layers.

In general, the pelletization processes applied within the context of this work was successful at collapsing multi-phase mixtures into low-porosity monoliths prior to sintering. While some pellets, such as the set-7 pellets, did show evidence of oxidation during the sintering process, overall, this CPS pelletization protocol worked pretty well. Higher temperatures are likely needed to fully sinter the inter-dispersed metallic particles between the secondary and tertiary phases present in the multi-phase pellets so this should be studied in the future. However, it is more than likely that hot isostatic pressing would be a far better approach to fully densify these materials as it can be done under a vacuum to prevent oxidation as well as allowing for full void collapse without the need to displace gas-containing void spaces.

The primary conclusion is that the CPS process can be used to make pellets quick and easy for screening processes. It remains unclear from this study how these pellets and their properties (e.g., mechanical integrity) resemble those of pellets of similar compositions produced using hot-pressing processes like HUP (including SPS) or HIP as that was outside the scope of this project; however, this should be evaluated in a future study.

The primary conclusions drawn from this work summarized below:

- The PAN composite production process is extremely flexible for producing beads of predictable sizes and shapes using a variety of active gettering materials including metals (i.e., Ag^0, Bi^0, Cu^0) and sulfides (i.e., Ag_2S, Bi_2S_3, Cu_2S) at different loading levels of getter (i.e., 75–90 mass%).

- The PAN composite production process often creates beads with tails on them (see Figure 4-4 for examples of these). Removing these tails is fairly easy to do while they are wet, but difficult once the pellets are dry due to the static nature of the resulting materials. Thus, the tails tend to statically adhere to the beads. Using an antistatic device did not change this issue.

- Effective DMSO removal from the DIW-DMSO mixture during PAN composite bead synthesis will require implementation of a new type of bead support system with a pathway for solution removal. This would require a mesh-type support for the beads to sit on top of within the mixing vessel whereby the DMSO-rich portion of the mixture separates to the bottom of the vessel and can be selectively pipetted out into a waste container while leaving the beads intact (see Figure 4-6).

- Several aspects of the metal encapsulant portion of the work could use improvement. The metals utilized in this work will need optimization before high-quality pellets can be realized using the approaches discussed herein. The inherent oxidation-prone properties of these less-noble metals suggest that non-oxidized metallic encapsulants need to be used to help prevent with issues with particle-particle sintering during firing. A study should also be performed for each metal encapsulant to find the optimal firing temperature prior to producing pellets; this was not done in the current work due to funding and time constraints. Also, other promising metal encapsulants should be explored, e.g., the 55.5Bi-44.5Pb eutectic not obtained for this work. While Pb^0 is environmentally toxic and disposal is restricted under the RCRA (EPA 1980) (see Section 2.6), the high stability of PbI_2 (Table 2-2) makes it an attractive long-term storage option for radioiodine.

- The concept of loading a PAN composite with iodine and subsequently removing the PAN phase through DMSO dissolution proved successful for AgI-based materials, somewhat successful for BiI_xO_y-based materials, and not successful for CuI-based materials. This additional step, while adding another liquid waste stream to the process, will greatly simplify down-stream consolidation processes for waste form production (i.e., hot pressing) and remove the low-density polymer phase that will add unwanted volume to the final composite form.

Additional ideas and experiments that should be pursued in the event that this work was to be continued are summarized below:

- One of the project goals in the original plan was to evaluate the sizes of PAN beads using different orifice (pipette tip) diameters and different solution temperatures. To initiate this

line of inquiry, SEM was performed on different pipette tips to get accurate orifice diameter measurements and DMSO-PAN viscosity measurements at different temperatures (i.e., 25°C–70°C). The reason that this was not completed was due to the difficultly in figuring out how to properly heat the DMSO-PAN mixture with active getters added to these mixtures and transferring that mixture to a pipette tip for dropping into the agitated DIW dish (Figure 3-1c) without the mixture cooling.

- For scaling up these types of procedures and producing smaller beads sizes, previous work on bead production for other processes can be utilized. This includes continuous-type production processes like those documented by PNNL (Katalenich et al. 2022), INL (Marshall 2019), and ORNL (Collins et al. 2004) for other nuclear applications. These types of systems can be used to produce large quantities of beads at different sizes depending on the chosen orifice diameter.

- While the work presented here sets the bases for future exploratory research using these types of active getters, it is likely (nearly undoubtable) that using higher porosity active gettering materials would yield more effective sorbents overall. Previous work looking at porous sulfides (i.e., aerogels, nanoflowers) (Riley et al. 2013a; Riley et al. 2014; Subrahmanyam et al. 2015; Yu et al. 2020; Yu et al. 2021) demonstrated effective capture of iodine gas even in low-concentration environments. Engineering the active gettering materials to be higher porosity prior to PAN composite synthesis should improve the overall capture efficiency of the composites so this should be explored.

- The exploration of pelletization and CPS for iodine-loaded MS_x-PAN composites should be explored. This was planned but time did not permit these experiments. The thermodynamic calculations show that elemental S should be produced when these are loaded with iodine; it is unclear how the S will behave in the pelletization and firing process.

6.0 References

Baskaran, K, M Ali, BJ Riley, I Zharov, and K Carlson. 2022. "Evaluating the physisorption and chemisorption of iodine on bismuth-functionalized carbon foams." *ACS Mater. Lett.* **4**(9):1780-86.

Baskaran, K, C Elliott, M Ali, J Moon, J Beland, D Cohrs, S Chong, BJ Riley, D Chidambaram, and K Carlson. 2023. "Effects of NO_2 aging on bismuth nanoparticles and bismuth-loaded silica xerogels for iodine capture." *Journal of Hazardous Materials* **446**:130644.

Cao, C, S Chong, L Thirion, JC Mauro, JS McCloy, and A Goel. 2017. "Wet chemical synthesis of apatite-based waste forms–A novel room temperature method for the immobilization of radioactive iodine." *Journal of Materials Chemistry A* **5**(27):14331-42.

Chong, S, J Peterson, J Nam, B Riley, and J McCloy. 2017. "Synthesis and characterization of iodosodalite." *Journal of the American Ceramic Society* **100**(5):2273-84.

Chong, S, JA Peterson, BJ Riley, D Tabada, D Wall, CL Corkhill, and JS McCloy. 2018. "Glass-bonded iodosodalite waste form for immobilization of ^{129}I." *Journal of Nuclear Materials* **504**:109-21.

Chong, S, BJ Riley, RM Asmussen, A Fujii Yamagata, J Marcial, S Lee, and CA Burns. 2022. "Iodine capture with metal-functionalized polyacrylonitrile composite beads containing Ag^0, Bi^0, Cu^0, or Sn^0 particles." *ACS Applied Polymer Materials* **4**(12):9040-51.

Chong, S, BJ Riley, RM Asmussen, AR Lawter, SH Bruffey, J Nam, JS McCloy, and JV Crum. 2020a. "Iodosodalite synthesis with hot isostatic pressing of precursors produced from aqueous and hydrothermal processes." *Journal of Nuclear Materials* **538**:152222.

Chong, S, BJ Riley, W Kuang, and MJ Olszta. 2021. "Iodine capture with mechanically robust heat-treated Ag-Al-Si-O xerogel sorbents." *ACS Omega* **6**(17):11628-38.

Chong, S, BJ Riley, JA Peterson, MJ Olszta, and ZJ Nelson. 2020b. "Gaseous iodine sorbents: A comparison between Ag-loaded aerogel and xerogel scaffolds." *ACS Applied Materials and Interfaces* **12**(23):26127–36.

Collins, JL, RD Hunt, GD Del Cul, and DF Williams. 2004. *Production of Depleted UO2 Kernels for the Advanced Gas-Cooled Reactor Program for use in TRISO Coating Development*. ORNL/TM-2004/123, Oak Ridge National Laboratory, Oak Ridge, TN.

Cordova, EA, V Garayburu-Caruso, CI Pearce, KJ Cantrell, JW Morad, EC Gillispie, BJ Riley, FC Colon, TG Levitskaia, SA Saslow, O Qafoku, CT Resch, MJ Rigali, JE Szecsody, SM Heald, M Balasubramanian, P Meyers, and VL Freedman. 2020. "Hybrid sorbents for ^{129}I capture from contaminated groundwater." *ACS Applied Materials & Interfaces* **12**(23):26113-26.

EPA. 1980. "Identification and listing of hazardous waste." *Code of Federal Regulations* **40**.

Hall, ME, AR Horrocks, and J Zhang. 1994. "Flammability of polyacrylonitrile and its copolymers." *Polymer Degradation and Stability* **44**:379-86.

Horrocks, AR, J Zhang, and ME Hall. 1994. "Flammability of polyacrylonitrile and its copolymers II. Thermal behaviour and mechanism of degradation." *Polymer International* **33**:303-14.

Hrma, P and AA Kruger. 2016. "High-temperature viscosity of many-component glass melts." *Journal of Non-Crystalline Solids* **437**:17-25.

Kabatesi, JC and J-P Wang. 2022. "Separating silver from tin silver alloy residue: Effect of agitation rate." *Metals* **12**:177.

Katalenich, JA, SM Lee, RL Oelrich, C Padilla Cintron, BN Robertson, H Shah, and DJ Sunderland. 2022. *Framatome TRISO Study*. PNNL-33776, Pacific Northwest National Laboratory, Richland, WA.

Khairulin, RA, SV Stankus, RN Abdullaev, and VM Sklyarchuk. 2010. "The density and interdiffusion coefficients of bismuth-tin melts of eutectic and near-eutectic composition." *High Temperature* **48**(2):188-91.

Kim, B-S, J-C Lee, and S-K Kim. 2010. "A novel cyclic process involving zinc for separating silver from lead-free solder residue." *Materials Transactions* **51**:1350-53.

Lide, DR. 2008. *CRC Handbook of Chemistry and Physics*, 88th ed., CRC Press, Boca Raton, FL.

Liu, PS and GF Chen. 2014. "Making Porous Metals." In *Porous Materials: Processing and Applications*, eds. PS Liu and GF Chen, ch. 2, pp. 43. Butterworth-Heinemann (Elsevier), Amsterdam.

Marshall, DW. 2019. *AGR-5/6/7 Fuel Fabrication Report*. INL/EXT-19-53720, Idaho National Laboratory, Idaho Falls, ID.

MTI. Calculating applied pressure on pellet pressing die. 2023. Accessed at https://www.mtixtl.com/YLJ-HP2-H.aspx.

NIST. Phase Diagrams & Computational Thermodynamics: Bi-Sn System. 2023. Accessed at https://www.metallurgy.nist.gov/phase/solder/bisn.html.

Riley, BJ, S Chong, RM Asmussen, A Bourchy, and MH Engelhard. 2021a. "Polyacrylonitrile Composites of Ag-Al-Si-O Aerogels and Xerogels as Iodine and Iodide Sorbents." *ACS Applied Polymer Materials* **3**(7):3344-53.

Riley, BJ, S Chong, and CL Beck. 2021b. "Iodine vapor reactions with pure metal wires at temperatures of 100-139 °C in air." *Industrial & Engineering Chemistry Research* **60**(47):17162-73.

Riley, BJ, S Chong, and NL Canfield. 2024. "Synthesis of and iodine capture with MS_x (Ag_2S, Bi_2S_3, Cu_2S)–polyacrylonitrile composites." *New Journal of Chemistry* **48**(8):3352-56.

Riley, BJ, S Chong, W Kuang, T Varga, AS Helal, M Galanek, J Li, ZJ Nelson, and PK Thallapally. 2020a. "Metal–organic framework–polyacrylonitrile composite beads for xenon capture." *ACS Applied Materials & Interfaces* **12**(40):45342-50.

Riley, BJ, S Chong, J Marcial, N Lahiri, MK Bera, S Lee, T Wu, K Kruska, and J Matyáš. 2022a. "Silver-loaded xerogel nanostructures for iodine capture: A comparison of thiolated versus unthiolated sorbents." *ACS Applied Nano Materials* **5**(7):9478-94.

Riley, BJ, S Chong, MJ Olszta, and JA Peterson. 2020b. "Evaluation of getter metals in Na-Al-Si-O aerogels and xerogels for the capture of iodine gas." *ACS Applied Materials & Interfaces* **12**(17):19682-92.

Riley, BJ, S Chong, J Schmid, J Marcial, ET Nienhuis, MK Bera, S Lee, NL Canfield, S Kim, MA Derewinski, and RK Motkuri. 2022b. "Role of zeolite structural properties toward iodine capture: A head-to-head evaluation of framework type and chemical composition." *ACS Applied Materials & Interfaces* **14**(16):18439-52.

Riley, BJ, J Chun, JV Ryan, J Matyáš, XS Li, DW Matson, SK Sundaram, DM Strachan, and JD Vienna. 2011. "Chalcogen-based aerogels as a multifunctional platform for remediation of radioactive iodine." *RSC Advances* **1**:1704-15.

Riley, BJ, J Chun, W Um, WC Lepry, J Matyas, MJ Olszta, X Li, K Polychronopoulou, and MG Kanatzidis. 2013a. "Chalcogen-Based Aerogels As Sorbents for Radionuclide Remediation." *Environmental Science & Technology* **47**(13):7540-47.

Riley, BJ and T Garn. 2019. "Purification of Gas and Liquid Streams Using Composite Sorbents Embedded in a Polyacrylonitrile Matrix." In *Advances in Materials Science Research*, ed. M Wythers, Vol 35, pp. 119-47. Nova Science Publishers.

Riley, BJ, JO Kroll, JA Peterson, J Matyáš, MJ Olszta, X Li, and JD Vienna. 2017. "Silver-loaded aluminosilicate aerogels as iodine sorbents." *ACS Applied Materials & Interfaces* **9**(38):32907-19.

Riley, BJ, D Pierce, A, and J Chun. 2013b. *Efforts to Consolidate Chalcogels with Adsorbed Iodine*. FCRD-SWF-2013-000249, PNNL-22678, Pacific Northwest National Laboratory, Richland, WA.

Riley, BJ, D Pierce, A, J Chun, J Matyáš, WC Lepry, T Garn, J Law, and MG Kanatzidis. 2014. "Polyacrylonitrile-chalcogel hybrid sorbents for radioiodine capture." *Environmental Science & Technology* **48**(10):5832-39.

Sanderson, RT. 2023. "*Bismuth.*" Encyclopædia Britannica, Inc.

Sobolev, V. 2007. "Thermophysical properties of lead and lead-bismuth eutectic." *Journal of Nuclear Materials* **362**(2):235-47.

Sobolev, VP and A Gessi. 2015. "Thermophysical and electric properties of liquid lead, bismuth and lead-bismuth eutectic." In *Handbook on Lead-bismuth Eutectic Alloy and Lead Properties, Materials Compatibility, Thermal-hydraulics and Technologies*, ch. 2, Nuclear Energy Agency Organisation for Economic Cooperation and Development (NEA-OECD).

Subrahmanyam, KS, D Sarma, CD Malliakas, K Polychronopoulou, BJ Riley, DA Pierce, J Chun, and MG Kanatzidis. 2015. "Chalcogenide aerogels as sorbents for radioactive iodine." *Chemistry of Materials* **27**(7):2619-26.

Vatanpour, V, ME Pasaoglu, B Kose-Mutlu, and I Koyuncu. 2023. "Polyacrylonitrile in the Preparation of Separation Membranes: A Review." *Industrial & Engineering Chemistry Research* **62**(17):6537-58.

Yadav, A, S Chong, BJ Riley, JS McCloy, and A Goel. 2023. "Iodine capture by Ag-loaded solid sorbents followed by Ag recycling and iodine immobilization: An end-to-end process." *Industrial & Engineering Chemistry Research* **62**(8):3635-46.

Yu, Q, X Jiang, Z Cheng, Y Liao, Q Pu, and M Duan. 2020. "Millimeter-sized Bi_2S_3@polyacrylonitrile hybrid beads for highly efficient iodine capture." *New Journal of Chemistry* **44**(39):16759-68.

Yu, Q, X Jiang, and M Duan. 2021. "Nano-flower-shaped SnS_2 doped polyacrylonitrile hybrid beads for effective capture of radioactive gaseous iodine." *Social Science Research Network*.

Appendix A – Additional Data and Information

A.1 Calculations for Understanding Iodine Loading

$$Q_{\mathrm{e}} = {}^{m_{\mathrm{I}}}/_{m_{\mathrm{polymet}}} \tag{A.1}$$

$$m_{\mathrm{polymet+I}} = m_{\mathrm{polymet}} + m_{\mathrm{I}} = (1 + Q_e)m_{\mathrm{polymet}} \tag{A.2}$$

A.2 XRD Data

A.2.1 XRD of Pure Metal Encapsulants

Table A1. Summary of XRD data for as-received encapsulant metals where PDF is the powder diffraction file, SG is the space group, and *a*, *b*, and *c* are the unit cell parameters. Note that $BiSn^0$ is just a mixture of the two base metals (Bi^0 and Sn^0).

Material	PDF	SG (#)	*a* (Å)	*b* (Å)	*c* (Å)
Bi^0	05-0519	*R*-3*m* (166)	4.546	4.546	11.86
Sn^0	04-0673	$I4_1/amd$ (141)	5.831	5.831	3.182
$BiSn^0$	05-0519	*R*-3*m* (166)	4.546	4.546	11.86
	04-0673	$I4_1/amd$ (141)	5.831	5.831	3.182

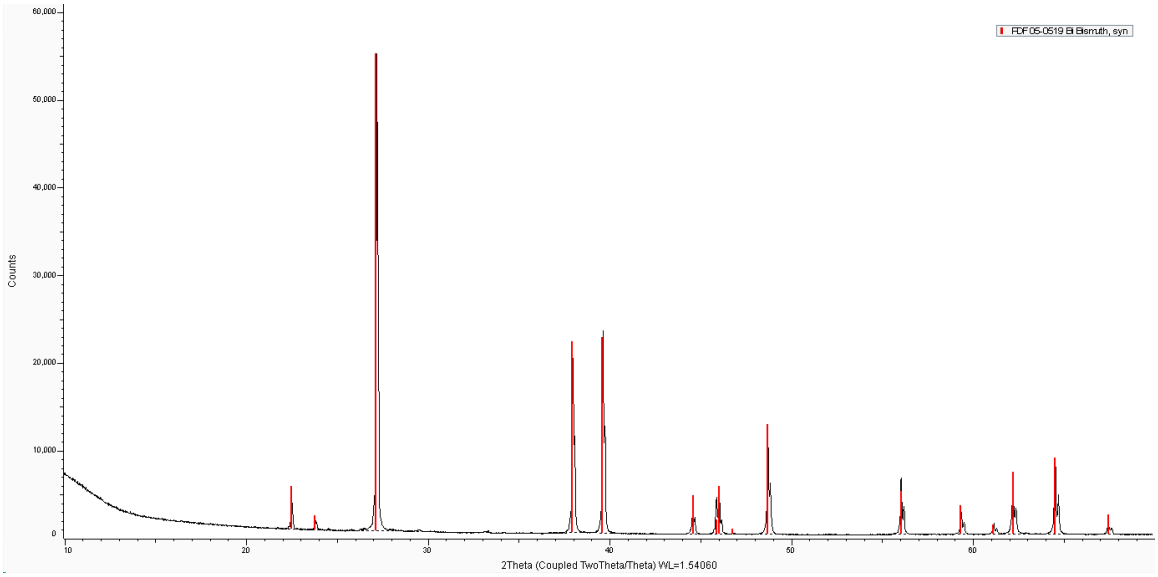

Figure A-1. XRD of as-received Bi^0 particles from American Elements.

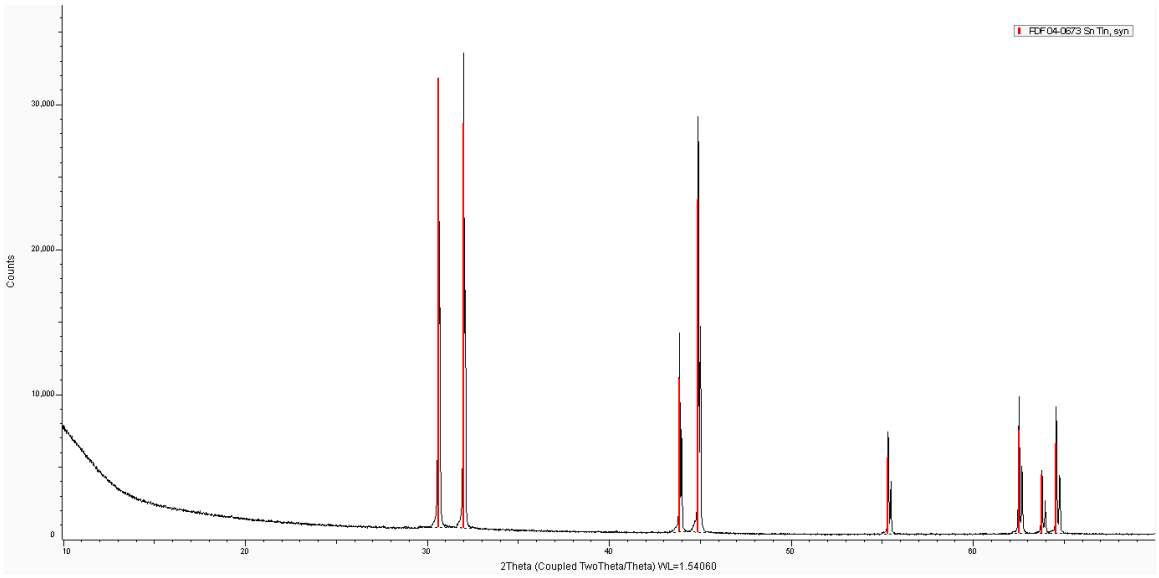

Figure A-2. XRD of as-received Sn^0 particles from American Elements.

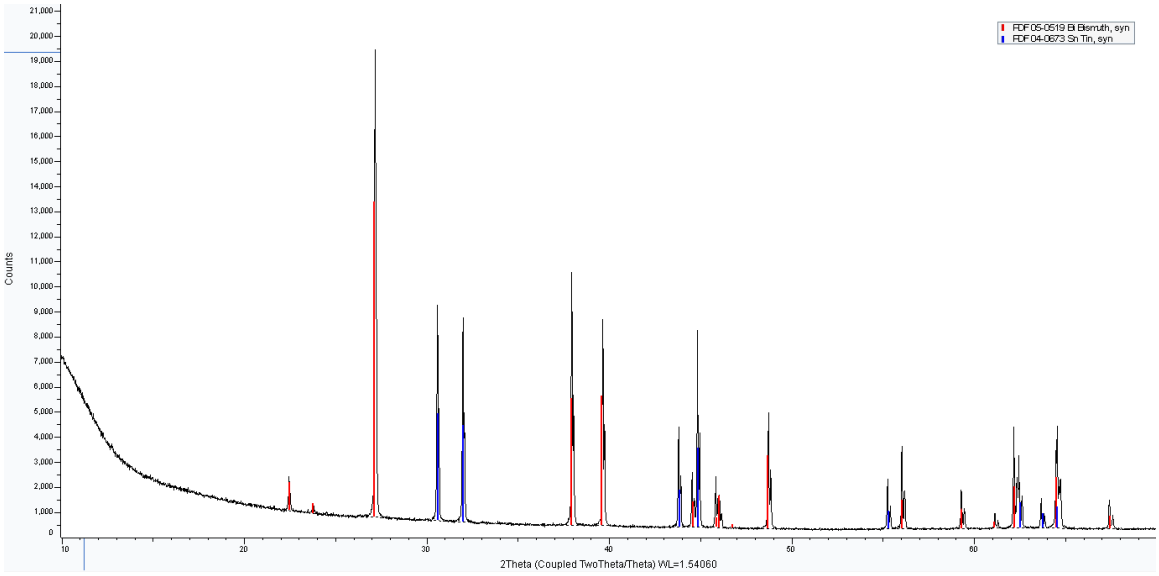

Figure A-3. XRD of as-received $BiSn^0$ alloy particles from American Elements.

A.2.2 XRD of PAN Composites Without Iodine

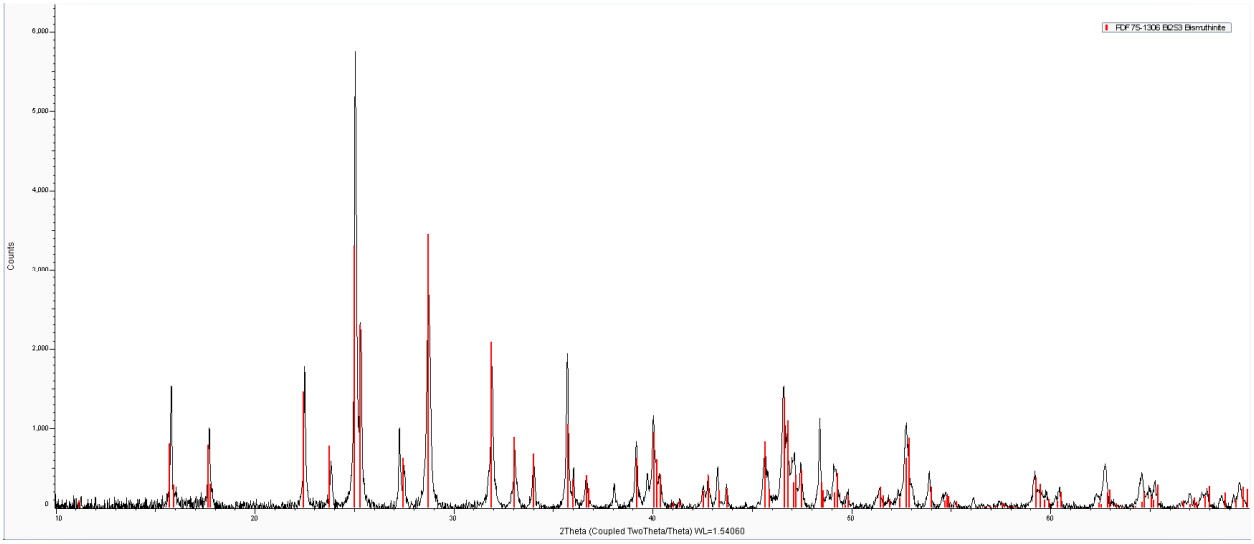

Figure A-4. XRD of unloaded 80BiS-PAN (Bi_2S_3) composites.

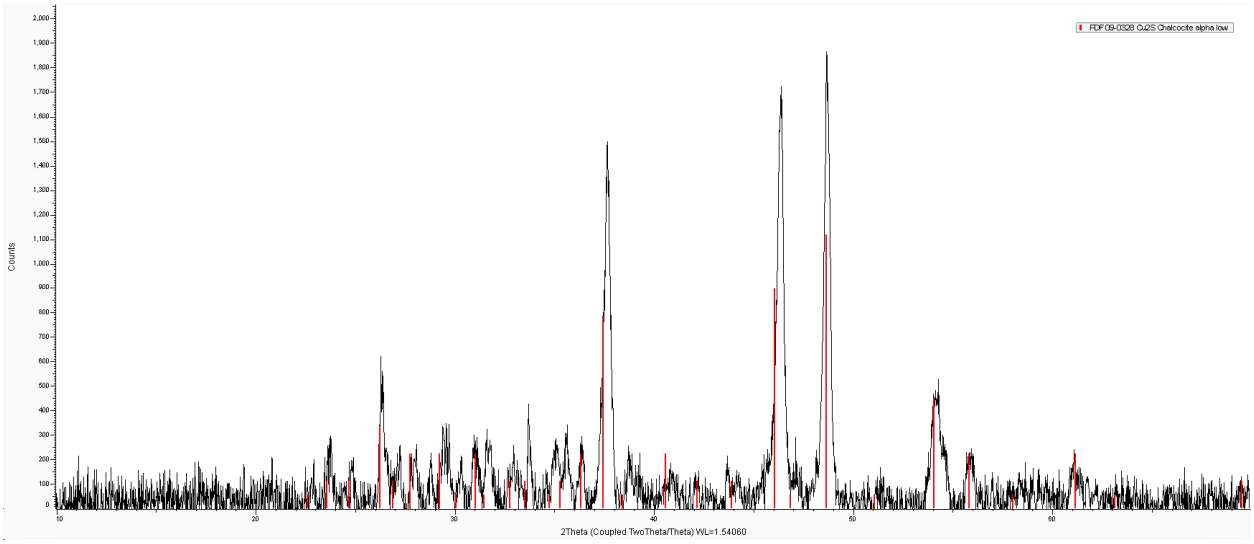

Figure A-5 XRD of unloaded 80CuS-PAN (Cu_2S) composites.

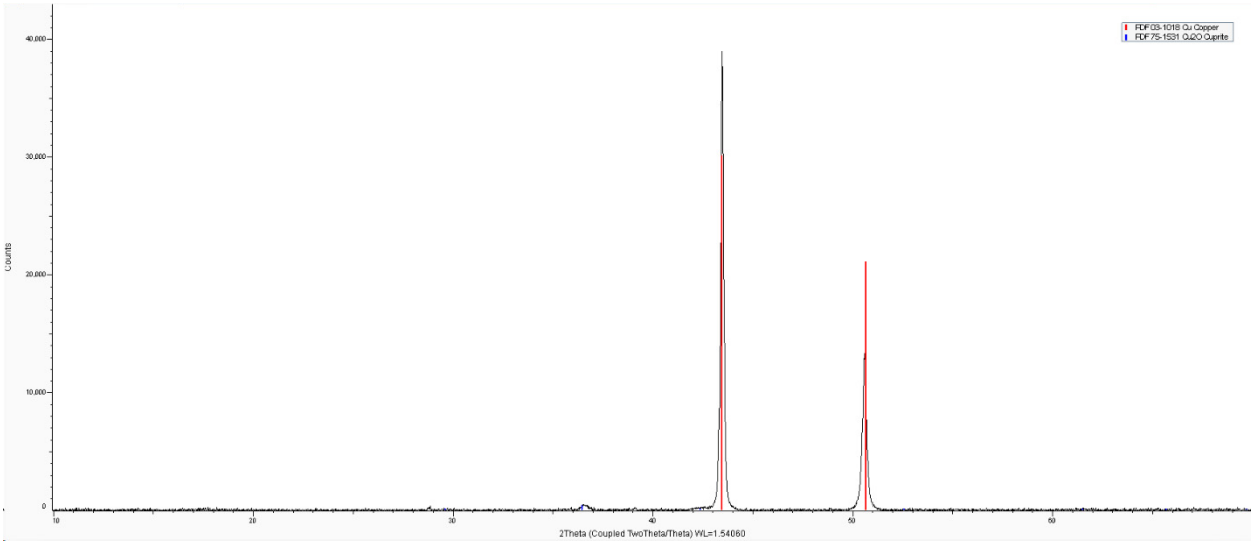

Figure A-6. XRD for 80Cu-PAN (before iodine).

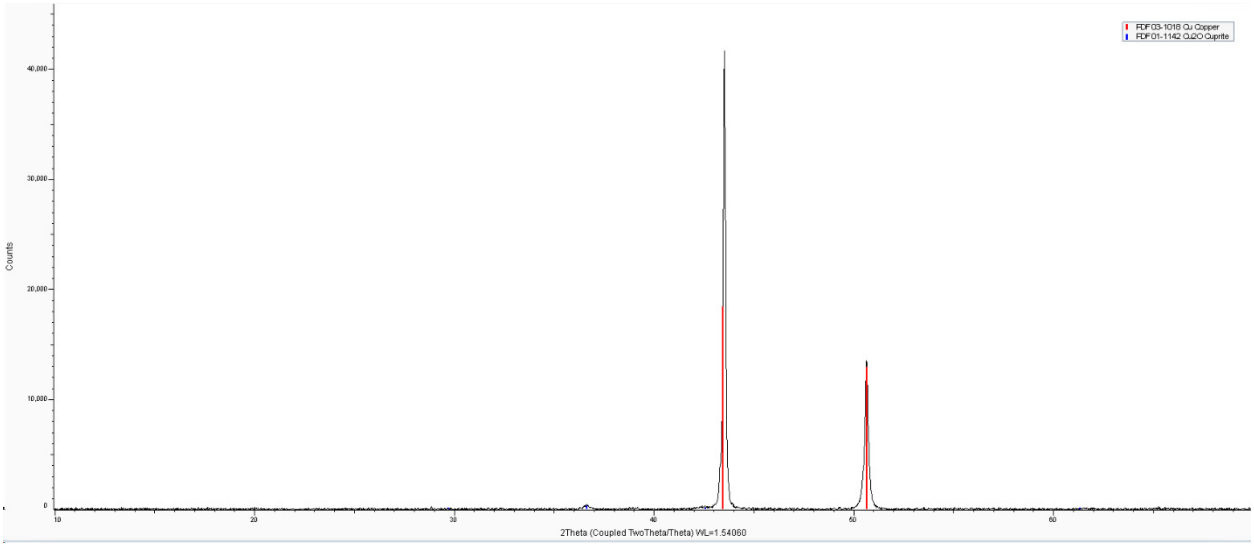

Figure A-7. XRD for 90Cu-PAN (before iodine).

A.2.3 XRD of Iodine-Loaded PAN Composites

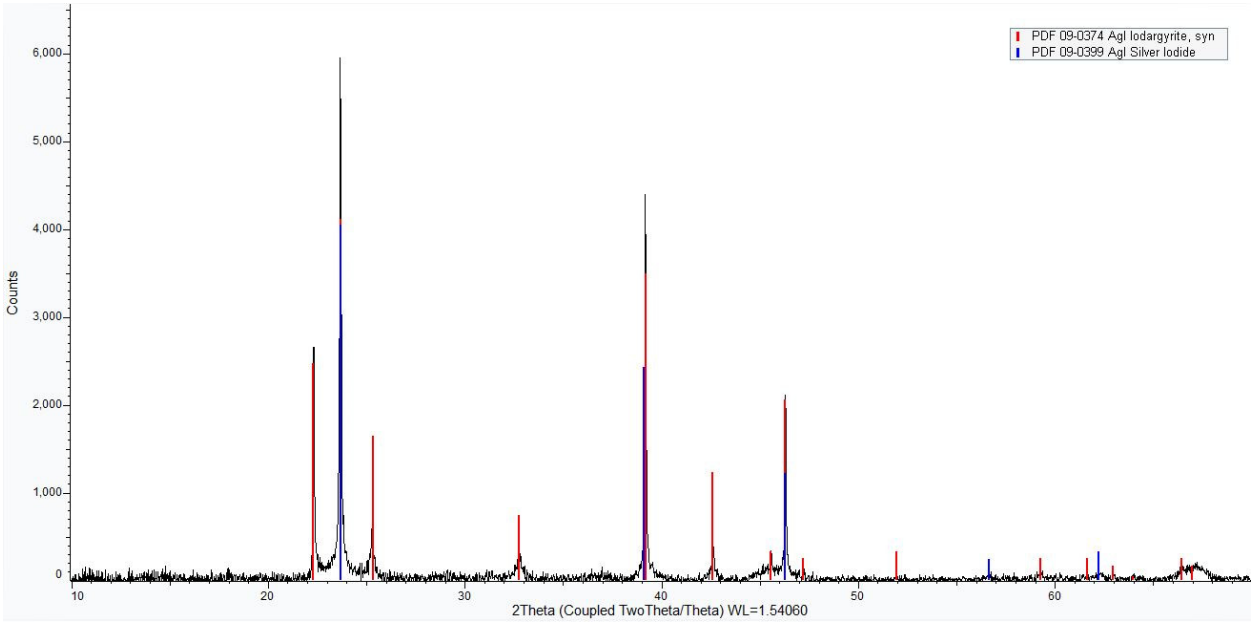

Figure A-8. XRD of Clariant AC-6120[130] material after iodine.

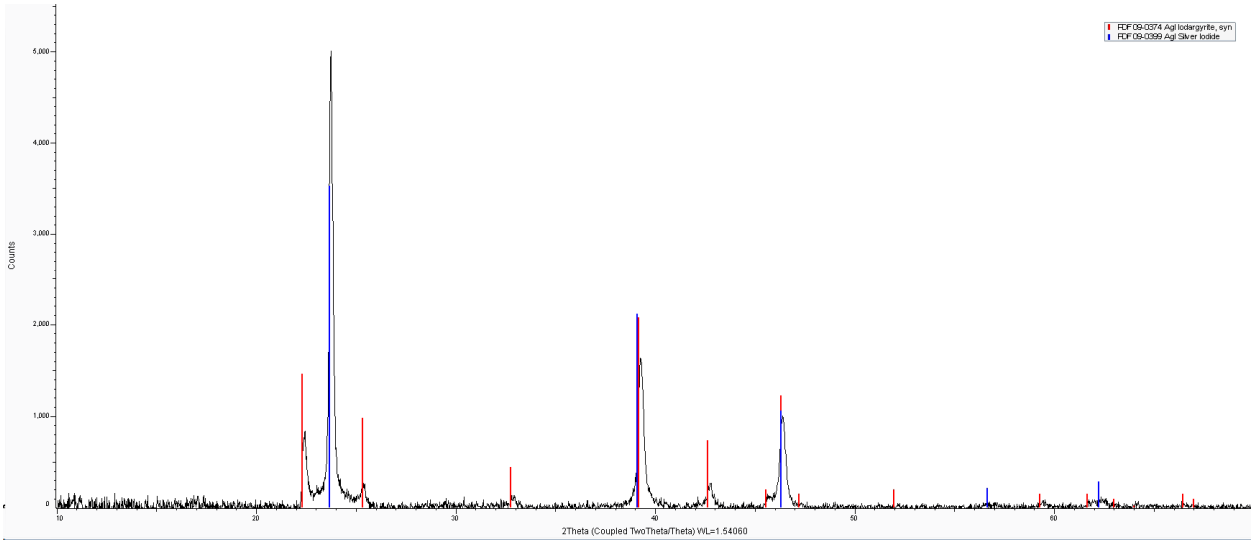

Figure A-9. XRD of AgI-PAN[130].

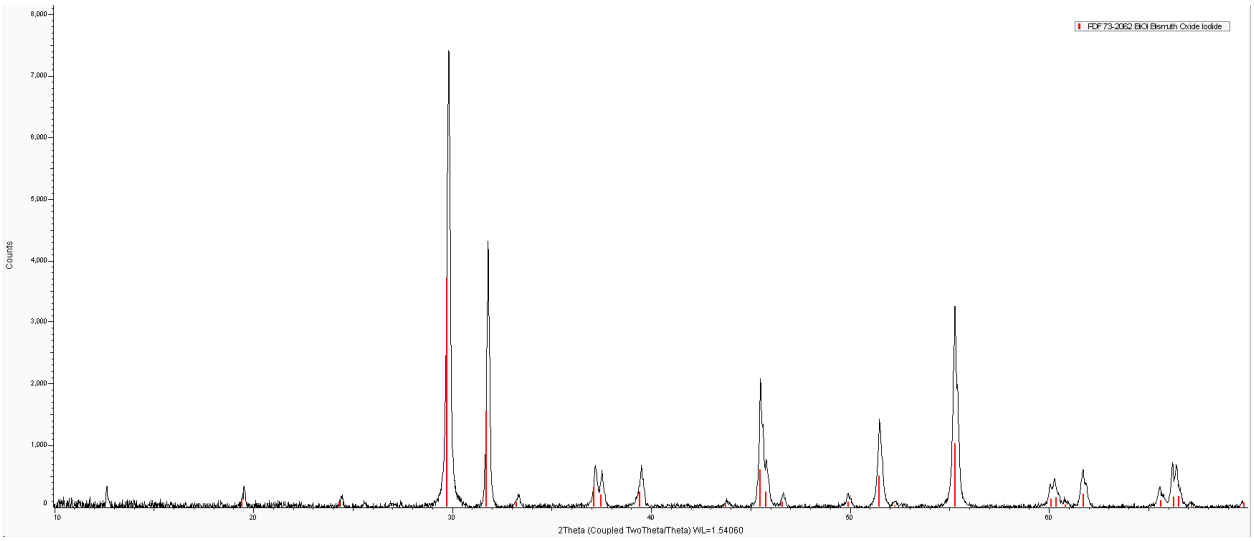

Figure A-10. XRD of BiI-PAN(130) on only the orange-colored beads.

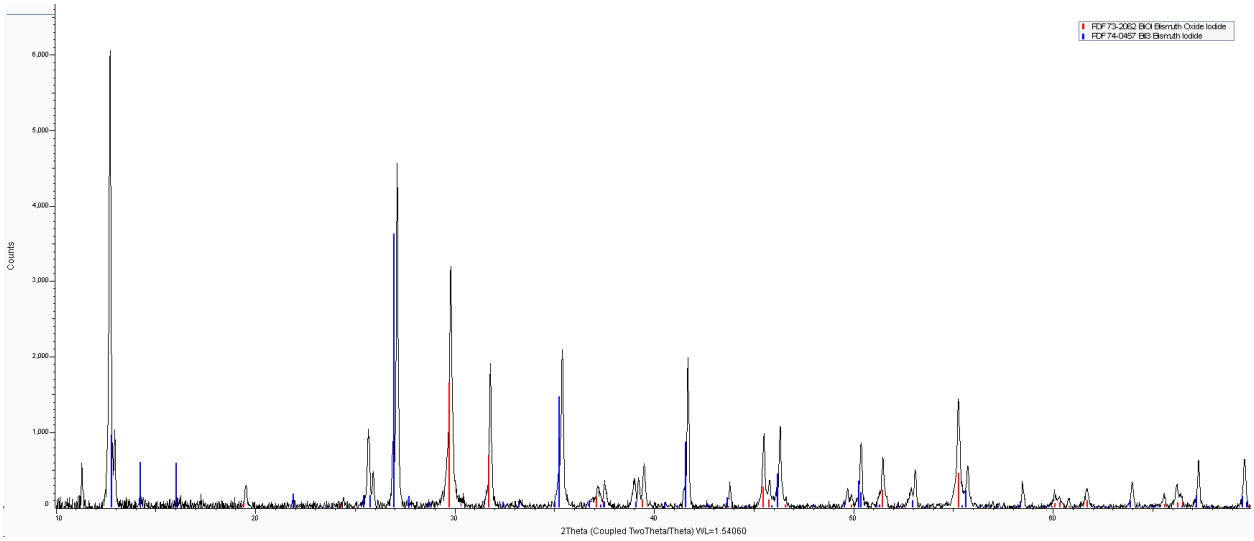

Figure A-11. XRD of BiI-PAN(130) on only the brown-colored beads.

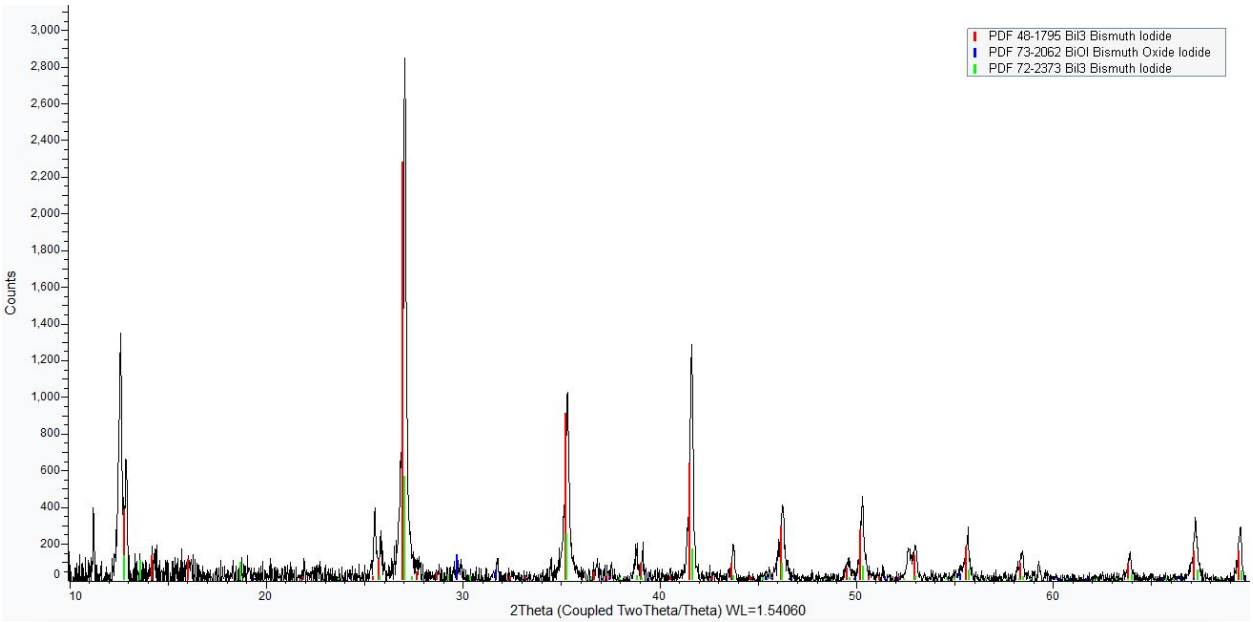

Figure A-12. XRD of 80BiS-PAN(130) after iodine loading. The two BiI_3 phases differ by the space group (hexagonal and rhombohedral).

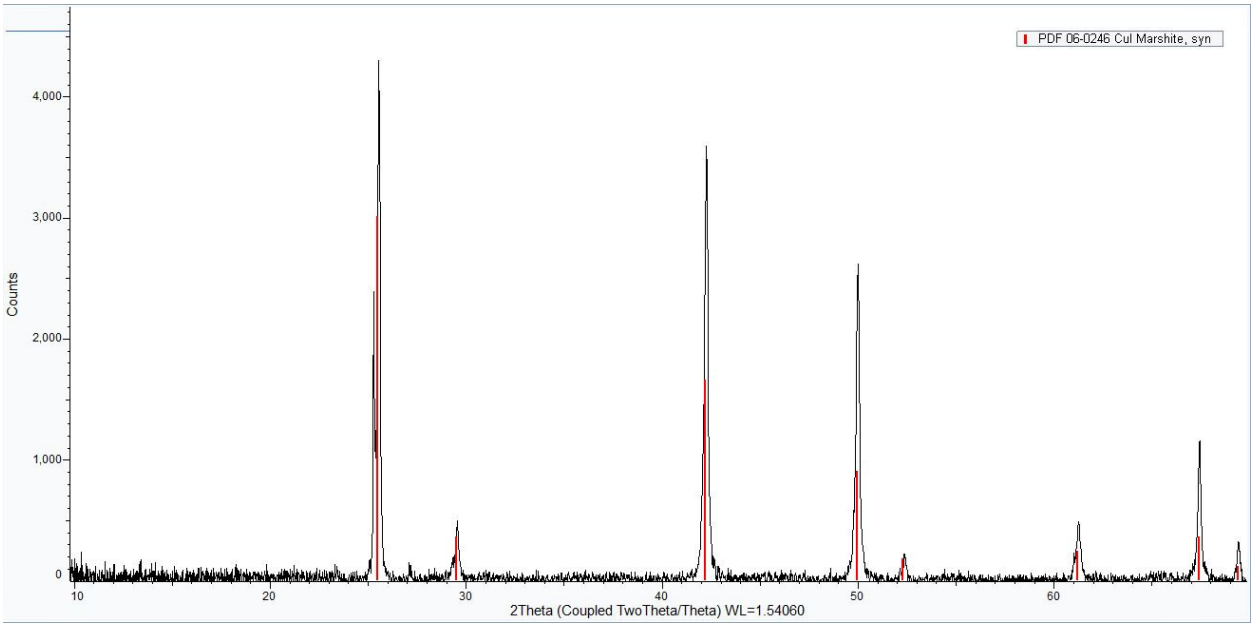

Figure A-13. XRD of 80CuS-PAN(130) after iodine loading.

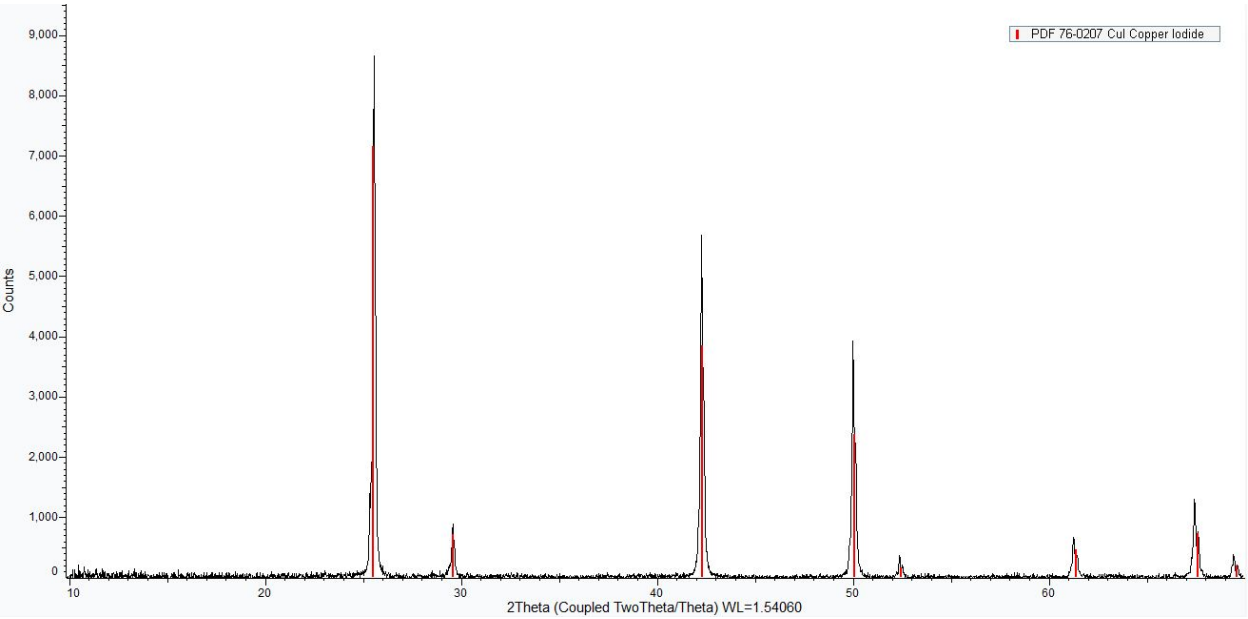

Figure A-14. XRD of 80Cu-PAN(130) after iodine loading.

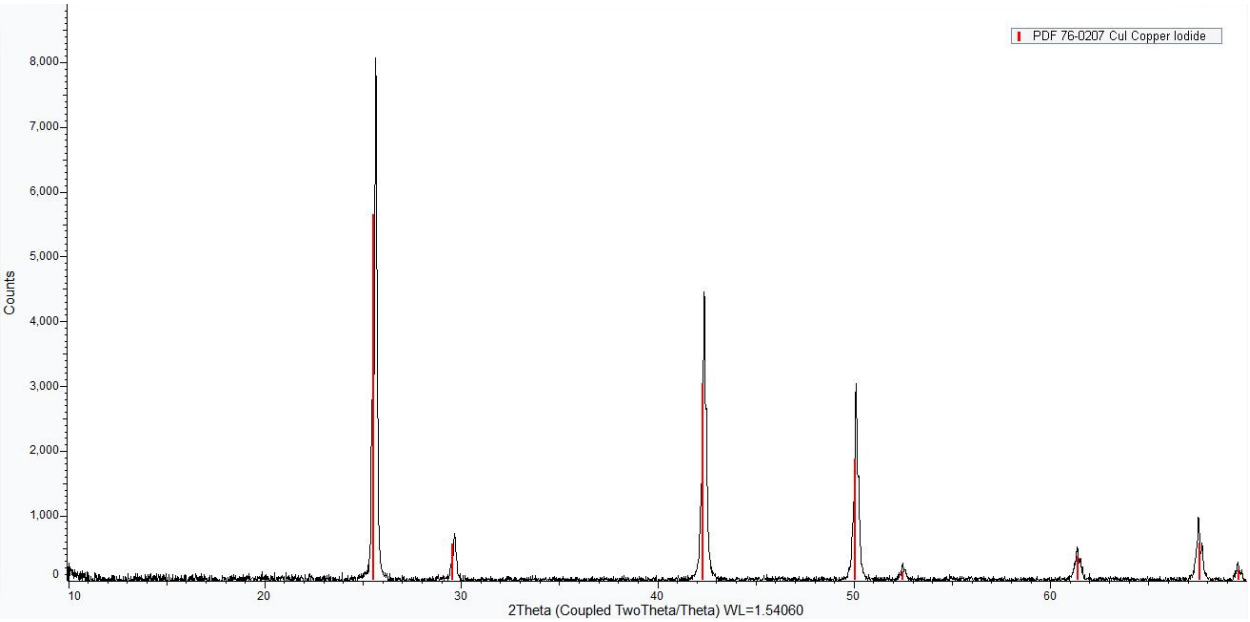

Figure A-15. XRD of 90Cu-PAN(130) after iodine loading.

A.3 PSDs of Metal Encapsulants

Size(um)	%Chan	%Pass	Size(um)	%Chan	%Pass
2000	0.00	100.00	3.89	0.00	0.00
1674	0.00	100.00	3.27	0.00	0.00
1408	0.00	100.00	2.750	0.00	0.00
1184	0.00	100.00	2.313	0.00	0.00
995.6	0.00	100.00	1.945	0.00	0.00
837.2	0.00	100.00	1.635	0.00	0.00
704.0	0.00	100.00	1.375	0.00	0.00
592.0	0.00	100.00	1.156	0.00	0.00
497.8	0.00	100.00	0.972	0.00	0.00
418.6	0.00	100.00	0.818	0.00	0.00
352.0	0.00	100.00	0.688	0.00	0.00
296.0	0.25	100.00	0.578	0.00	0.00
248.9	0.56	99.75	0.486	0.00	0.00
209.3	1.01	99.19	0.409	0.00	0.00
176.0	1.75	98.18	0.344	0.00	0.00
148.0	2.76	96.43	0.2890	0.00	0.00
124.5	4.04	93.67	0.2430	0.00	0.00
104.7	5.91	89.63	0.2040	0.00	0.00
88.00	8.72	83.72	0.1720	0.00	0.00
74.00	11.74	75.00	0.1450	0.00	0.00
62.23	12.82	63.26	0.1220	0.00	0.00
52.33	11.05	50.44	0.1020	0.00	0.00
44.00	8.39	39.39	0.0860	0.00	0.00
37.00	6.56	31.00	0.0720	0.00	0.00
31.11	5.72	24.44	0.0610	0.00	0.00
26.16	5.18	18.72	0.0510	0.00	0.00
22.00	4.44	13.54	0.0430	0.00	0.00
18.50	3.37	9.10	0.0360	0.00	0.00
15.56	2.27	5.73	0.0300	0.00	0.00
13.08	1.43	3.46	0.02550	0.00	0.00
11.00	0.91	2.03			
9.25	0.61	1.12			
7.78	0.36	0.51			
6.54	0.15	0.15			
5.50	0.00	0.00			
4.63	0.00	0.00			

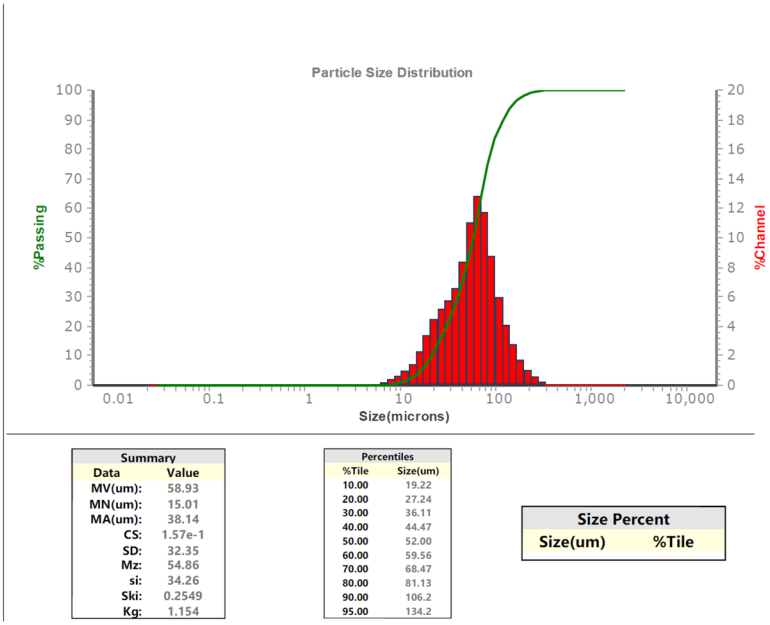

Summary	
Data	Value
MV(um):	58.93
MN(um):	15.01
MA(um):	38.14
CS:	1.57e-1
SD:	32.35
Mz:	54.86
si:	34.26
Ski:	0.2549
Kg:	1.154

Percentiles	
%Tile	Size(um)
10.00	19.22
20.00	27.24
30.00	36.11
40.00	44.47
50.00	52.00
60.00	59.56
70.00	68.47
80.00	81.13
90.00	106.2
95.00	134.2

Size Percent	
Size(um)	%Tile

Figure A-16. PSD data for bismuth metal encapsulant used in this study.

Size(um)	%Chan	%Pass	Size(um)	%Chan	%Pass
2000	0.00	100.00	3.89	1.70	6.96
1674	0.00	100.00	3.27	1.38	5.26
1408	0.00	100.00	2.750	1.10	3.88
1184	0.00	100.00	2.313	0.88	2.78
995.6	0.00	100.00	1.945	0.62	1.90
837.2	0.00	100.00	1.635	0.50	1.28
704.0	0.00	100.00	1.375	0.39	0.78
592.0	0.00	100.00	1.156	0.28	0.39
497.8	0.00	100.00	0.972	0.11	0.11
418.6	0.00	100.00	0.818	0.00	0.00
352.0	0.00	100.00	0.688	0.00	0.00
296.0	0.00	100.00	0.578	0.00	0.00
248.9	0.17	100.00	0.486	0.00	0.00
209.3	0.64	99.83	0.409	0.00	0.00
176.0	1.21	99.19	0.344	0.00	0.00
148.0	2.22	97.98	0.2890	0.00	0.00
124.5	3.75	95.76	0.2430	0.00	0.00
104.7	5.89	92.01	0.2040	0.00	0.00
88.00	8.47	86.12	0.1720	0.00	0.00
74.00	10.22	77.65	0.1450	0.00	0.00
62.23	9.40	67.43	0.1220	0.00	0.00
52.33	6.58	58.03	0.1020	0.00	0.00
44.00	3.99	51.45	0.0860	0.00	0.00
37.00	2.57	47.46	0.0720	0.00	0.00
31.11	2.05	44.89	0.0610	0.00	0.00
26.16	2.09	42.84	0.0510	0.00	0.00
22.00	2.54	40.75	0.0430	0.00	0.00
18.50	3.28	38.21	0.0360	0.00	0.00
15.56	4.05	34.93	0.0300	0.00	0.00
13.08	4.46	30.88	0.02550	0.00	0.00
11.00	4.48	26.42			
9.25	4.04	21.94			
7.78	3.47	17.90			
6.54	2.93	14.43			
5.50	2.47	11.50			
4.63	2.07	9.03			

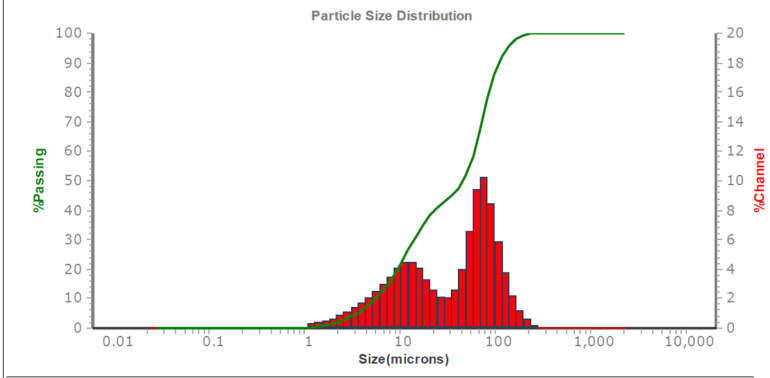

Summary	
Data	Value
MV(um):	46.11
MN(um):	1.924
MA(um):	12.47
CS:	4.81e-1
SD:	38.38
Mz:	44.22
si:	36.78
Ski:	0.2172
Kg:	0.790

Percentiles	
%Tile	Size(um)
10.00	4.97
20.00	8.53
30.00	12.64
40.00	20.82
50.00	41.71
60.00	54.46
70.00	64.97
80.00	77.30
90.00	97.88
95.00	119.3

Size Percent	
Size(um)	%Tile

Figure A-17. PSD data for tin metal encapsulant used in this study.

Size(um)	%Chan	%Pass	Size(um)	%Chan	%Pass
2000	0.00	100.00	3.89	0.00	0.00
1674	0.00	100.00	3.27	0.00	0.00
1408	0.00	100.00	2.750	0.00	0.00
1184	0.00	100.00	2.313	0.00	0.00
995.6	0.00	100.00	1.945	0.00	0.00
837.2	0.00	100.00	1.635	0.00	0.00
704.0	0.00	100.00	1.375	0.00	0.00
592.0	0.00	100.00	1.156	0.00	0.00
497.8	0.00	100.00	0.972	0.00	0.00
418.6	0.00	100.00	0.818	0.00	0.00
352.0	0.00	100.00	0.688	0.00	0.00
296.0	0.17	100.00	0.578	0.00	0.00
248.9	0.60	99.83	0.486	0.00	0.00
209.3	1.18	99.23	0.409	0.00	0.00
176.0	2.20	98.05	0.344	0.00	0.00
148.0	3.69	95.85	0.2890	0.00	0.00
124.5	5.62	92.16	0.2430	0.00	0.00
104.7	8.33	86.54	0.2040	0.00	0.00
88.00	12.37	78.21	0.1720	0.00	0.00
74.00	16.68	65.84	0.1450	0.00	0.00
62.23	17.69	49.16	0.1220	0.00	0.00
52.33	13.76	31.47	0.1020	0.00	0.00
44.00	8.31	17.71	0.0860	0.00	0.00
37.00	4.51	9.40	0.0720	0.00	0.00
31.11	2.46	4.89	0.0610	0.00	0.00
26.16	1.37	2.43	0.0510	0.00	0.00
22.00	0.75	1.06	0.0430	0.00	0.00
18.50	0.31	0.31	0.0360	0.00	0.00
15.56	0.00	0.00	0.0300	0.00	0.00
13.08	0.00	0.00	0.02550	0.00	0.00
11.00	0.00	0.00			
9.25	0.00	0.00			
7.78	0.00	0.00			
6.54	0.00	0.00			
5.50	0.00	0.00			
4.63	0.00	0.00			

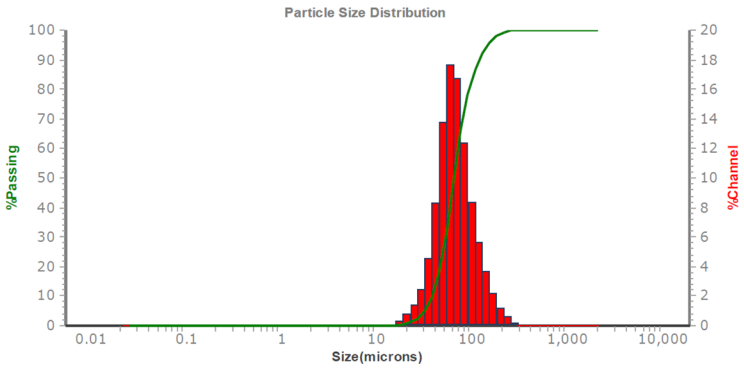

Summary	
Data	Value
MV(um):	71.10
MN(um):	39.50
MA(um):	58.21
CS:	1.03e-1
SD:	27.91
Mz:	68.02
si:	30.60
Ski:	0.355
Kg:	1.285

Percentiles	
%Tile	Size(um)
10.00	37.60
20.00	45.52
30.00	51.50
40.00	57.00
50.00	62.75
60.00	69.41
70.00	77.96
80.00	90.89
90.00	115.5
95.00	141.1

Size Percent	
Size(um)	%Tile

Figure A-18. PSD data for bismuth-tin eutectic metal encapsulant used in this study.

Pacific Northwest National Laboratory

902 Battelle Boulevard
P.O. Box 999
Richland, WA 99354

1-888-375-PNNL (7665)

www.pnnl.gov